The Pennsylvania State University

The Graduate School

Eberly College of Science

INVESTIGATION AND CHARACTERIZATION OF THE NATURE OF THE ELECTRICAL CONTACTS IN MOLECULAR ELECTRONIC DEVICE CONSTRUCTIONS

A Thesis in

Chemistry

by

Thomas Addison Daniel

© 2005 Thomas Addison Daniel

Submitted in Partial Fulfillment
of the Requirements
for the Degree of

Doctor of Philosophy

August 2005

The thesis of Thomas Addison Daniel was reviewed and approved* by the following:

David L. Allara
Professor of Chemistry and Materials Science
Thesis Advisor
Chair of Committee

Nicholas Winograd
Evan Pugh Professor of Chemistry

Thomas E. Mallouk
DuPont Professor of Materials Chemistry and Physics

Mark Horn
Distinguished Professor of Engineering Science and Mechanics

Ayusman Sen
Professor of Chemistry
Head of the Department of Chemistry

*Signatures are on file in the Graduate School

Abstract

An overview of various molecular electronic device constructions that utilize self-assembly is given in chapter 1 with a more specific analysis of selected devices studied in later chapters. The second chapter details the use of CPAFM to probe the nature of the evolving interface and metal morphology arising from Au vapor deposition onto the surface of a SAM. The results show that the Au penetrates the ordered regions of the monolayer and forms a uniform layer at the thiol interface. However, filaments form at defect sites in the monolayer due to a higher diffusion rate through the monolayer. These results suggest that vapor deposition of Au is problematic for use in MEDs since no top contact is formed. The third chapter details the used of various applied techniques to probe the nature of the evolving interface chemistry and metal morphology arising from Ti vapor deposition onto the surface of a SAM. The results reveal a highly heterogeneous Ti overlayer forms, in which a large fraction of atoms do not stick to the bare SAM surface while the adsorbed atoms lead to a highly heterogeneous film. The data indicate that for applications such as molecular device contacts the use of Ti may be highly problematic. The fourth chapter inspects the growth of multilayer molecular films used as molecular resists. The actual performance of such a resist is dependent on the exact way that the multilayer stacks organize during the assembly, yet little is definitively known about the details. We have applied surface science techniques to unravel the mechanisms of multi-assembly. Our results differ significantly from previously proposed growth mechanisms, and point to improved ways to form multilayer films. The fifth chapter inspects SAMs of the isocyano derivative of OPE have been prepared in oxygen-free environments on smooth Pd surfaces. The SAMs show significant chemical

instability when exposed to ambient conditions. Exposure results in a chemically degraded interface structure. CPAFM measurements show the conductance of the Pd SAMs diminish by ~2 orders of magnitude. The results underscore the importance of controlled assembly procedures for aromatic isocyanide SAMs.

TABLE OF CONTENTS

List of Figures ix

List of Tables xvii

Acknowledgments xviii

CHAPTER 1 Introduction 1

1.1 Introduction to Molecular Electronics 2

1.2 Molecular Electrical Contacts Formed via Metal Vapor Deposition 4

1.3 Molecular Electrical Contacts Formed on nanofabricated metal gaps 5

1.4 Molecular Devices that Utilize Alternate Chemical Binding to the Substrate 7

References 9

CHAPTER 2 Evolution of the Interface and Metal Film Morphology in the Vapor Deposition of Au on Dodecanethiolate monolayers on Au {111} 17

2.1 Introduction 18

2.2 Experimental 19

2.2.1 Sample Preparation 19

2.2.2 Metal Depositions 20

2.2.3 Atomic force Microscopy 21

2.3 Results and Discussion 22

2.4 Conclusions 30

References 32

Chapter 3 Evolution of the Interface and Metal Film Morphology in the Vapor Deposition of Ti on Hexadecanethiolate Monolayers On Au{111} 35

3.1 Introduction 36

3.2 Experimental 39

3.2.1 Materials and General Procedures 39

3.2.2 X-Ray Photoelectron Spectroscopy 40

3.2.3 Infrared Spectroscopy 40

3.2.4 Time-of-Flight Secondary Ion Mass Spectrometry 41

3.2.5 Atomic Force Microscopy 41

3.2.6 Definition and Measurement of Deposited Metal Coverage 42

3.3 Results 44

3.3.1 XPS – Formation of Carbide Products 44

3.3.2 IRS – Ti Deposition on a $CD_3(CD_2)_7(CH_2)_8$S-/Au SAM – a "Top Down" Localized Chemical Degradation 46

3.3.3 AFM – Ti Clustering and Heterogeneous Overlayer Morphology 50

3.3.4 ToF-SIMS – Localized Chemical Degradation 57

3.4 Discussion 59

3.5 Conclusions 63

3.6 Acknowledgements 65

References 66

CHAPTER 4 Investigation of the Growth Mechanisms and interface properties of α,ω-Mercaptoalkanoic Acid Multilayer Films 71

4.1 Introduction 72

4.2 Experimental 76

4.2.1 Materials 76

4.2.2 Sample Preparation 76

4.2.3 Characterization Methods 77

4.2.3.1 Single Wavelength Ellipsometry (SWE) 77

4.2.3.2 Infrared Reflection Spectroscopy (IRS) 78

4.2.3.3 X-Ray Photoelectron Spectroscopy (XPS) 80

4.2.3.4 Contact Angle 80

4.3 Results and Discussion 81

4.3.1 Formation of a MHA|MH Bilayer 81

4.3.1.1.1 Formation of the MHA SAM 81

4.3.1.1.2 Formation of the MPA SAM 84

4.3.1.2 Formation of the MHA-Cu^{2+} coordinated surface 88

4.3.1.3 Formation of a MHA|MH bilayer film 94

4.3.1.4 Readdition of copper and MH to densify the bilayer film 100

4.3.1.4.1 Addition of Cu^{2+} to the MHA|MH bilayer film 100

4.3.1.4.2 Readdition of MH to a MHA|MH bilayer film 103

4.3.2 MHA| MHA| MH Trilayer films 105

4.3.2.1 Formation of a MHA|MHA bilayer 105

4.3.2.2 Copper Coordination of adlayers of MHA;
thiol vs. carboxylic acid 108

4.3.2.3 Addition of Cu^{2+} to a MHA|MHA bilayer 114

4.3.2.4 Formation of a MH capping layer to a MHA|MHA bilayer 116

4.4 Conclusions 120

References 122

CHAPTER 5 Electronic and Chemical Stability of Isocyanide Bound Molecular Wire Monolayers on Palladium Surfaces 128

5.1 Introduction 129

5.2 Experimental 132

5.2.1 Synthesis 132

5.2.2 Sample Preparation 132

5.2.3 Conducting Probe Atomic Force Microscopy (CP-AFM) 134

5.3 Results 134

5.4 Summary and Conclusions 136

5.5 Acknowledgements 139

References 140

Appendix A Supplemental Materials for Chapter 3 146

A.1 Preparation and Characterization of $CD_3(CD_2)_7(CH_2)_8SH$ 147

Appendix B Supplemental Materials for Chapter 5 150

A.1 Preparation and Characterization of 4, 4'- Di(ethynylphenyl)-1-(isocyano) benzene 151

List of Figures

CHAPTER 2

Figure 2.1 (**a**) AFM image of a bare **C12** SAM surface. 1 μm x 1 μm contact mode image showing the surface topography. The image reveals the underlying (111) Au terraces and step edges. (**b**) Unfiltered lateral force image on a smaller area (8 nm x 8 nm) of the bare dodecane thiol SAM reveals the hexagonally packed molecular lattice. (c) Current image of the bare SAM, the image taken with a -1V bias on the surface reveals an insulating film to the limit of our electrical amplifiers (10pA)

23

Figure 2.2. CPAFM image (1μm x 1μm) of a **C12** SAM with 5 eq ML of Au vapor deposited. (**a**) Topography shows the clear structure of the underlying Au (111) substrate, indicating uniform and commensurate growth of a gold film underneath the SAM. (**b**) Current image recorded simultaneously with the topography showing electrical shorts in the film, indicating the presence of Au filaments in the monolayer. (**c**) Typical unfiltered lateral force image (25.4nm x 25.4 nm) shows large ordered areas.

25

Figure 2.3. A schematic of different length Au filaments growing upwards from the Au substrate that would be seen as conduction pathways in the film. As the filaments start to form the tunneling barrier from the surface of the monolayer to the substrate is reduced allowing current to pass to the substrate more readily than before. If the filament is long enough, the AFM tip can come into direct contact with it causing a direct short to the Au substrate.

26

Figure 2.4. CPAFM image (1μm x 1μm) of a dodecane thiol SAM with 10 eq ML of Au vapor deposited. (**a**) Topography shows the clear structure of the underlying Au (111) substrate and the presence of large clusters of Au penetrating the monolayer. (b) Current image recorded simultaneously with the topography reveals electrical shorts in the film at all of the cluster locations.

27

Figure 2.5. CPAFM image (1μm x 1μm) of a dodecane thiol SAM with 20 eq ML of Au vapor deposited. (**a**) Topography shows the structure of the underlying Au (111) substrate, and the presence of large clusters of Au penetrating the monolayer from the Au substrate surrounded by roughened areas around it. (b) Current image recorded simultaneously with the

topography showing shorts in the film at the clusters and the surrounding rough areas of the surface.

28

Figure 2.6. AFM images (1μm x 1μm) of a solution annealed dodecane thiol SAM with (a) 20 and (b) 30 eq ML of Au vapor deposited. The images reveal far fewer cluster formations relative to an unannealed monolayer (figure 2.4).

29

CHAPTER 3

Figure 3.1: Sticking (condensation) coefficient S(θ) of Ti on the SAM surface vs total Ti dose delivered (atoms per SAM molecule) to the SAM surface. (——) determined from a dual QCM experiment, (•) estimated from XPS Ti 2p peak areas, (----) line marking S(θ)=1.0. For details see text.

43

Figure 3.2: Au 4f, C 1s and Ti 2p core level XPS spectra for different coverages of Ti on the CH_3 SAM. XPS Au 4f (left), C 1s (center) and Ti 2p (right) core level spectra as a function of incrementally increasing Ti coverage on the SAM surface, as determined from the total amount of metal delivered to the surface, corrected for the independently measured sticking coefficient. The intensity scales are in arbitrary units and are different for each core level. The dashed lines in the Ti $2p_{3/2}$ peak at 454.7 and 456.4 eV mark the positions for the metallic and carbide species. For details see text.

45

Figure 3.3: IRS C–H (right) and C–D (left) stretching mode spectra for as a $CD_3(CD_2)_7$-$(CH_2)_8$-S-/Au SAM as a function of the incrementally increasing Ti coverage (θ_{Ti}) as determined from the total amount of metal delivered to the surface corrected for the independently measured sticking coefficient. Only selected spectra are assigned θ_{Ti} labels for clarity. For details see text.

47

Figure 3.4: IRS C–H and C–D stretching mode spectra as a function of the incrementally increasing Ti coverage (θ_{Ti}) on a $CD_3(CD_2)_7$-$(CH_2)_8$-S-/Au SAM surface as determined from the total amount of metal delivered to the surface corrected for the independently measured sticking coefficient. The θ_{Ti} = 0 spectrum is shown in terms of the actual intensities, -log[R(0)/Ro], while for $\theta_{Ti} > 0$ difference spectra, defined as

$\Delta A(\theta) \equiv -\log[R(\theta_{Ti})/ R(\theta_o)]$, are shown. Thus, increasing negative peaks signify a loss of the original peak intensity from the bare SAM. The d and r symbols represent methylene and methyl group stretching features, respectively. For details see text.

48

Figure 3.5. AFM images of a bare CH_3 SAM surface. (**A**) 1 μm x 1 μm contact mode image showing the surface topography. The image reveals the underlying (111) Au terraces and step edges. (**B**) The simultaneously recorded lateral force image for the scan in **A**. (**C**) Contact mode imaging in a different, smaller area (17 nm x 17 nm) of the bare SAM reveals the molecular lattice.

51

Figure 3.6. Sequentially taken contact (topography) (**A**, **C**) and lateral force (**B**, **D**) AFM images (1 μm x 1 μm) of a fixed area of a CH_3 SAM surface deposited Ti at θ=1.0. (**A**, **B**): The images show the AFM tip coming into contact with a metal cluster, causing the tip to rise, as seen in the topography, and bend laterally, as seen in the lateral force image. As the tip scans laterally across the surface (in the direction of the top black arrows) a newly contacted cluster is pushed ahead of the tip and typically rolled off to the lower side with the tip passing out of contact to the left. Once the tip is returned to a new position just below the original starting point the next scan line typically recontacts the cluster and moves it again towards the lower left. The arrows point to a region which shows the typical locus of the motion of a cluster being swept off to the lower left during the first scan (faint white spots in contact mode). After completion of the first scan in the indicated area most clusters end up being swept off the image area at the lower left. (**C**, **D**): With the removal of the clusters the topography image regains some sharpness in the resolution of the underlying Au features (**C** vs **A**). In the lateral force image (**D**) note the appearance of small depressions or pits which remain after the clusters are swept off the surface.

52

Figure 3.7. Contact mode AFM images of SAMs after deposited Ti. (**A**) A 1 μm x 1 μm image of a θ = 5 deposition sample after sweeping the surface with the tip for one full scan to remove most of the Ti clusters. Notice the small pits (dark spots) scattered all across the surface which show where the metal clusters originally grew and reacted with the monolayer. The arrows indicate firmly anchored Ti clusters that were not moved by the tip. (**B**) The same region as in **A** but a 0.5 μm x 0.5 μm image which shows the pits in more detail. Typically, the pits are rectangular or oblong as a result of the tip dragging the metal clusters to the left with the initial scan and they vary in depth from ~0.2 – 1.0 nm. (**C**) A 1 μm x 1 μm image for the θ = 5 sample taken in different area

which shows both pits and several of the more firmly anchored remaining clusters. **(D, E, F)** 1 μm x 1 μm images of θ = 10, 20 and 40 samples taken on the first scan after an initial scan to sweep the surface. Note that at these higher coverages the tip is generally unable to move the clusters at the forces used and sweeping has little effect on subsequent scans. The surface density of clusters increases with the amount of deposited metal until at θ = 40 the sample surface is almost entirely covered. The open rectangular patches at θ = 40 appear to be intrinsic to the surface structure since these types of features with varying shapes and sizes are seen scattered on the surfaces for different samples and surface regions. The presence of these features indicates that complete contact of the surface by the deposited metal requires quite high coverages. 55

Figure 3.8: High resolution ToF-SIMS spectra of selected ion peaks at varying total coverages of deposited Ti on the SAM. (**A**) Au^+, (**B**) AuM^+, (**C**), $HAuM^-$; where M ≡ $-S(CH_2)_{16}$, (**D**) $^{48}TiC^+$ and $SC_2H_4^+$. The peak intensities are in arbitrary units with different scales for each spectrum. 58

Figure 3.9: Schematic of the major features arising in the vapor deposition of Ti atoms on a hexadecanethiolate/Au SAM as concluded from the data obtained from multiple in-situ characterization probes. The left hand drawing illustrates for an incoming Ti atom, from left to right, unreactive scattering of an incoming Ti atom off the SAM surface, formation of a carbide reaction product after collision of a Ti atom with the SAM surface, nucleation and growth of a Ti cluster or nanoparticle at a previously reacted surface site, and continued reaction of deposited Ti atoms with $-CH_2-$ units deep into the SAM. The right hand drawing illustrates the possible characteristics that arise in the later stages of deposition where a complete metal overlayer can form. Note the extensive carbide interphase that forms and the likely formation of voids at the SAM/inorganic interface, which would be caused by the highly heterogeneous character of the growth process across the surface. 60

CHAPTER 4

Figure 4.1: Schematic summarizing the formation of multilayers using the method of Ulman and co-workers (reference **Error! Bookmark not defined.**). The steps are: 1.) formation of an α,ω-mercaptoalkanioc acid/Au SAM; 2.) coordination of neighboring CO_2H terminal groups with Cu^{2+} ions; 3.) formation of an overlayer of α,ω-mercaptoalkanoic acid molecules via (RSH)–Cu interaction. Steps 2 and 3 are repeated to build the stack layer by layer.

73

Figure 4.2. Definition of the tilt (θ) and twist (Ψ) angles of an alkane thiol molecule relative to the laboratory coordinate system, where the laboratory coordinate Z is perpendicular to the sample surface, the xyz molecular coordinate system is aligned with the laboratory XYZ system.

79

Figure 4.3. Infrared spectra of the C-H stretching modes for stages **A**-**C** of growth of a bilayer film. Infrared spectra of the **MHA**-Au SAM (A): experiment (—), simulated spectrum (···). The best fit simulation (shown) yields an average chain tilt (θ) of 33±3˚ from surface normal and twists (Ψ) of 52±3˚. Infrared spectra of the **MPA**-Au SAM (A’): experiment (—), simulated spectrum (···). The best fit simulation (shown) yields an average chain tilt (θ) of 32±3˚ from surface normal and twists (Ψ) of 49±3˚. The addition of the Cu^{2+} ions (**B**) causes a slight disordering of the alkane chains observed in both the d^+ and d^- modes as a +2 cm^{-1} shift relative to the bare monolayer (**A**) . The addition of a thiol adlayer causes a shift back to the original frequency (**C**).

85

Figure 4.4. Infrared spectra of the carbonyl stretches for a MHA-Au SAM (**A**) and a MPA-Au SAM (**A’**). The ratio between hydrogen bonding (~1718 cm-1) and non hydrogen bonding (~1741 cm-1) stretching indicates a change in the orientation of the carboxylic acid head groups of the two molecules. (**A’ no HCl**) An example of an uncleaned MPA-Au SAM, the surface has lower intensity carboxylic acid carboxylate peaks than a pure clean MPA surface (A) along with the presence of carboxylate peaks.

87

Figure 4.5. Odd-even effect of an all-trans alkane chains causes a different orientation in the carboxylic acid terminal groups.

87

Figure 4.6. Infrared spectra of the lower frequency region for stages **A-E** of growth for a bilayer film, detailing the changes to the carboxylic acid functional group during the growth of a MHA|MH bilayer.

89

Figure 4.7. The O 1s XPS spectra for stages **A**-**C** of growth for a bilayer film. The bare monolayer (**A**) displays a doublet at 532.6 and 534.0 eV from the two oxygen atoms on the carboxylic acid. The addition of the Cu2+ ions to the carboxylic acid (**B**) forms carboxylate ions in which the oxygen atoms are chemically equivalent and form a singlet at 531.8 eV. (**C**) The addition of a MH adlayer leaves a broad peak at 532.5

eV indicating that the interface has a mix of both the carboxylic acid and the carboxylate functional groups. 90

Figure 4.8. The C 1s XPS spectra for stages **A**-**C** of growth for a bilayer film. 91

Figure 4.9. The Cu 2p 3/2 XPS spectra for stages **B**-**E** of growth for a bilayer film. 92

Figure 4.10. The S 2p XPS spectra for stages **A**-**E** of growth for a bilayer film. 93

Figure 4.12. Schematic of MH bilayer on an α,ω-mercaptoalkanioc acid/Au SAM. 97

Figure 4.12. Infrared spectra of a deuterated MH on a MHA-Au SAM: experiment (—), simulated spectrum (···). The calculated spectra yields an average chain tilt of 41±3˚ from surface normal and twists of 41±3˚. 98

Figure 4.13. Infrared spectra of the C-D stretching modes for the C-E stages of growth of a bilayer film. 102

Figure 4.14. Infrared spectra for the 5 steps of growth of a trilayer film. 107

Figure 4.15. Schematic of two possible α,ω-mercaptoalkanioc orientations for a MHA bilayer on Au. 108

Figure 4.16. Infrared spectra for the first 3 steps of growth for both a bilayer and a trilayer film. (**A**) the bare MHA monolayer shows the carboxylic acid stretches of the monolayer, while (**B**) the Cu^{2+} coordinated MHA surface results in the complete disappearance of the carboxylic acid groups replaced by carboxylate groups. The addition of a MH adlayer to the Cu^{2+} coordinated MHA surface (**C**) results in the complete loss of both carboxylate stretches and the replacement of the carboxylic acid stretches. The addition of MHA to a Cu^{2+} coordinated MHA surface (**F**) reveals the presence of both carboxylate ions and carboxylic acid components. 110

Figure 4.17. (**a**) Schematic of the orientation of the copper carboxylate complex formed on the surface after the initial addition of Cu^{2+} ions to a α,ω-mercaptoalkanioc SAM. (**b**) Schematic of the structure of the copper carboxylate complex formed if one or both species are unconstrained geometrically, i.e. bound to a surface. (c) Directions of the symmetric and antisymmetric vibrations of a carboxylate ion.

111

Figure 4.18. The XPS Cu 2p 3/2 region spectra for the F-H stages of growth for a trilayer film.

113

Figure 4.19. The XPS S 2p region spectra and a fitting of the 3 different sulfur components for a bilayer of MHA.

114

Figure 4.20. XPS spectra for steps A, F, H and H" of growth for a trilayer film.

119

CHAPTER 5

Figure 5.1. Bonding structures for OPE-NC SAMs on Au (I) and Pd (II or III)

131

Figure 5.2. Chemical structure of OPE-NC

132

Figure 5.3. CP-AFM I-V scans for a representative OPE-NC/Pd SAM before and after 18 hr ambient exposure. The curves represent an average of 186 and 240 measurements for the fresh and exposed SAM, respectively with respective standard deviations of ±60 and ±8 picoAmps. For details see text.

136

Figure 5.4. Schematic illustration of the main chemical and structural features of the OPE-NC SAMs on Pd substrates prepared under rigorous conditions with minimum exposure to laboratory ambient and after storage in laboratory ambient. The illustration shows the same type of tilted molecule structure but with an initial bridge bonded isocyanide group which slowly converts to a polymeric species over time at ambient

temperature. The headgroups, while stable to oxidation reactions, slowly convert with time to a poly(imine) type of polymer film with associated loss in organization and packing of the molecules. 137

List of Tables

Chapter 4

Table 4.1: Selected Infrared Mode Assignments for Alkanethiolate and Mercaptoalkanoic Acid SAMs 82

Table 4.2: Explanation of figure abbreviations used for each step of the multilayer films growth. a) prime notation used to indicate systems constructed with monolayers of MPA, such as **A'** for a bare monolayer of MPA. 83

Table 4.3: Thickness and contact angle measurements for bilayers of MHA|MH (A-E) and MPA|MH (A'-E') for each step of their respective MH bilayer growth. 84

Acknowledgements

Many individuals have provided me with guidance and support here at Penn State University who I am very grateful for the opportunity to work with. I would like to acknowledge and thank my advisor Dr. David Allara. He has provided an excellent work atmosphere where I was encouraged to expand my scientific knowledge to many different areas and techniques. Not only does the lab he provided have many of the most useful equipment I ever needed, but when more specialized tools were needed a way to use them was always found due in great part to his help. Additionally I would like to thank the members of the Allara group for their advice and friendship over the years. Much of what I have accomplished would not be possible with out their help.

Several funding agencies have provided financial support and I would like to acknowledge them here. The National Science Foundation (NSF), the Defense Advanced Research Project Agency (DARPA), the Air Force Office of Scientific Research, the Naval Research Laboratories, the Office of Naval Research, the Army Research Office, the Department of Energy, the Cornell High Energy Synchrotron Source (CHESS), and the Penn State NSF MRSEC program.

I would also like to thank my family for always supporting my decisions, their encouragement, and providing for me in many ways during my life. I would also like to thank the many friends I've made here for there support and friendship over my years here at Penn State University.

Specific scientific contributions to individual Chapters

Chapter 3: Zihua Zhu from Dr. Nicholas Winograd research group provided the ToF-SIMS data. Dr. Sundarajan Upilli and Timothy Tighe synthesized the $D_3C(CD_2)_7(CH_2)_8SH$ compound utilized in the IR portion of this study and contributed the IR and XPS experiments respectively

Chapter 4: Dr. Sundarajan Upilli synthesized the 15-mercaptopentadecanethiol and deuterated hexadecanethiol compounds used in this study.

Chapter 5: Dr. Jawad Naciri of the Naval Research Laboratory and Dr. Sundarajan Upilli synthesized portions of the OPE-NC compound utilized in this study. While not directly included in this thesis, Dr. Joshua Stapleton contributed the IR, XPS and AFM studies that motivated the study.

Chapter 1

Introduction

1.1 Introduction to Molecular Electronics

Information technologies have revolutionized the modern world and continue to do so, in more and more dramatic ways, as they increased in processing power. This increase in processing power is driven technologically by the industry's ability to continually reduce the size of integrated circuits. However, as the features continue to diminish in size, the costs of meeting the increasing demands on manufacturing tolerances increase as well. In fact, facilities are expected to reach 100 billion dollar operating and construction costs by 2010.[1] In addition, physical limits on silicon technologies[2] threaten to bring an end the exponential growth in computing speed observed over the past 35 years.[3,4] These problems have lead to the development of molecular electronics as a possible alternate computing technology.

Molecular electronics is defined as the utilization of molecular properties for the construction of an electrical device.[5] Gorman and Carroll define the following fundamental requirements for a molecular system to be considered a device.[6] 1) The molecules utilized must perform some electrical function, such as a switching or a rectification. 2) The molecules and device must be electrically and chemically stable. 3) The molecules must perform the electronic task reversibly. 4) The molecules must remain in a physical location in space. 5) There must be a way to interact with the component and exchange information to the outside world. These requirements are the current focus of present molecular electronic research.[6,7]

In order to test any molecules of interest for use in molecular electronic devices (MEDs), requirements 4 and 5 must first be met. A variety of device configurations have

been utilized to immobilize and electrically investigate different molecules in an attempt to meet both requirements. They differ widely in electrode materials employed, means of electrical contact to the molecules, and the number of molecules used.[8 - 50] One commonality for many of these device designs, however, is the utilization of self-assembly of electronically active organic molecules on metal surfaces.

The formation of self-assembled monolayers (SAMs), discovered by Allara and Nuzzo,[51] involves a simple and efficient one step method of forming ordered monolayers on a surface.[52] SAMs have been used to form organic monolayers on both metal[51-57] and semiconductor[52,58-60] substrates, using a variety of attachment mechanisms.[51,52,54,60-66] The best studied system utilizes thiol-Au chemistry.[51] Thiol-Au SAM formation involves placing the substrate in a dilute (~mM) solution of the adsorbate molecule in question. The adsorbing molecules will then attach to the substrate via a chemical or ionic interaction depending on the system. After a short time (typically less than 24 hrs) in the solution a dense and often molecularly ordered monolayer forms on the substrate. The substrate can then be removed from solution and cleaned via solution rinsing. The surface is then ready for characterization and/or device testing. This process has the significant advantage that it doesn't require 'clean room' facilities making it a relatively inexpensive process, compared to conventional silicon technologies utilized in integrated circuits. The main advantage in using SAM chemistry for MEDs construction, is that by chemically attaching the appropriate functional group to a proposed molecule of interest, the molecule can form a physical and electrical contact to a conducting substrate.

While much work has been done on many differing MED configurations[8-50] a significant variation in the amount of current passing through similar molecules has been

reported for different devices.[28,67] The variation is significant enough, often differing by orders of magnitude, that it can not be dismissed as uncertainties in the measurements. A review of the literature by Salomon and coworkers,[67] concluded that this variation is likely due to fundamental differences between the electrical contacts formed with the top of the SAM molecules used in these devices. The lack of fundamental knowledge about the nature of electrical contacts made to molecules has motivated the research reported in this thesis.

1.2 Molecular Electrical Contacts Formed via Metal Vapor Deposition

The vacuum deposition of metal layers on organic thin films is a widely used process developed for many applications ranging from electronic devices to barrier coatings. The outcomes of any particular deposition are typically very difficult to predict because of the lack of fundamental information on the complex, intertwined chemical and physical processes that can be involved in the interface formation and metal overlayer growth. As a means of building the fundamental rules underlying these complex phenomena, recent efforts have focused on using the chemically and physically well-defined structures of self-assembled monolayers (SAMs) as the organic substrates.[68-75] These structures not only provide model systems but have become highly relevant because of their recent applications in molecular electronic devices, where vapor deposited metal contacts are used in a base electrode-molecule-metal structure[29-50] where the exact nature of the contact interface and metal morphology can profoundly affect device behavior.

When metal atom vapors impinge on organic substrates a wide range of behaviors are possible, many often undesired, including severe chemical degradation, clustering of the metal into heterogeneous overlayers with discontinuous interfaces, penetration deep into the organic matrix and even scattering from the surface with no condensation. For a number of applications, particularly molecule-based electronics using top metal contact devices it is desirable to achieve reproducibly uniform deposition across the surface with subsequent growth of a dense, uniform metal overlayer. This method of forming electrical contact to molecules is highly appealing since it is an easily scaled process. The top metal can vary from noble metals, such as gold, to very reactive metals, such as titanium. The work conducted in chapters 2 and 3 provides a study on the vapor depositions of Au and Ti, respectively, onto alkanethiolate/Au monolayers in order to better understand the top metal contact formed by metal depositions on SAMs. The results illustrate the nature of the interactions between the metals and the alkanethiolate films and indicate some likely causes of device failure in MEDs constructed using the two different metals.

1.3 Molecular Electrical Contacts Formed on nanofabricated metal gaps

The use of self-assembled, multilayer molecular films as precision spacers ("molecular rulers") for lithographic processing, has recently been reported.[76,77,78,79] These reports indicate that appropriate molecular ruler films (MRFs), in conjunction with liftoff, or other standard lithographic techniques, can be used on surfaces with nominal micrometer scale patterns, previously created by standard lithographic processing (e.g., photolithography), to create final topographical features in the 1-100 nm width range. Such a capability, if sufficiently precise and generally applicable, would fill a

longstanding gap in patterning by providing designed, precision dimensions down to the molecular scale which could then be used as MEDs.

The present state-of-the art is based on alkanethiol-gold chemistry and thus presently is limited to patterning gold features,[76-7779] though suitable chemistries should allow extensions to other materials. In detail, multilayer stacks of self-assembled monolayers (SAMs), each with a predesigned thickness, are formed layer by layer on a foundation SAM of an ω-carboxyalkanethiolate SAM on Au{111} [$HO_2C(CH_2)_nS$–/Au].[80] The foundation SAM is prepared on a surface with gold features, e.g., μm-width gold posts or lines on a silicon oxide substrate, with the SAM forming selectively on, and conformal to, the gold features. While a number of methods are available for forming conformal multilayers,[81-90] the current method is based on the method of Ulman and co-workers[81] which uses stacks of α,ω-mercaptoalkanoic acid layers ligated at their interfaces by copper ions. Once the foundation SAM is formed, iterations of layered growth, with selected constituent molecules of specific molecular lengths the thickness of the final stack, in principle, can be precisely controlled. By vapor depositing a metal film on the substrate a gap can be formed between the original gold features and the newly deposited metal, with the separation of the gaps being determined by the selected thickness of the MRF stack.

The success of MRFs in forming precision nanometer scale features with sharp, highly replicating feature edges and gap widths depends critically on the ability to control the precision of the thickness and surface roughness of the MRFs as well as the interfacial topography and adhesive interaction of the deposited metal overlayer with the molecular films. In this regard, the growth of the α,ω-mercaptoalkanoic acid/Cu^{2+} MRFs

has proven to be problematic. For example, recent work has shown that while <10 nm junctions can be fabricated with MRF liftoff processing, poor reproducibility in the electronic characteristics of the resulting structures limits the quality of the information obtainable.[25] In similar work by Weiss and co-workers,[79] the rate of successfully nanofabricated separation using multilayer lithographic techniques decreased as the area of the interface increased.

In order to reliably control the final feature characteristics a better understanding of the details of the multilayer growth mechanisms and intermediate layer structures is required. Given our long term interest in producing highly precise gaps and features for building MEDs and other applications, it was of interest to study the details of MRF structures and their growth mechanisms. In chapter 4, the nature of the interfacial layers and the chemical reactions that govern them, is studied by use of infrared reflection spectroscopy (IRS), X-ray photoelectron spectroscopy (XPS), and single wavelength ellispsometry SWE, along with other ancillary probes. The results of this study lead to a better understanding of the growth of multilayer films and provide details for better procedural processes to increase the quality of these films.

1.4 Molecular Devices that Utilize Alternate Chemical Binding to the Substrate

With the increased interest in fabricating electronic devices based on molecules and molecular assemblies, it is critically important to understand the detailed way in which the molecules bond and organize at electrode surfaces. One family of candidate structures used extensively in recent MED studies is based on SAMs made from various derivatives of 4,4'-di(phenylene-ethynylene)benzenethiol[91] [commonly referred to as

oligo(phenylene-ethynylene)thiol or OPE-SH]. It has been shown that the current-voltage behavior of these molecules can be altered by changing ring substituents.[32-35] Further flexibility in tailoring the electrical properties of the SAMs is possible by altering the headgroup used to anchor the molecule to the base electrode and by varying the electrode material.[92] Furthermore, there has been little work done on the assembly of organic molecules on alternate metals such as palladium, an attractive alternate for device contacts,[93] despite the fact that electrical measurements of isocyanide SAMs bound on Pd appear to exhibit improved junction properties over those on Au.[50]

Given the reports that -NC/noble metal junctions exhibit lower conduction barriers than the corresponding thiol-based junctions,[50] it is important for molecular electronics applications to establish in detail the attachment mechanism(s) of isocyanide terminated device type molecules since the attachment mode could affect the molecular orientation and packing. The nature of the ArNC-metal bond (where Ar = an aryl group, the common constituent structure of device molecules) is complicated by possible multiple bonding interactions with the metal substrate. The study presented in chapter 5 is a CP-AFM study of the chemical and electrical stability of the ArNC-Pd metal bonds. Done in tandem with other surface techniques performed by Stapleton *et al,*[94] the studies illustrate the nature of the isocyanide bond to Pd surfaces and reveal that short exposures of the surface to ambient conditions will degrade the chemical bonding between the isocyanide and the Pd.

References:

[1] Tour J.M. *Molecular Electronics: Commercial Insights, Chemistry, Devices, Architecture and Programming*; World Scientific: River Edge, NJ, 2003.

[2] Martin, S.J.; Godschalx, J.P.; Mills, M.E.; Shaffer, E.O.; Townsend, P.H. *Advanced Materials* **2000,** 12, 1769.

[3] Observation based on processing power of integrated circuits designed by intel see: http://www.intel.com/research/silicon/mooreslaw.htm

[4] Moore, G.E. *Electronics* **1965,** 38, 114-117.

[5] Darpa uses a similar definition see: http://www.darpa.mil/MTO/mole/

[6] Carroll, R. L.; Gorman, C. B. *Angewandte Chemie-International Edition* **2002,** *41*(23), 4379-4400.

[7] Mantooth, B. A.; Weiss, P. S. *Proceedings of the IEEE* **2003,** *91*(11), 1785-1802.

[8] Wang, W. Y.; Lee, T.; Reed, M. A. *Physical Review B* **2003,** *68*(3).

[9] Selzer, Y.; Salomon, A.; Cahen, D. *Journal of Physical Chemistry B* **2002,** *106*(40), 10432-10439.

[10] Chabinyc, M. L.; Chen, X. X.; Holmlin, R. E.; Jacobs, H.; Skulason, H.; Frisbie, C. D.; Mujica, V.; Ratner, M. A.; Rampi, M. A.; Whitesides, G. M. *Journal of the American Chemical Society* **2002,** *124*(39), 11730-11736.

[11] Beebe, J. M.; Engelkes, V. B.; Miller, L. L.; Frisbie, C. D. *Journal of the American Chemical Society* **2002,** *124*(38), 11268-11269.

[12] Kushmerick, J. G.; Holt, D. B.; Yang, J. C.; Naciri, J.; Moore, M. H.; Shashidhar, R. *Physical Review Letters* **2002,** *89*(8).

---

[13] Reichert, J.; Ochs, R.; Beckmann, D.; Weber, H. B.; Mayor, M.; von Lohneysen, H. *Physical Review Letters* **2002,** *88*(17).

[14] Collier, C. P.; Wong, E. W.; Belohradsky, M.; Raymo, F. M.; Stoddart, J. F.; Kuekes, P. J.; Williams, R. S.; Heath, J. R. *Science* **1999**, *285* , 391-394.

[15] Cui, X. D.; Primak, A.; Zarate, X.; Tomfohr, J.; Sankey, O. F.; Moore, A. L.; Moore, T. A.; Gust, D.; Harris, G.; Lindsay, S. M. *Science* **2001,** *294*(5542), 571-574.

[16] Mceuen, P. L. *Physics World* **2000,** *13*(6), 31-36.

[17] Vilan, A.; Shanzer, A.; Cahen, D. *Nature* **2000,** *404*(6774), 166-168.

[18] Bumm, L. A.; Arnold, J. J.; Charles, L. F.; Dunbar, T. D.; Allara, D. L.; Weiss, P. S. *Journal of the American Chemical Society* **1999,** *121*(35), 8017-8021.

[19] Slowinski, K.; Fong, H. K. Y.; Majda, M. *Journal of the American Chemical Society* **1999,** *121*(31), 7257-7261.

[20] Park, H.; Lim, A. K. L.; Alivisatos, A. P.; Park, J.; Mceuen, P. L. *Applied Physics Letters* **1999,** *75*(2), 301-303.

[21] Dekker, C. *Physics Today* **1999,** *52*(5), 22-28.

[22] Slowinski, K.; Chamberlain, R. V.; Miller, C. J.; Majda, M. *Journal of the American Chemical Society* **1997,** *119*(49), 11910-11919.

[23] Dhirani, A.; Lin, P. H.; GuyotSionnest, P.; Zehner, R. W.; Sita, L. R. *Journal of Chemical Physics* **1997,** *106*(12), 5249-5253.

[24] Joachim, C.; Gimzewski, J. K. *Chemical Physics Letters* **1997,** *265*(3-5), 353-357.

[25] McCarty, G. S. *Nano Lett.* **2004,** *4*(8), 1391-1394.

[26] Selzer, Y.; Cabassi, M. A.; Mayer, T. S.; Allara, D. L. *Nanotechnology* **2004,** *15*(7), S483-S488.

[27] Selzer, Y.; Cabassi, M. A.; Mayer, T. S.; Allara, D. L. *Journal of the American Chemical Society* **2004,** *126*(13), 4052-4053.

[28] Selzer, Y.; Cai, L. T.; Cabassi, M. A.; Yao, Y. X.; Tour, J. M.; Mayer, T. S.; Allara, D. L. *Nano Letters* **2005,** *5*(1), 61-65.

[29] Zhou, C.; Deshpande, M. R.; Reed, M. A.; Jones, L.; Tour, J. M. *Appl. Phys. Lett.* **1997**, *71*, 611-613.

[30] Collet, J.; Vuillame, D. *Appl. Phys. Lett.* **1998**, *73*, 2681-2693.

[31] Allara, D. L.; Dunbar, T. D.; Weiss, P. S.; Bumm, L. A.; Cygan, M. T.; Tour, J. M.; Reinerth, W. A.; Yao, Y.; Kozaki, M.; Jones, L. *Ann. N. Y. Acad. Sci.* **1998**, *852*, 349-370.

[32] Chen, J.; Reed, M. A.; Rawlett, A. M.; Tour, J. M. *Science* **1999**, *286*, 1550-1552.

[33] Chen, J.; Wang, W.; Reed, M. A.; Rawlett, A. M.; Price, D. W.; Tour, J. M. *Appl. Phys. Lett.* **2000**, *77*, 1224-1226.

[34] Reed, M. A.; Chen, J.; Rawlett, A. M.; Price, D. W.; Tour, J. M. *Appl. Phys. Lett.* **2001**, *78*, 3735-3737.

[35] Rawlett, A. M.; Hopson, T. J.; Nagahara, L. A.; Tsui, R. K.; Ramachandran, G. K.; Lindsay, S. M. *Appl. Phys. Lett.* **2002**, *81*, 3043-3045.

[36] Collier, C.P.; Mattersteig, G.; Wong, E.W.; Luo, Y.; Beverly, K.; Sampaio, J.; Raymo, F.M.; Stoddart, J.F.; Heath, J.R.; *Science*, **2000**, *289*, 1172-1175.

[37] Collier, C. P.; Jeppesen, J. O.; Luo, Y.; Perkins, J.; Wong, E. W.; Heath, J. R.; Stoddart, J. F. *J. Am. Chem. Soc.* **2001**, *123*, 12632-12641.

[38] Metzger, R. M.; Xu, T.; Peterson, I. R. *J. Phys. Chem. B* **2001**, *105*, 7280-7290.

[39] Chen, J.; Reed, M. A. *Chem. Phys.* **2002**, *281*, 127-145.

[40] Chang, S. C.; Li, Z. Y.; Lau, C. N.; Larade, B.; Williams, R. S. *Appl. Phys. Lett.* **2003**, *83*, 3198-3200.

[41] Vuillaume, D.; Lenfant, S. *Microelectron. Eng.* **2003**, *70*, 539-550.

[42] Lenfant, S.; Krzeminski, C.; Delerue, C.; Allan, G.; Vuillaume, D. *Nano Letters* **2003** , *3*, 741-746.

[43] McCreery, R.; Dieringer, J.; Solak, A. O.; Snyder, B.; Nowak, A. M.; McGovern, W. R.; DuVall, S. *J. Am. Chem. Soc.* **2003**, *125*, 10748-10758.; McCreery, R.; Dieringer, J.; Solak, A. O.; Snyder, B.; Nowak, A. M.; McGovern, W. R.; DuVall, S. *J. Am. Chem. Soc.* **2004**, *126*, 6200.

[44] de Boer, B.; Frank, M. M.; Chabal, Y. J.; Jiang, W. R.; Garfunkel, E.; Bao, Z. *Langmuir* **2004**, *20*, 1539-1542.

[45] Jung, G. Y.; Ganapathiappan, S.; Li, X.; Ohlberg, D. A. A.; Olynick, D. L.; Chen, Y.; Tong, W. M.; Williams, R. S. *Appl. Phys. A* **2004**, *78*, 1169-1173.

[46] McCreery, R. L. *Chem. Mater.* **2004**, *16*, 4477-4496.

[47] Stewart, D. R.; Ohlberg, D. A. A.; Beck, P. A.; Chen, Y.; Williams, R. S.; Jeppesen, J. O.; Nielsen, K. A.; Stoddart, J. F. *Nano Letters* **2004**, *4*, 133-136.

[48] Lau, C. N.; Stewart, D. R.; Williams, R. S.; Bockrath, M. *Nano Letters* **2004**, *4*, 569-572.

[49] Haick, H.; Ambrico, M.; Ghabboun, J.; Ligonzo, T.; Cahen, D. *Phys. Chem. Chem. Phys.* **2004**, *6*, 4538-4541.

[50] Chen, J.; Calvet, L. C.; Reed, M. A.; Carr, D. W.; Grubisha, D. S.; Bennett, D. W. *Chem. Phys. Lett.* **1999**, *313*, 741-748.

---

[51] Nuzzo, R.G.; Allara, D.L. *J Journal of the American Chemical Society* **1983,** *105*, 4481-4483.

[52] Ulman, A. *Chemical Reviews* **1996,** *96*(4), 1533-1554.

[53] Love, J. C.; Wolfe, D. B.; Haasch, R.; Chabinyc, M. L.; Paul, K. E.; Whitesides, G. M.; Nuzzo, R. G. *Journal of the American Chemical Society* **2003,** *125*(9), 2597-2609.

[54] Allara, D.L.; Nuzzo, R.G. *Langmuir* **1985,** 9, 1046-1050.

[55] Shimazu, K.; Kaneda, K.; Kita, H. *Bulletin of the Chemical Society of Japan* **1994,** *67*(8), 2069-2074.

[56] Demoz, A.; Harrison, D. J. *Langmuir* **1993,** *9*(4), 1046-1050.

[57] Tao, Y. T. *Journal of the American Chemical Society* **1993,** *115*(10), 4350-4358.

[58] Nakagawa, O. S.; Ashok, S.; Sheen, C. W.; Martensson, J.; Allara, D. L. *Japanese Journal of Applied Physics Part 1-Regular Papers Short Notes & Review Papers* **1991,** *30*(12B), 3759-3762.

[59] Han, S. M.; Ashurst, W. R.; Carraro, C.; Maboudian, R. *Journal of the American Chemical Society* **2001,** *123*(10), 2422-2425.

[60] Stewart, M. P.; Maya, F.; Kosynkin, D. V.; Dirk, S. M.; Stapleton, J. J.; McGuiness, C. L.; Allara, D. L.; Tour, J. M. *Journal of the American Chemical Society* **2004,** *126*(1), 370-378.

[61] Monnell, J. D.; Stapleton, J. J.; Jackiw, J. J.; Dunbar, T.; Reinerth, W. A.; Dirk, S. M.; Tour, J. M.; Allara, D. L.; Weiss, P. S. *Journal of Physical Chemistry B* **2004,** *108*(28), 9834-9841.

[62] Pellerite, M. J.; Dunbar, T. D.; Boardman, L. D.; Wood, E. J. *Journal of Physical Chemistry B* **2003,** *107*(42), 11726-11736.

---

[63] Nakamura, T.; Yasuda, S.; Miyamae, T.; Nozoye, H.; Kobayashi, N.; Kondoh, H.; Nakai, I.; Ohta, T.; Yoshimura, D.; Matsumoto, M. *Journal of the American Chemical Society* **2002,** *124*(43), 12642-12643.

[64] Han, W. H.; Li, S. M.; Lindsay, S. M.; Gust, D.; Moore, T. A.; Moore, A. L. *Langmuir* **1996,** *12*(23), 5742-5744.

[65] Henderson, J. I.; Feng, S.; Bein, T.; Kubiak, C. P. *Langmuir* **2000,** *16*(15), 6183-6187.

[66] Meyer, G. J.; Lisensky, G. C.; Ellis, A. B. *Journal of the American Chemical Society* **1988,** *110*(15), 4914-4918.

[67] Salomon, A.; Cahen, D.; Lindsay, S.; Tomfohr, J.; Engelkes, V. B.; Frisbie, C. D. *Advanced Materials* **2003,** *15*(22), 1881-1890.

[68] Jung, D. R.; Czanderna, A. W. *Crit. Rev. Solid State* **1994**, *19*, 1-54.

[69] Herdt, G. C.; King, D. E.; Czanderna, A. W. *Z. Phys. Chem.* **1997**, *202*, 163-196.

[70] Hooper, A.; Fisher, G. L.; Konstadinidis, K.; Jung, D.; Nguyen, H.; Opila, R.; Collins, R. W.; Winograd, N.; Allara, D. L. *J. Am. Chem. Soc.* **1999**, *121*, 8052-8064.

[71] Fisher, G. L.; Hooper, A. E.; Opila, R. L.; Allara, D. L.; Winograd, N. *J. Phys. Chem. B* **2000**, *104*, 3267-3273.

[72] Fisher, G. L.; Walker, A. V.; Hooper, A. E.; Tighe, T. B.; Bahnck, K. B.; Skriba, H. T.; Reinard, M. D.; Haynie, B. C.; Opila, R. L.; Winograd, N.; Allara, D. L. *J. Am. Chem. Soc.* **2002**, *124*, 5528-5541.

[73] Walker, A. V.; Tighe, T. B.; Reinard, M. D.; Haynie, B. C.; Allara, D. L.; Winograd, N. *Chem. Phys. Lett.* **2003**, *369*, 615-620.

[74] Walker, A. V.; Tighe, T. B.; Stapleton, J.; Haynie, B. C.; Upilli, S.; Allara, D. L.; Winograd, N. *Appl. Phys. Lett.* **2004**, *84*, 4008-4010.

[75] Walker, A. V.; Tighe, T. B.; Cabarcos, O. M.; Reinard, M. D.; Haynie, B. C.; Uppili, S.; Winograd, N.; Allara, D. L. *J. Am. Chem. Soc.* **2004**, *126*, 3954-3963.

[76] Hatzor, A.; Weiss, P. S. *Science* **2001,** *291*(5506), 1019-1020.

[77] Anderson, M. E.; Tan, L. P.; Tanaka, H.; Mihok, M.; Lee, H.; Horn, M. W.; Weiss, P. S. *J. Vac. Sci. Technol., B.* **2003,** *21*(6), 3116-3119.

[78] Anderson, M. E.; Smith, R. K.; Donhauser, Z. J.; Hatzor, A.; Lewis, P. A.; Tan, L. P.; Tanaka, H.; Horn, M. W.; Weiss, P. S. *J. Vac. Sci. Technol., B.* **2002,** *20*(6), 2739-2744.

[79] Anderson, M. E.; Srinivasan, C.; Jayaraman, R.; Weiss, P. S.; Horn, M. W. *Microelectron. Eng.* **2005,** *78-79* 248-252.

[80] Nuzzo, R.G.; Dubois, L.H.; Allara, D.L. *J. Am. Chem. Soc*. **1990**, *112*, 558-569.

[81] Evans, S. D.; Ulman, A.; Goppertberarducci, K. E.; Gerenser, L. J. *J. Am. Chem. Soc*. **1991,** *113*(15), 5866-5868.

[82] Freeman, T. L.; Evans, S. D.; Ulman, A. *Langmuir* **1995,** *11*(11), 4411-4417.

[83] Brust, M.; Blass, P. M.; Bard, A. J. *Langmuir* **1997,** *13*(21), 5602-5607.

[84] Auer, F.; Nelles, G.; Sellergren, B. *Chem-Eur J.* **2004,** *10*(13), 3232-3240.

[85] Cheng, W. L.; Dong, S. J.; Wang, E. K. *Chem. Mater.* **2003,** *15*(13), 2495-2501.

[86] Lee, H.; Kepley, L. J.; Hong, H. G.; Mallouk, T. E. *J. Am. Chem. Soc*. **1988,** *110*(2), 618-620.

[87] Lee, H.; Kepley, L. J.; Hong, H. G.; Akhter, S.; Mallouk, T. E. *J. Phys. Chem.* **1988,** *92*(9), 2597-2601.

[88] Tillman, N.; Ulman, A.; Penner, T. L. *Langmuir* **1989,** *5*(1), 101-111.

[89] Ansell, M. A.; Zeppenfeld, A. C.; Yoshimoto, K.; Cogan, E. B.; Page, C. J. *Chem. Mater.* **1996,** *8*(3), 591-594.

---

[90] Zhang, W. W.; Lu, C. S.; Zou, Y.; Xie, J. L.; Ren, X. M.; Zhu, H. Z.; Meng, Q. J. *J. Colloid and Interface Sci.* **2002,** *249*(2), 301-306.

[91] Tour, J. M. *Acc. Chem. Res.* **2000**, *33*, 791-804.

[92] Seminario, J. M.; Zacarias, A. G.; Tour, J. M. *J. Am. Chem. Soc.* **1999**, *121*, 411-416.

[93] Love, J.C.; Wolfe, D.B.; Haasch, R.; Chabinyc, M.L.; Paul, K.E.; Whitesides, G.M.; Nuzzo, R.G. *J. Am. Chem. Soc.* **2003**, *125*, 2597-2609.

[94] Stapleton, J.J.; Daniel, T.A.; Uppili S; Cabarcos O.M. Naciri J.; Shashidhar R.; Allara D.L. (Submitted for publication).

Chapter 2

Evolution of the Interface and Metal Film Morphology in the Vapor Deposition of Au on Dodecanethiolate Monolayers on Au {111}

2.1 Introduction

An important aspect of molecular electronics, continues to be the nature of the contacts formed by vapor deposition of metals onto self-assembled monolayers. The desired characteristics of these top contacts depend upon avoiding problems such as shorting failures via metal penetration, poorly formed contacts, and the presence of metal filaments, which can provide erratic conductance behavior upon bias cycling, in some cases including switching and memory artifacts. The use of molecules as the active component in electronic devices has made significant advances in recent years.[1,2] Many different designs have been utilized to create molecule based devices.[3-11] A typical size scaleable device is fabricated via the vapor deposition of metals onto self-assembled monolayers (SAMs) to prepare a metal/SAM/Au substrate sandwich structures.[3-6] However there is significant device to device variation attributed to a lack of fundamental data on the nature of the top metal contacts structure and its interaction with the SAM.[12]

Many studies have been performed on alkanethiolate SAM structures, which are commonly used as test SAMs for molecule-based devices.[12] Theoretical calculations show that for alkanethiolate films the interactions between the molecules consist primarily of van der Waals forces at room temperature, and that thermal energy causes small movements of the film molecules on the Au substrate.[13,14] This movement results in temporary vacancies in the monolayer. The sizes of which are large enough for metal atoms to diffuse from the vacuum interface to the Au/S interface.[15] Previous reports of Au vapor deposited on octadecane thiol SAMs suggest that the Au atoms penetrate through the monolayer and form a commensurate structure with the underlying Au substrate.[16,17] However, the studies were limited to very low Au coverages ($\theta_{Au}<1$).

In this study we apply *in-situ* conducting probe atomic force microscopy (CP-AFM) to characterize the topography and electrical characteristics of samples prepared by vapor deposition of gold atoms onto ambient temperature SAMs prepared via chemisorption of the dodecane thiol on Au{111}/mica. After vacuum deposition of controlled coverages of Au, ranging from θ_{Au} = a few up to 30 Au atoms/molecule, the samples were transferred *in vacuo* to the analysis chamber where both topographical and electrical current measurements were done simultaneously on micron scale areas. The use of vacuum conditions minimizes contamination of the sample and at the metal/SAM interface. The combination of the two imaging modes reveals the partitioning between metal overlayer clustering/growth and penetration to the underlying Au-S interface, with and without intervening metal filaments.

For a dodecane thiol SAM, the majority of the deposited Au penetrates uniformly across the surface to the underlying Au/S substrate. However, some Au at the surface forms clusters which provide a conduction path to the gold substrate. The Au atoms are theorized to land and move laterally across the surface of the SAMs until they can find a diffusion pathway through the monolayer. Two competing pathways through the monolayer are proposed, one through temporary vacancies in the ordered regions of the monolayer, and another through defect sites in the monolayer. Diffusion through these defect sites in a monolayer is found to occur at a much faster rate than through temporary vacancies. This leads to the formation of filaments that grow from the surface of the Au substrate through the monolayer forming electrical shorts.

2.2 Experimental

2.2.1 Sample Preparation.

Dodecanethiol (**C12** $CH_3(CH_2)_{11}SH$) (98% Aldrich) was used as received. The SAMs were formed on a hydrogen flame annealed Au(111) substrates on mica (Molecular Imaging, Tempe, AZ). The preparation and characterization of the $H_3C(CH_2)_{11}S$-/Au SAMs has been described in detail previously[18-22] and is summarized briefly here. Self-assembly of well-organized monolayers was achieved by immersing the Au substrates into millimolar solutions of the dodecane thiol molecule in absolute ethanol for ~1 day, at ambient temperature. To increase monolayer ordering, the solution was heated to 70°C for 1 hour and cooled to room temperature before the sample was removed.[23] The samples were then thoroughly rinsed with ethanol, acetone, and dichloromethane to remove physisorbed materials from the surface and finally dried under a stream of N_2 gas. All samples were immediately mounted and stored in the UHV AFM chamber until they were used.

2.2.2 Metal Depositions

The depositions were performed using resistive heating of a Tungsten basket heater (B12B-.040W type, R.D. Mathis, Long Beach, CA). The Au (≥ 99.99 % Refining Systems, Las Vegas, NV) was baked at least 1 hour prior to depositions to remove impurities in the gold. The throw distance was ~26 in. and the sample temperatures remained near ~25 °C under the deposition conditions. During the deposition, the rate was maintained at 1.0±0.1 equivalent monolayers per minute and the pressure remained $<5 \times 10^{-8}$ torr. The mass of metal atoms delivered to the SAM surfaces was measured by placing quartz crystal microbalance (QCM) crystals with gold coated electrodes in the path of the vapor flux. Geometric factor corrections (tooling factors) for the placement of the QCM crystal relative to the sample and absolute fluxes were calibrated using AFM

measured film thicknesses at the sample and QCM crystal locations. Readout/controller units were obtained from Sigma Instruments (SQM-160, maximum error ± 7 %). The amount of metal delivered per unit area to the samples was determined from the QCM measurements as mass per unit area (ρ_A). For ease in data analysis and interpretation, an equivalent coverage of metal atoms per SAM molecule (θ_{Au}) was calculated using the ρ_A values and the molecular density of 4.6 molecules·nm^{-2} for a well-formed alkanethiolate/Au{111} SAM.[24,25] The deposition was monitored with a Au coated QCM electrode. The sticking coefficient is 1 for bare Au vs. SAMs of alkane thiols.

2.2.3 Atomic Force Microscopy

The atomic force microscopy (AFM) measurements were performed in a ultrahigh vacuum (UHV) chamber (base pressure 10^{-10} torr) outfitted with a RHK 350 scan head setup controlled by a RHK SPM 100 electronics system (RHK technologies, Troy, MI). The contact mode AFM images were taken with Silicon cantilevers (FMR type, spring constant ~2.8 N/m, tip radius ~10 nm; Molecular Imaging, Tempe, AZ). The CPAFM images were taken with Platinum-Iridium (90/10) coated silicon cantilevers (EFM type, spring constant ~3.0 N/m, tip radius ~20 nm, Molecular Imaging, Tempe, AZ). The scan head was calibrated in the z direction using Au single step edges (0.3nm). The x & y lateral directions were calibrated using lattice images of dodecane thiol monolayers on Au (111).[24,25] The samples were initially analyzed by contact mode with a silicon tip because the silicon tips are both sharper and more durable than the metal coated conducting tips. All lattice imaging was done with the silicon tips as we were unable to get good lattice resolution images with any of the metal coated tips. Following analysis of the uncoated monolayer, the samples were transferred under continuous vacuum to the

deposition chamber, which is isolated from the analysis chamber by a gate valve. After the deposition, the metal/SAM specimen was transferred directly *in vacuo* back to the analysis chamber for immediate imaging where the pressure was maintained below $5x10^{-10}$ torr.

2.3 Results

The structure of gold grown on a dodecane thiol SAM on Au was inspected by UHV AFM. Prior to the deposition of the gold contact mode images were taken to confirm the cleanliness and integrity of the monolayer. Figure 2.1a shows a typical **C12** SAM on Au(111), with large underlying (111) terraces and well-defined step edges. Figure 2.1b shows a AFM image of the SAM showing a hexagonal lattice with a nearest neighbor distance of 4.9±0.4 Å corresponding to a (√3X√3)R30˚ lattice structure.[24,25] Images taken of bare **C12** SAMs with a conducting tip show a uniform insulating film, Figure 2.1c.[26]

In the initial stages of the Au deposition, 1 to 5 equivalent monolayers deposited, the surface topography revealed by traditional AFM does not undergo detectable changes from that of a bare monolayer. This can be seen in Figure 2.2a where the structure of the surface is indistinguishable from that of a bare monolayer. Importantly, no rough features or amorphous regions are observed that might indicate Au cluster growth. Imaging with a silicon AFM tip reveals that the monolayer is still ordered after the deposition, see Figure 2.2c. This agrees with previous reports[16,17] that the Au atoms penetrate through the SAMs and diffuse across the Au/S interface to form a commensurate structure with the

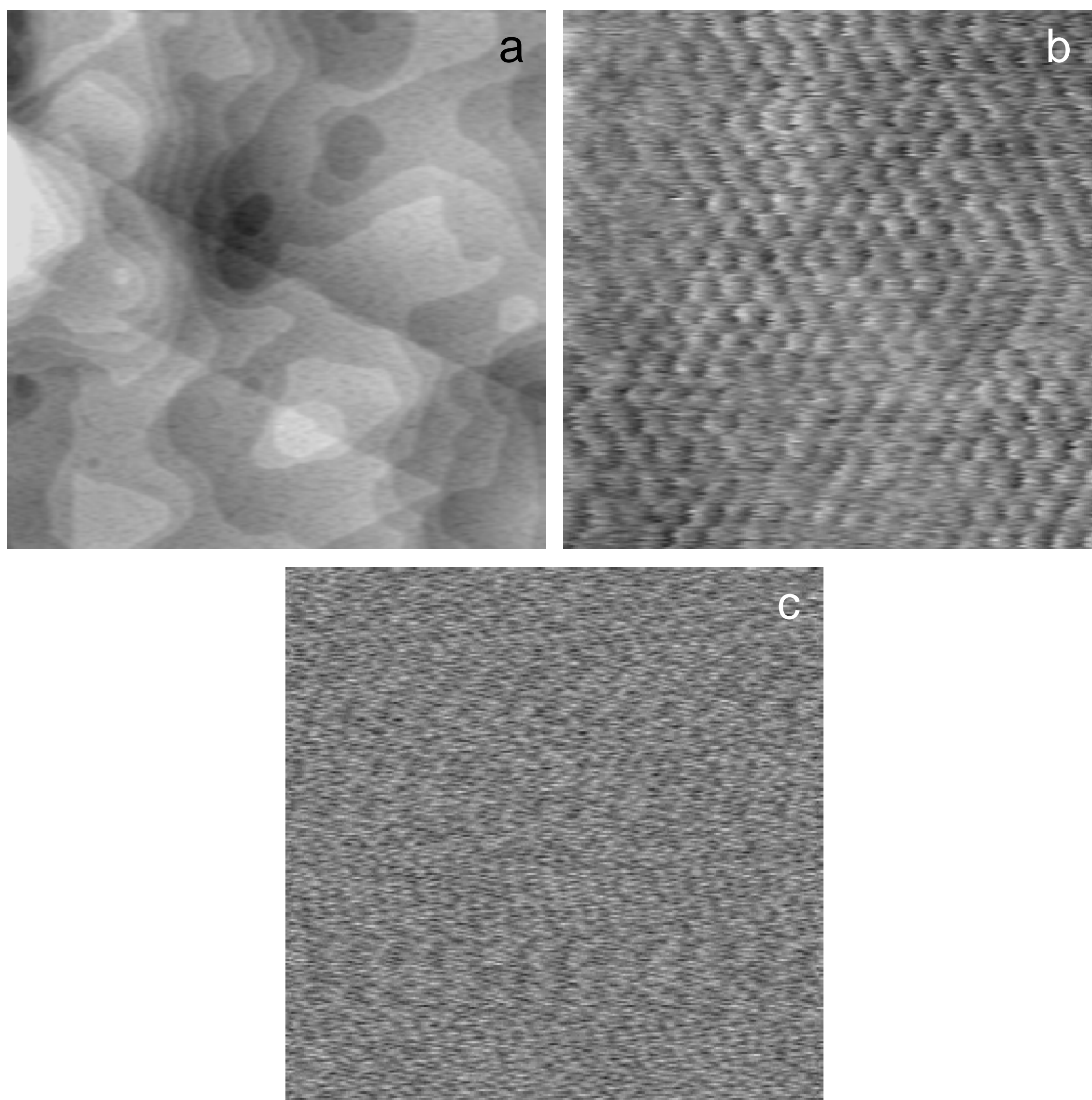

Figure 2.1. (**a**) AFM image of a bare **C12** SAM surface. 1 μm x 1 μm contact mode image showing the surface topography. The image reveals the underlying (111) Au terraces and step edges. (**b**) Unfiltered lateral force image on a smaller area (8 nm x 8 nm) of the bare dodecane thiol SAM reveals the hexagonally packed molecular lattice. (c) Current image of the bare SAM, the image taken with a -1V bias on the surface reveals an insulating film to the limit of our electrical amplifiers (10pA).

underlying Au, allowing an ordered SAM film to 'float' above the Au substrate. However, upon inspection of a current image, taken simultaneously with the topography, points of conduction in the film are observed, see Figure 2.2b. Since they are not present in the bare monolayer surfaces these conduction pathways must be due to the deposition of Au upon the surface. The conduction pathways are caused by nanofilaments of Au growing upwards from the surface of the Au (111) substrate, illustrated in Figure 2.3. Small filaments that are close to the thickness of the monolayer, or just short of it, would be very difficult to detect using contact mode AFM due to the large radius of curvature of the tip and the AFM contact interface.[27] However, by using the tip as a conducting probe we are able to detect the presence of these filaments since they form conduction pathways to the Au substrate. The amount of current through these conduction pathways was found to vary greatly from hundreds of pA up to a complete short, at -10nA.[28] This variation in conduction is attributed to different sizes of Au filaments formed on the surface of the Au(111). If the filament is longer than the monolayer is thick (~16 Å [29]), then filaments would penetrate the monolayer entirely and come into direct contact with the scanning conducting tip. These are seen in the current image as complete electrical shorts. If the filament is shorter than the monolayer then the monolayer would serve as an insulating layer. However, the tunneling barrier to the Au substrate would be reduced and conduction dependent upon the distance between the surface of the monolayer and the filament is observed.

As Au coverage increases to the 5-10 equivalent monolayers regime, Au filament growth through the monolayer becomes more apparent in both the topography and current modes of the CPAFM images. Figure 2.4 shows both the topography and the current

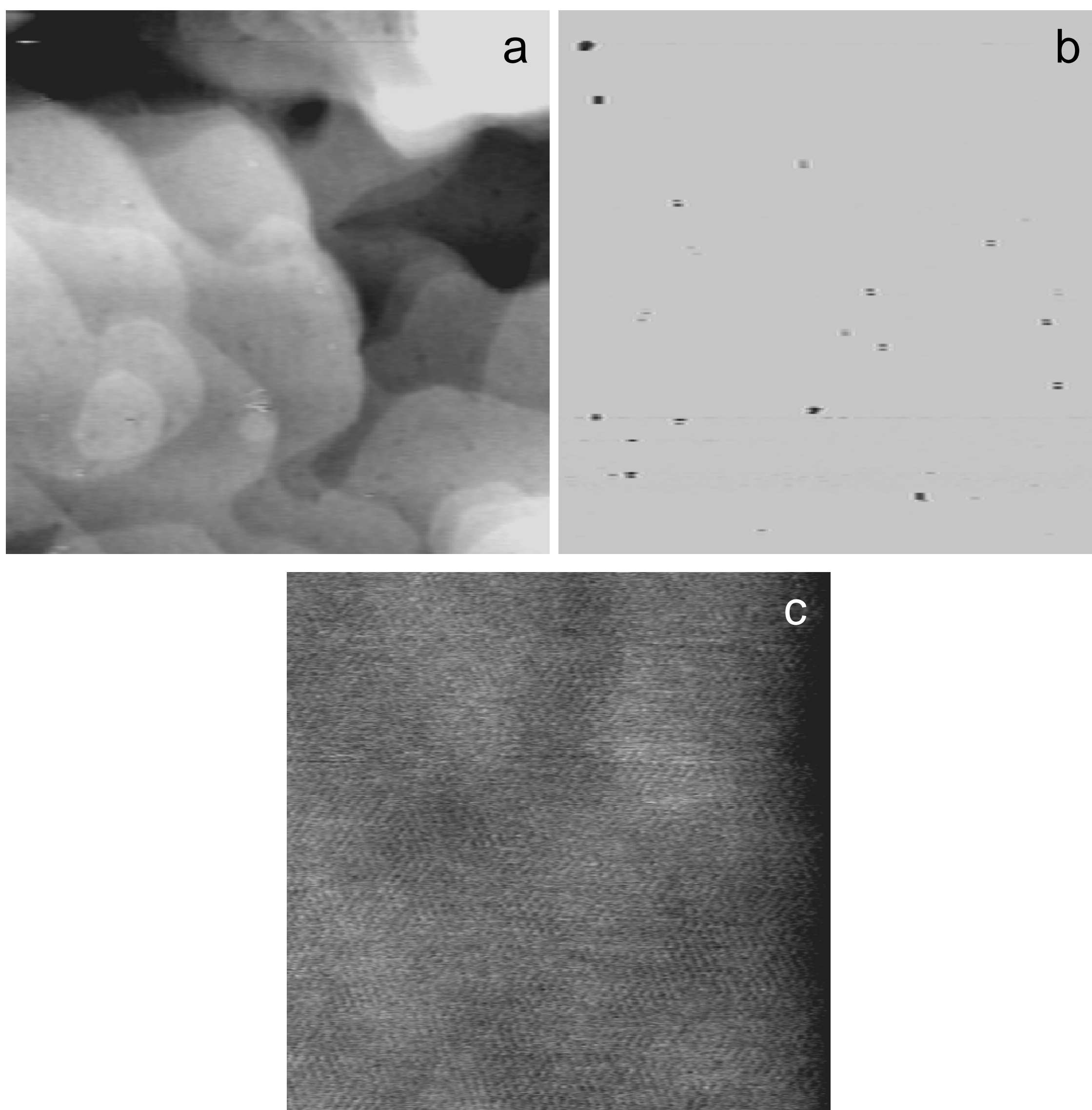

Figure 2.2. CPAFM image (1μm x 1μm) of a **C12** SAM with 5 eq ML of Au vapor deposited. (**a**) Topography shows the clear structure of the underlying Au (111) substrate, indicating uniform and commensurate growth of a gold film underneath the SAM. (**b**) Current image recorded simultaneously with the topography showing electrical shorts in the film, indicating the presence of Au filaments in the monolayer. (**c**) Typical unfiltered lateral force image (25.4nm x 25.4 nm) shows large ordered areas.

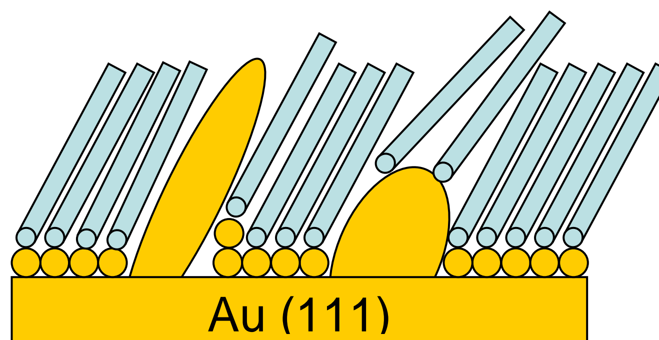

Figure 2.3. A schematic of different length Au filaments growing upwards from the Au substrate that would be seen as conduction pathways in the film. As the filaments start to form the tunneling barrier from the surface of the monolayer to the substrate is reduced allowing current to pass to the substrate more readily than before. If the filament is long enough, the AFM tip can come into direct contact with it causing a direct short to the Au substrate.

images taken on a **C12** SAM with 10 equivalent monolayers of Au deposited on it. The topography image reveals flat ordered regions where commensurate growth of Au on the substrate occurs and the formation of large filaments, ranging in size up to 6 nm in height. At the locations of the filaments the current image reveals electrical shorts in the film. The volume of the clusters does not account for all of the vaporized Au on the surface.[30] Therefore, some uniform diffusion through the monolayer must still occur. Importantly, the locations of the Au filaments are found on step edges of the Au and other defect locations on the Au (111) substrate. These defects in the substrate are also likely to cause

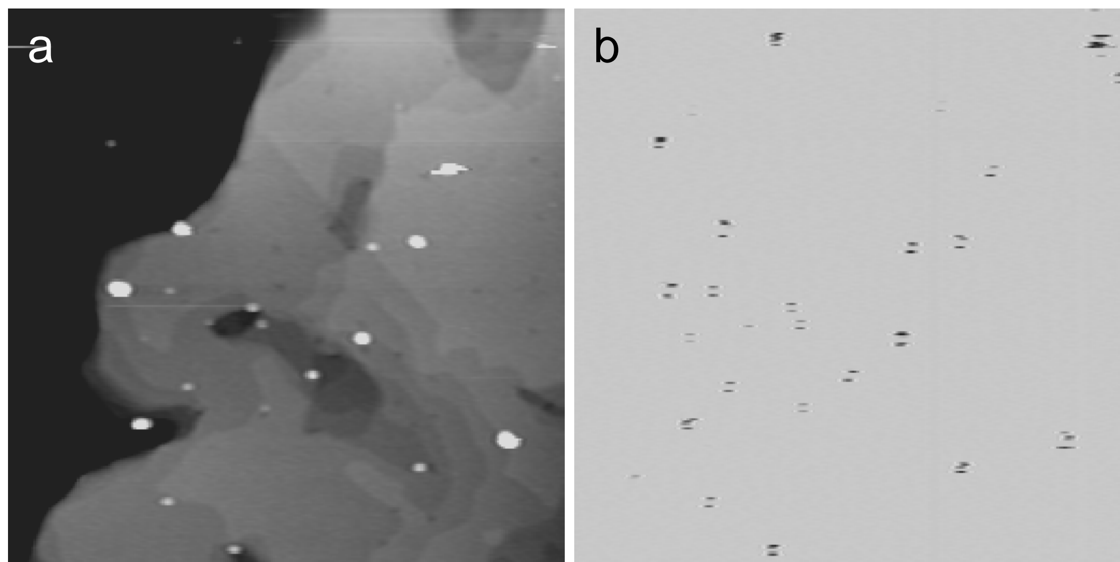

Figure 2.4. CPAFM image (1μm x 1μm) of a dodecane thiol SAM with 10 eq ML of Au vapor deposited. (**a**) Topography shows the clear structure of the underlying Au (111) substrate and the presence of large clusters of Au penetrating the monolayer. (b) Current image recorded simultaneously with the topography reveals electrical shorts in the film at all of the cluster locations.

defects in alkanethiol monolayers.[23] The presence of these filaments at likely monolayer defect locations implies that Au atoms can pass through defects in the monolayer at a fast enough rate that the commensurate diffusion of Au across the S-Au interface does not occur before the buildup of gold filaments through the monolayer.

Once filaments form on the surface, the local area around the cluster has a lower coverage of SAM molecules caused by local surface roughening. This lower coverage will cause more defects in the monolayer to form, thus making the area surrounding the

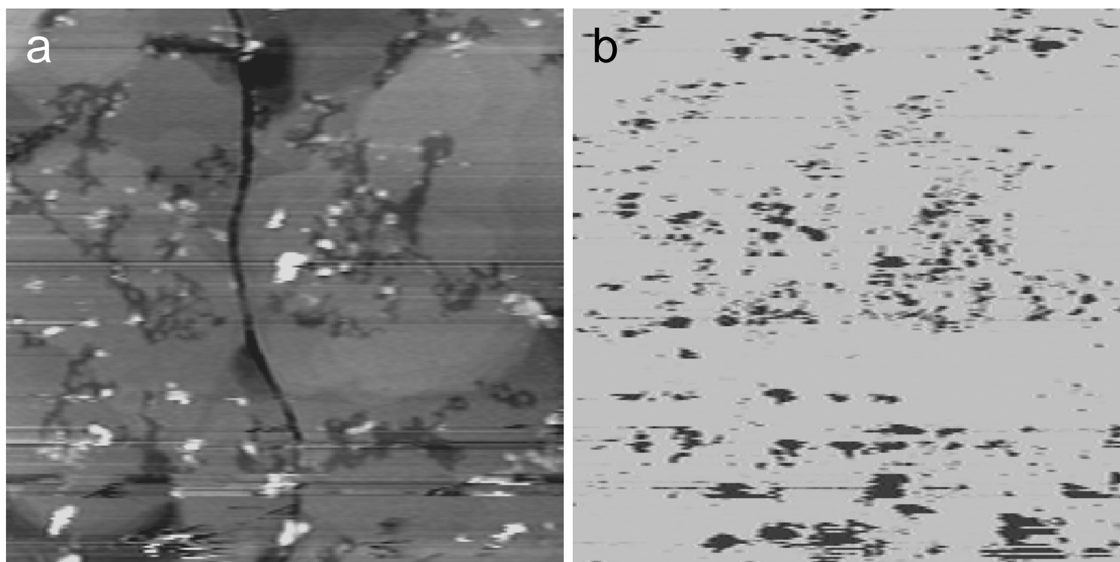

Figure 2.5. CPAFM image (1μm x 1μm) of a dodecane thiol SAM with 20 eq ML of Au vapor deposited. (**a**) Topography shows the structure of the underlying Au (111) substrate, and the presence of large clusters of Au penetrating the monolayer from the Au substrate surrounded by roughened areas around it. (b) Current image recorded simultaneously with the topography showing shorts in the film at the clusters and the surrounding rough areas of the surface.

original filament more prone to forming Au filaments. This is seen clearly in Figure 2.5 where large areas of defects and conduction can be seen in localized areas on the surface after 20 equivalent monolayers of Au are deposited. The surface is segregated into two distinct regions: flat insulating regions and rough areas with Au clusters with many conduction pathways not clearly detectable in the topography images. While it is likely that the diffusion rate through defect sites increases at this point, due to the larger number

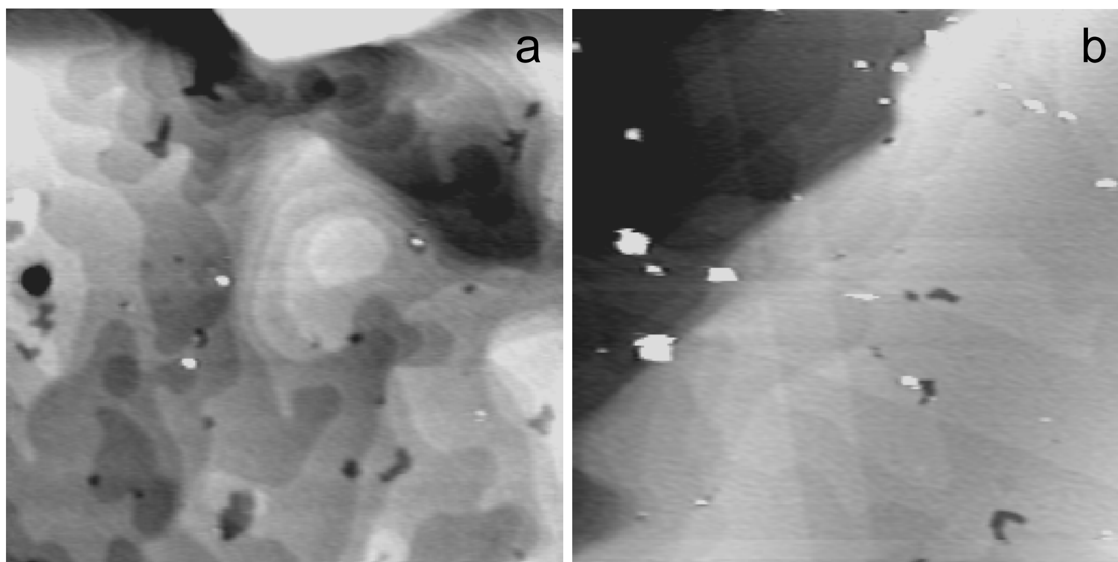

Figure 2.6. AFM images (1μm x 1μm) of a solution annealed dodecane thiol SAM with (a) 20 and (b) 30 eq ML of Au vapor deposited. The images reveal far fewer cluster formations relative to an unannealed monolayer (Figure 2.4).

of defects in the monolayer, it is impossible to tell from our experiments what percentage passes through ordered regions as opposed to defect sites in the monolayer.

Bumm and coworkers,[23] found that alkanethiol monolayers could be annealed in solution to form much larger alkanethiol grains and fewer monolayer defect sites in the monolayer. We utilized this technique as further proof of our proposed diffusion mechanisms. Figures 3.6a and 3.6b show AFM images of a solution annealed monolayer of dodecane thiol after 20 and 30 equivalent monolayers of Au have been deposited respectively. The images show a dramatically lower number of visible Au clusters on the surface compared to that of an unannealed monolayer, see Figure 2.4. The higher ordering of the monolayer has significantly limited the diffusion pathways of the Au to

be primarily through ordered regions. However, filaments do form on the surface since defects are still present in the monolayers.

2.4 Conclusion

The presence of both uniform growth and filaments implies two separate pathways through the monolayer. Our findings indicate that as the Au is vapor deposited on to the SAM substrate, the Au atoms strike the vacuum/monolayer interface and move around the surface until they find a way to pass through the monolayer. One pathway is the diffusion through the monolayer through temporary vacancies in ordered regions of the monolayer, created by thermal fluctuations at room temperature.[13,14] This diffusion is slow enough that the Au atoms move laterally across the Au/S interface forming a commensurate Au {111} surface. This Au diffusion pathway results in the monolayer 'floating' on the growing Au {111} surface. A second, and faster, diffusion pathway through the monolayer is through large defect sites in the monolayer. This pathway is too fast for Au atoms to uniformly distribute across the Au/S interface and leads to the formation of Au filaments on the Au {111} surface. These filaments form electrical shorts in the monolayer. These diffusion pathways are both inappropriate for molecular electronic structures, as the first has no top metal contact and the second forms an electrical short in the film. Formation of an effective top metal contact will require the formation of a uniform top metal contact with absolutely no shorts in it. Futher experiments need to be done to determine if it is possible to form an effective top contact on alkanethiol monolayers by reducing the formation of temporary vacancies on highly ordered films. Proposed methods to reduce temporary vacancies include, reducing

temperature of the samples and increasing the interaction between neighboring monolayer molecules with forces other than Van der Waals, such as hydrogen bonding.

References

[1] Tour, J. M.; Kozaki, M.; Seminario, J. M. *Journal of the American Chemical Society* **1998,** *120*(33), 8486-8493.

[2] Ratner, M. A.; Davis, B.; Kemp, M.; Mujica, V.; Roitberg, A.; Yaliraki, S. *Molecular Electronics: Science and Technology* **1998,** *852* 22-37.

[3] Chen, J.; Reed, M. A.; Rawlett, A. M.; Tour, J. M. *Science* **1999,** *286*(5444), 1550-1552.

[4] Wang, W. Y.; Lee, T.; Reed, M. A. *Physical Review B* **2003,** *68*(3).

[5] Wang, W. Y.; Lee, T.; Reed, M. A. *Journal of Physical Chemistry B* **2004,** *108*(48), 18398-18407.

[6] Wang, W. Y.; Lee, T.; Kretzschmar, I.; Reed, M. A. *Nano Letters* **2004,** *4*(4), 643-646.

[7] Collier, C. P.; Mattersteig, G.; Wong, E. W.; Luo, Y.; Beverly, K.; Sampaio, J.; Raymo, F. M.; Stoddart, J. F.; Heath, J. R. *Science* **2000,** *289*(5482), 1172-1175.

[8] Zhou, C.; Deshpande, M. R.; Reed, M. A.; Jones, L.; Tour, J. M. *Applied Physics Letters* **1997,** *71*(5), 611-613.

[9] Metzger, R. M.; Baldwin, J. W.; Shumate, W. J.; Peterson, I. R.; Mani, P.; Mankey, G. J.; Morris, T.; Szulczewski, G.; Bosi, S.; Prato, M.; Comito, A.; Rubin, Y. *Journal of Physical Chemistry B* **2003,** *107*(4), 1021-1027.

[10] Dhirani, A.; Lin, P. H.; GuyotSionnest, P.; Zehner, R. W.; Sita, L. R. *Journal of Chemical Physics* **1997,** *106*(12), 5249-5253.

[11] Liang, W. J.; Shores, M. P.; Bockrath, M.; Long, J. R.; Park, H. *Nature* **2002,** *417*(6890), 725-729.

[12] Salomon, A.; Cahen, D.; Lindsay, S.; Tomfohr, J.; Engelkes, V. B.; Frisbie, C. D. *Advanced Materials* **2003,** *15*(22), 1881-1890.

[13] Bhatia, R.; Garrison, B. J. *Langmuir* **1997,** *13*(4), 765-769.

[14] Bhatia, R.; Garrison, B. J. *Langmuir* **1997,** *13*(15), 4038-4043.

[15] Hooper, A.; Fisher, G. L.; Konstadinidis, K.; Jung, D.; Nguyen, H.; Opila, R.; Collins, R. W.; Winograd, N.; Allara, D. L. *Journal of the American Chemical Society* **1999,** *121*(35), 8052-8064.

[16] Ohgi, T.; Sheng, H. Y.; Nejoh, H. *Applied Surface Science* **1998,** *132* 919-924.

[17] Ohgi, T.; Sheng, H. Y.; Dong, Z. C.; Nejoh, H. *Surface Science* **1999,** *442*(2), 277-282.

[18] Allara, D. L.; Nuzzo, R. G. *Langmuir* **1985**, *1*, 52-66.

[19] Nuzzo, R. G.; Dubois, L. H.; Allara, D. L. *J. Am. Chem. Soc.* **1990**, *112*, 558-569.

[20] Laibinis, P. E.; Whitesides, G. M.; Allara, D. L.; Tao, Y. T.; Parikh, A. N.; Nuzzo, R. G. *J. Am. Chem. Soc.* **1991**, *113*, 7152-7167.

[21] MacPhail, R. A.; Strauss, H. L.; Snyder, R. G.; Elliger, C. A. *J. Phys. Chem.* **1984**, *88*, 334-341.

[22] Laibinis, P. E.; Nuzzo, R. G.; Whitesides, G. M. *J. Phys. Chem.* **1992**, *96*, 5097-5105.

[23] Bumm, L. A.; Arnold, J. J.; Charles, L. F.; Dunbar, T. D.; Allara, D. L.; Weiss, P. S.

Journal of the American Chemical Society **1999,** *121*(35), 8017-8021.

[24] Poirier, G. E.; Tarlov, M. J. *Langmuir* **1994,** *10*(9), 2853-2856.

[25] Delamarche, E.; Michel, B.; Gerber, C.; Anselmetti, D.; Guntherodt, H. J.; Wolf, H.; Ringsdorf, H. *Langmuir* **1994,** *10*(9), 2869-2871

[26] Images taken on C12 monolayers with conducting PtIr tips with a 1V surface bias show no measurable current at all. The noise floor of the current amplifiers we used is ~10pA.

[27] Carpick, R. W.; Salmeron, M. *Chemical Reviews* **1997,** *97*(4), 1163-1194.

[28] -10nA was the high current limit set for the current amplifier for these experiments. The voltage was limited to -10mV since higher voltages were found to create currents high enough to damage the tip, this high current can lead to complete demetallization of the contact area of the tip. This is unfortunate since higher voltages could be used to probe deeper into the monolayers enabling better imaging of filament growth beneath the alkanethiol surface.

[29] Shi, J.; Hong, B.; Parikh, A. N.; Collins, R. W.; Allara, D. L. *Chemical Physics Letters* **1995,** *246*(1-2), 90-94.

[30] The bulk density of Au was used in the volume calculations 19.3 g cm^{-3}.

Chapter 3

Evolution of the Interface and Metal Film Morphology in the Vapor Deposition of Ti on Hexadecanethiolate Monolayers on Au {111}

3.1 Introduction

The vacuum deposition of metal layers on organic thin films is a widely used process used for many applications ranging from electronic devices to barrier coatings. Predictions of the outcome of any particular deposition are typically very difficult because of the lack of fundamental information on the complex, intertwined chemical and physical processes that can be involved in the interface formation and metal overlayer growth. As a means of building fundamental rules underlying these complex phenomena, recent efforts have focused on using the chemically and physically well-defined structures of self-assembled monolayers (SAMs) as the organic substrates.[1-8] These structures not only provide model systems but have become highly relevant because of their recent applications in molecular electronic devices where vapor deposited metal contacts are used in a base electrode-molecule-metal structure[9-29] for which the exact nature of the contact interface and metal morphology can profoundly affect device performance.

When metal atom vapors impinge on organic substrates a wide range of behaviors are possible, many often undesired, including severe chemical degradation, clustering of the metal into heterogeneous overlayers with discontinuous interfaces, penetration deep into the organic matrix and even scattering from the surface with no condensation. For a number of applications, particularly molecule-based electronics using top metal contact devices; it is desirable to achieve reproducibly uniform deposition across the surface with subsequent growth of a dense, uniform metal overlayer. One potential path for achieving this structure might seem to be the deposition of metal atoms which exhibit chemical reactivity with the ambient surface of the organic substrate, based on the simple notion

that uniform reaction across the surface should lead to a uniform nucleation and growth. Recent reports, however, demonstrate cases where this picture does not completely hold. For example, in the case of Al vapor deposition on a methyl ester-terminated hexadecanthiolate/Au{111} SAM, it was observed that while the initially deposited Al atoms react quantitatively with the ester groups in a 1:1 stoichiometry, subsequent deposition produces several layers of a dielectric form of the Al, followed by an ~3 nm highly porous metallic phase and a final dense metal overlayer.[3] In contrast, for Al deposited on H_3C- or H_3CO-terminated hexadecanethiolate/Au{111} SAMs there are no chemical reactions and the Al atoms partition to different extents between penetration to the Au/S interface to form an adlayer and growth of an overlayer at the SAM surface.[3,5] These data show that Al, typically considered a chemically reactive metal in terms of its thermochemical ability to form highly stable oxides and carbides, appears, in fact, to be dominantly controlled by subtle kinetic factors in its interactions with SAM surfaces. In view of this, it is of significant interest to explore the behavior of other common, aggressively reactive metals to look for complexities in their deposition on organic materials. The specific example of Ti would appear to be a good starting point because of the well known aggressive chemical character of Ti and its common use in microelectronics processing,[30,31] especially as a top contact in molecule-based electronics.[9,11,12,16,17,20,21,23-28]

Pointing to the aggressive nature of Ti, the vapor deposited metal reacts indiscriminately with triazine, polyimide, polystyrene, polyethylene, and epoxy films to form Ti-O, Ti-C and Ti-N bonds[30-34] and with fluoropolymers to form Ti-C, Ti-O and Ti-F bonds.[35] In previous work[36] we showed from XPS data for ambient temperature

substrates that Ti reacts with the terminal groups of -CO_2H, -CO_2CH_3, -CH_3, -OH and -CN terminated alkanethiolate SAMs and concluded further that Ti readily reacts with the -CH_2- moieties of alkyl chains, which should be the least reactive groups of typical organic molecules. In a recent report, de Boer and co-workers, as a control to their larger study on vapor-deposited Au, Al, and Ti on SAMs of conjugated mono- and dithiols, also examined the interaction of Ti with the - CH_3 terminated hexadecanethiolate/Au{111} SAM.[24] Using infrared reflection spectroscopy (IRS) evidence they found Ti to be highly reactive and destructive. In spite of this pattern of aggressive reactivity from both XPS and IRS studies, however, the preliminary data from our earlier XPS study[36] also suggests that in the initial stages of deposition on the -CH_3 terminated hexadecanethiolate/Au{111} SAM a fraction of the incoming Ti atoms striking the surface scatter back into the vacuum with no reaction while the adsorbed remainder do not nucleate uniformly across the surface, but rather form isolated clusters.

Overall, these limited data suggest the -CH_3 terminated SAM shows a range of behaviors in Ti vapor deposition which are controlled by kinetic processes as well as thermochemical driving forces. Given the recent interest in using Ti metal as a top contact for device structures with hydrocarbon-like top layers[11,20,21,24-28] and our own work in optimizing the top contacts in molecular electronic devices (e.g., see reference 7), there was significant motivation to explore in greater detail the processes involved in Ti deposition on alkyl chain monolayers and relate this to the desirable characteristics for high quality contacts. The results of our study show that for deposition on a sample at room temperature with controlled Ti fluxes, Ti does indeed scatter off the CH_3 SAM surface, with a smooth decrease in the scattered fraction with increasing Ti doses, followed by gradual formation of a heterogeneous interface. The overall structure

consists of clusters of Ti atoms with metallic Ti outer regions and deep carbide interphases, which eventually at total average coverages exceeding 50 Ti atoms per SAM molecule merge into a continuous overlayer. These results underscore the need to understand how the interplay between kinetic and thermochemical pathways can affect the physical and chemical characteristics of deposited top metal layers on organic films for applications such as molecular devices.

3.2 Experimental

3.2.1 Materials and General Procedures

Details of the synthesis of $D_3C(CD_2)_7(CH_2)_8S$-/Au SAM can be found in the Appendix B. The preparation and characterization of the $H_3C(CH_2)_{15}S$-/Au and $D_3C(CD_2)_7(CH_2)_8S$-/Au SAMs have been described in detail previously[37-41] and is summarized briefly here. Sequential thermal depositions of Cr (~10 nm) and Au (~200 nm) were made onto clean Si(001) native oxide covered wafers. Self-assembly of well-organized monolayers was achieved by immersing the Au substrates into millimolar solutions of the relevant alkanethiol molecules in absolute ethanol for ~2 days at ambient temperature. The monolayer films were characterized with single wavelength ellipsometry, infrared spectroscopy and contact angle measurements to ensure that they were densely packed, clean surfaces. In addition, all SAMs were characterized by the initial TOF-SIMS, IRS, and XPS measurements prior to metal deposition.

Several sources were used for Ti (R.D. Mathis, Alfa Aesar) but in all cases the purities were ≥ 99.99 %. The depositions were conducted using resistively heated tungsten baskets or Ti coated tungsten wires with fluxes controlled to ~0.15 atoms·nm^{-2}·

s^{-1} at the sample for all analysis methods. The throw distances were all >35 cm and the sample temperatures remained near ~25 °C under the deposition conditions. In all cases the mass of metal atoms delivered to the SAM surfaces was measured by placing quartz crystal microbalance (QCM) crystals with gold electrodes in the path of the vapor flux. Geometric factor corrections (tooling factors) for the placement of the QCM crystal relative to the sample and absolute fluxes were calibrated using AFM measured film thicknesses at the sample and QCM crystal locations. Readout/controller units were obtained from Maxtek, Inc. (TM-400; maximum error ± 8 %; ToF-SIMS setup) and Sigma Instruments (SQM-160, maximum error ± 7 %; IRS and XPS setup).

3.2.2 X-Ray Photoelectron Spectroscopy

The XPS analyses were performed using a Kratos Analytical Axis Ultra equipped with a monochromatic Al K_{α} source operating at an X-ray power of 280 watts. Spectra were collected at a 90° photoelectron take off angle with respect to the sample plane with a pass energy of 20 eV and an energy step of 0.15 eV. The resulting FWHM of the Au $4f_{7/2}$ line was 0.71 eV. All spectra were referenced to the Au $4f_{7/2}$ at 84.0 eV. Following analysis of the uncoated monolayer, the samples were transferred under continuous vacuum to the deposition chamber, which was isolated from the analysis chamber by a gate valve. During the depositions the pressure remained <$1x10^{-8}$ Torr. After deposition, the metal/SAM specimen was transferred directly in vacuo back to the analysis chamber where the pressure was maintained below $5x10^{-9}$ Torr.

3.2.3 Infrared Spectroscopy

Analyses were performed on a Fourier transform instrument (Mattson Research Series 1000) fitted with custom in-house optics configured externally to the instrument

and designed for grazing incidence reflection of samples under vacuum.[3-5, 8] A liquid nitrogen cooled MCT detector was used with an effective low frequency cutoff of ~750 cm^{-1}. The infrared beam passed through the analysis chamber through a pair of differentially-pumped KBr windows. After analysis of the bare monolayer a shield was moved to unblock the path between the sample and the metal source. The pressure remained $<3x10^{-7}$ Torr during the deposition. The final spectra were determined as -log(R/R_o) where R is the sample spectrum and R_o is the spectrum of a bare gold wafer or a $C_{16}D_{33}$-S-/Au{111} SAM, with a given reference chosen on the basis to maximize information in the specific spectral region of interest for a given sample.

3.2.4 Time-of-Flight Secondary Ion Mass Spectrometry

The TOF-SIMS analyses were performed on a custom designed instrument as described previously.[42] Briefly, the instrument consists of a loadlock, a preparation chamber, a metal deposition chamber and the primary analysis chamber, each separated by a gate valve. The primary Ga^+ ions were accelerated to 15 keV and contained in a 100 nm diameter probe beam which was rastered over a (106x106) μm^2 area during data acquisition. All spectra were acquired using a total ion dose of less than 10^{11} ions·cm^{-2}. Relative peak intensities are reproducible to within ± 8 % from sample to sample and ± 8 % from scan to scan. During deposition the pressure remained $<5x10^{-8}$ Torr. After deposition, the preparation chamber pressure was allowed to recover to the base value of $1.5x10^{-9}$ Torr before sample transfer to the analysis chamber.

3.2.5 Atomic Force Microscopy

The AFM measurements were performed in a UHV chamber (base pressure 10^{-10} Torr) outfitted with a RHK 350 scan head setup which was controlled by a RHK SPM

100 electronics system (RHK technologies, Troy, MI). The images were taken with silicon cantilevers in contact mode (FFM type, spring constant ~2.8 N/m, tip radius ~10 nm; Molecular Imaging, Tempe, AZ). The SAM was formed on Au(111) substrates on mica (Molecular Imaging, Tempe, AZ) which were flame annealed immediately prior to monolayer formation. Following in-vacuo AFM analysis of the freshly made SAM, the samples were transferred under continuous vacuum to the deposition chamber, which was isolated from the analysis chamber by a gate valve. During the deposition the pressure remained $<5\times10^{-8}$ Torr. The mass of the deposited Ti was obtained using a SAM coated electrode adjacent to the sample. After deposition, the metal/SAM specimen was transferred directly in vacuo back to the analysis chamber for immediate imaging where the pressure was maintained below 5×10^{-10} Torr.

3.2.6 Definition and Measurement of Deposited Metal Coverage

The amount of metal delivered per unit area to the samples was determined from the QCM measurements as mass per unit area (ρ_A). For ease in data analysis and interpretation, an equivalent coverage of metal atoms per SAM molecule (θ_{Ti}) was calculated using the ρ_A values and the molecular density of 4.6 molecules·nm^{-2} for a well-formed alkanethiolate/Au{111} SAM. It follows that our deposition flux of ~0.15 atoms·nm^{-2}·s^{-1} is equivalent to ~0.033 Ti atoms per SAM molecule per second.

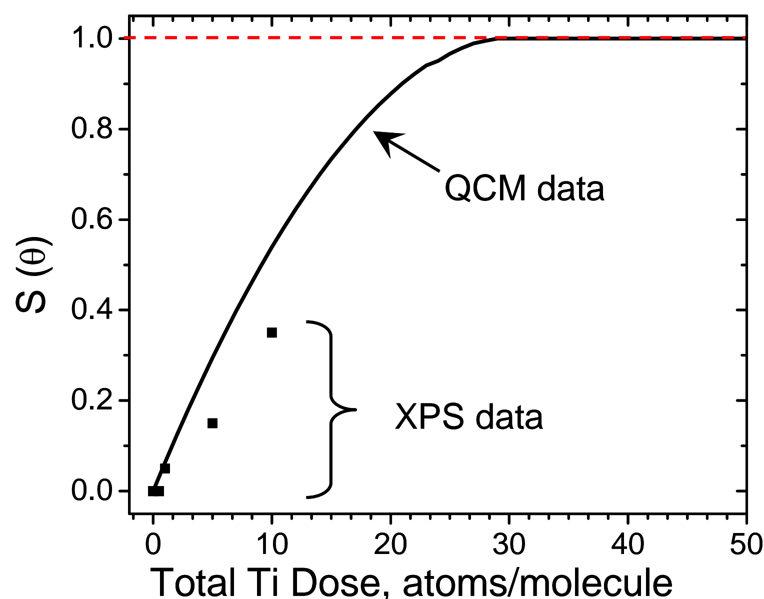

Figure 3.1: Sticking (condensation) coefficient S(θ) of Ti on the SAM surface vs total Ti dose delivered (atoms per SAM molecule) to the SAM surface. (——) determined from a dual QCM experiment, (•) estimated from XPS Ti 2p peak areas, (----) line marking S(θ)=1.0. For details see text.

In the early stages of Ti deposition on the SAM it was observed by XPS that only a fraction of the deposited metal vapor impinging on the surface condensed. In order to determine accurate condensation efficiencies measurements were made of the sticking (or condensation) coefficients, defined as $S(\theta) \equiv \theta/\theta_o$, where θ_o is the total number (dose) of metal vapor atoms impinging per SAM molecule, as determined directly from the QCM ρ_A values. The experiments were conducted using a side by side, dual QCM setup with a SAM covered Au QCM electrode and a reference bare Au electrode.[43] The data (Figure

3.1) show an initial S(θ) value of ~0.1 with a subsequent smooth, asymptotic approach to S(θ) = 1.0 at high doses. A cross check using coverages estimated from the XPS Ti 2p core level peak areas in the low coverage region[44] is shown in Figure 3.1.

3.3 Results

3.3.1 XPS – Formation of Carbide Products

The constant binding energy for the Au $4f_{7/2}$ line (Figure 3.2, left) indicates negligible charging or alloying at the gold interface[36]. In the C 1s region (Figure 3.2, center) starting at $1.2 < \theta < 3.3$, a feature appears at 282.1 eV that is straightforwardly assigned to a carbide species.[30,36,45,46] Further deposition shows attenuation and broadening of the main -(CH_2)- C 1s feature and continued carbide growth.[36] The Ti 2p region (Figure 3.2, right) shows Ti appearing at low coverages (θ=1.1). This is most easily seen for the stronger $2p_{3/2}$ feature of the Ti 2p doublet where a peak appears at 454.7 eV. This initial feature is assigned to Ti-C.[30,36,45,46] The positions and extent of carbide formation in the C 1s and Ti 2p regions agree well with our previously published results.[36] Looking at the Ti 2p3/2 feature in detail, as the deposition increases to θ = 14.8 the lineshape becomes broader and asymmetric with intensity appearing on the low binding energy side and a markedly broad shoulder on the high energy side of the main carbide peak. The low binding energy intensity we attribute to metallic Ti[30,36,45-47] and the high binding energy shoulder is due to a convolution of oxide species formed from background gases.[30,45-47]

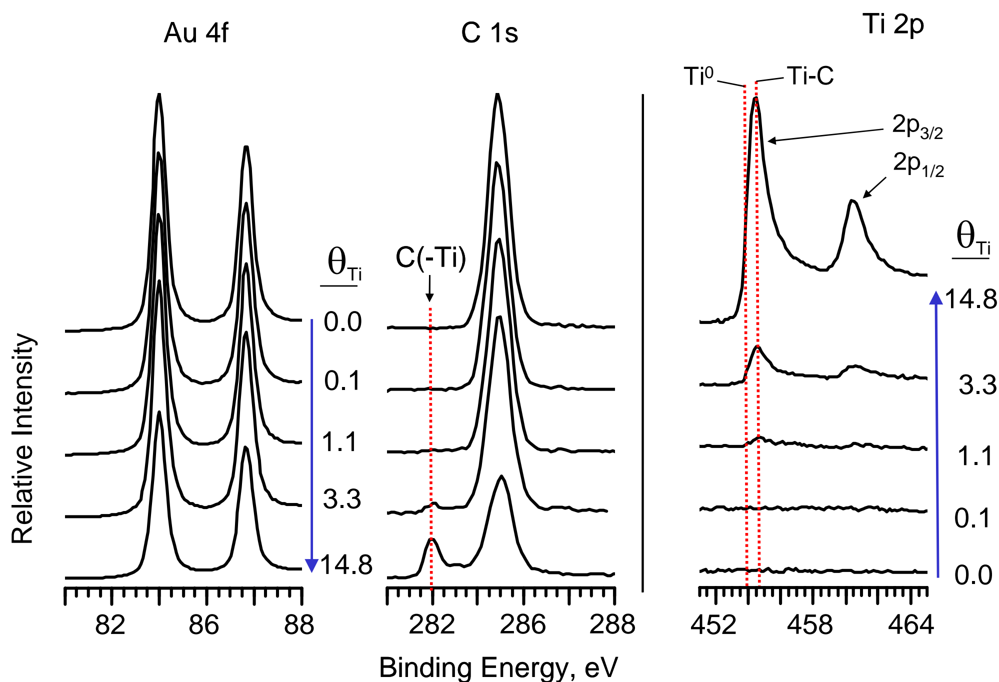

Figure 3.2: Au 4f, C 1s and Ti 2p core level XPS spectra for different coverages of Ti on the CH_3 SAM. XPS Au 4f (left), C 1s (center) and Ti 2p (right) core level spectra as a function of incrementally increasing Ti coverage on the SAM surface, as determined from the total amount of metal delivered to the surface, corrected for the independently measured sticking coefficient. The intensity scales are in arbitrary units and are different for each core level. The dashed lines in the Ti $2p_{3/2}$ peak at 454.7 and 456.4 eV mark the positions for the metallic and carbide species. For details see text.

Further analysis of the Ti 2p spectra at these higher coverages was not done because of the interfering species formed by reaction of Ti with background gases.[48]

3.3.2 IRS – Ti Deposition on A $CD_3(CD_2)_7(CH_2)_8S$-/Au SAM – A "Top Down" Localized Chemical Degradation

The experiments were carried out using SAMs prepared from $CD_3(CD_2)_7(CH_2)_8SH$ in order to allow the possibility of distinguishing between a "layer by layer" and a cratering or pitting mechanism in the carbide formation (see XPS section). Detailed characterization of the IR modes of C-H[37-41] and C-D[40,41] have been presented in detail elsewhere. The relevant stretching modes for the C-H (2800-3000 cm^{-1}) and C-D (2000-2300 cm^{-1}) are summarized for convenience: 2851 and 2918 cm^{-1}, -CH_2- symmetric C-H stretch (d^+) and -CH_2- antisymmetric C-H stretch (d^-) modes, respectively; 2091 and 2192 cm^{-1}, -CD_2- symmetric C-D stretch (d^+) and -CD_2- antisymmetric C-D stretch (d^-) modes, respectively; and 2074 and 2221 cm^{-1}, -CD_3- symmetric C-D stretch (r^+) and -CD_3- antisymmetric C-D stretch (r_a^-) modes, respectively.

The overall data are shown in Figure 3.3, where the trends in peak intensities clearly show the -CD_2- and -CD_3 modes rapidly losing intensity with increasing θ compared to the slow decay of the CH_2 modes. The attenuation of IR modes can be caused by chemical reactions, reorientation of the monolayer dipoles with respect to the surface,[49] or by screening of the dipoles due to metal atoms, clusters, or overlayers.[49,50] Since the spectral intensities from the C-D and C-H segments decay at different rates, reorientation of the molecules can be eliminated and the low overlayer coverages of the

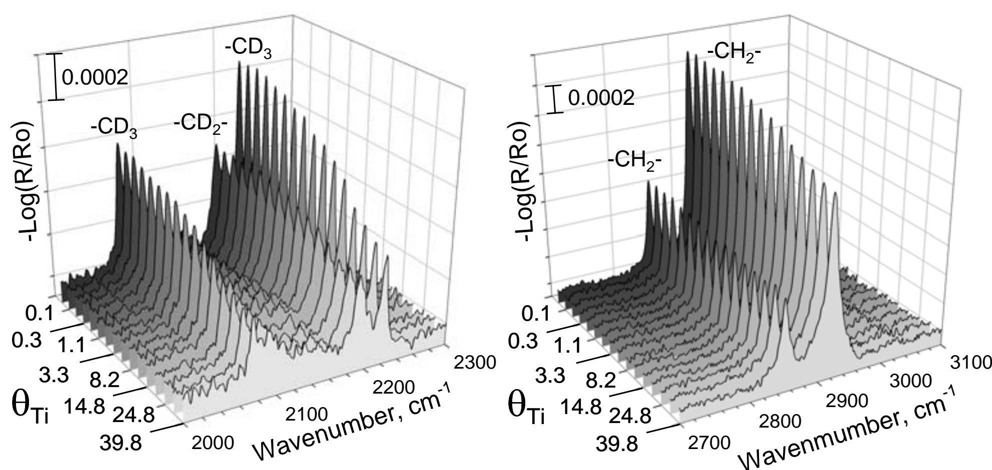

Figure 3.3: IRS C−H (right) and C−D (left) stretching mode spectra for a $CD_3(CD_2)_7$-$(CH_2)_8$-S-/Au SAM as a function of the incrementally increasing Ti coverage (θ_{Ti}) as determined from the total amount of metal delivered to the surface corrected for the independently measured sticking coefficient. Only selected spectra are assigned θ_{Ti} labels for clarity. For details see text.

metal are far too small for any significant electromagnetic field screening losses. Given the XPS evidence for carbide formation it is clear that the major cause of the peak losses are due to chemical degradation, with possible minor contributions from more subtle effects such as lineshape broadening. Since the -C_8D_{17} segment, located at the outer SAM surface, is associated with the fastest intensity decay one can readily conclude that significant chemical attack occurs at this segment. The particularly rapid decrease associated with the CD_3 group suggests this is the primary point of attack.

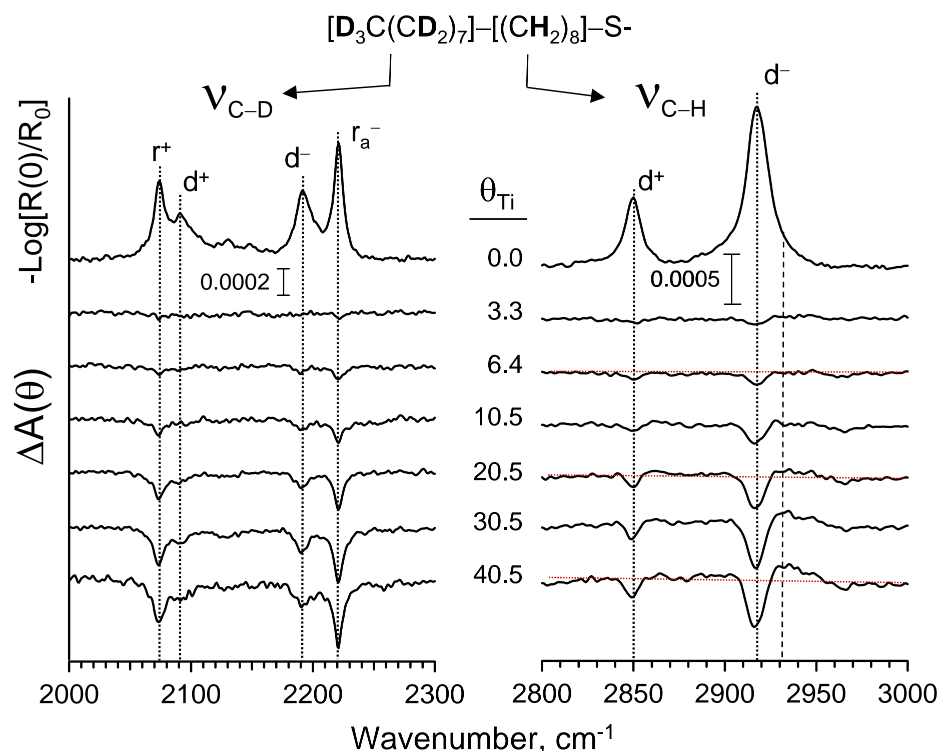

Figure 3.4: IRS C–H and C–D stretching mode spectra as a function of the incrementally increasing Ti coverage (θ_{Ti}) on a $CD_3(CD_2)_7$-$(CH_2)_8$-S-/Au SAM surface as determined from the total amount of metal delivered to the surface corrected for the independently measured sticking coefficient. The $\theta_{Ti} = 0$ spectrum is shown in terms of the actual intensities, -log[R(0)/Ro], while for $\theta_{Ti} > 0$ difference spectra, defined as $\Delta A(\theta) \equiv -\log[R(\theta_{Ti})/ R(\theta_o)]$, are shown. Thus, increasing negative peaks signify a loss of the original peak intensity from the bare SAM. The d and r symbols represent methylene and methyl group stretching features, respectively. For details see text.

In order to better reveal the changing character of the spectra, the data are plotted in Figure 3.4 in terms of absorbance difference spectra, $\Delta A(\theta)$, calculated as $-\log[R(\theta_{Ti})/R(\theta_o)]$ where θ_{Ti} represents the Ti-covered SAM and θ_o represents the bare SAM, respectively. Note that negative $\Delta A(\theta)$ features indicate an intensity loss relative to the original SAM spectrum for a given Ti coverage.

In the C-D stretching region (Figure 3.4, left side plots), representing the behavior of the top $-(CD_2)_7CD_3$ portion of the SAM , the small negative CD_3 mode peaks (2074 and 2221 cm^{-1}) barely appearing at $\theta_{Ti} = 3.3$ show that deposited Ti immediately interacts with the CD_3 group. At increasing Ti coverage negative CD_2 peaks appear and continued deposition shows attenuation to both the original CD_2 and CD_3 mode intensities, with preferential attenuation to CD_3. By $\theta = 40.5$ the $CD_2(d^-)$ and $CD_3(r_a^-)$ intensities are attenuated to ~35-40 and 50-60%, respectively. Since the exact stoichiometries of the reactions are uncertain it is difficult to extract quantitative relative reactivities from these data. Given the 14/3 ratio of CD_2 to CD_3 bonds in $-(CD_2)_7CD_3$ and a faster attenuation of the CD_3 modes, it is clear though that the Ti atoms favor reactions with the top CD_3 group, which in turn supports a top down degradation of the alkyl chain.

In the C-H stretching mode region (Figure 3.3, right side plots), both mode intensities decrease at the same rate, as expected, with a final d^- mode intensity attenuation of ~30% at $\theta = 40.5$. Note that this compares in magnitude roughly to the CD_2 d^- mode attenuation of ~35-40%. Consistent with this parallel behavior, the attenuation for the d^- mode intensity at $\theta = 20.5$ is ~0.2 for both the CD_2 and CH_2 modes. This comparison implies some chemical attack of Ti atoms is occurring at the bottom $-(CH_2)_8-$ chain units, as well as at the top of the SAM. Notice also, in contrast to the lack

of positive $\Delta A(\theta)$ features in the C-D spectra, the C-H spectra show the growth of weak, but clearly observable, positive features at ~2925-2935 cm^{-1}. These typically would correspond to the growth of conformational disorder in alkyl chains and suggests that there are a fraction of the alkyl chains in the SAM which are not destroyed, but rather disordered with increasing θ_{Ti}. On this basis we assign some of the C-H mode intensity loss to simple conformational disordering with the remainder to chemical degradation. Overall, the IR data point to a primary attack of Ti at the top of the chains with subsequent attack progressing into deeper regions of the SAM.

3.3.3 AFM – Ti Clustering and Heterogeneous Overlayer Morphology

Prior to metal deposition contact mode images were taken to confirm the cleanliness and integrity of the monolayer. The contact mode image of a typical freshly made SAM shows large underlying (111) terraces and well-defined step edges (Figure 3.5A), while the lateral force image (Figure 3.5B), obtained simultaneously, shows the same features but in less detail. At higher magnification (Figure 3.5C) in the contact mode the hexagonal lattice is observed with a nearest neighbor distance of 4.9±0.3 Å, corresponding to the standard $(\sqrt{3}x\sqrt{3})$,R30˚ lattice structure.[51,52]

In the initial stages of deposition the Ti appears on the surface as clusters which are easily moved by the tip during scanning. This is seen in Figure 3.6 for $\theta = 1$ where an initial scan of the surface, either in contact (**A**) or lateral force (**B**) modes, shows that when the tip comes in contact with a metal cluster the tip is deflected in both the normal

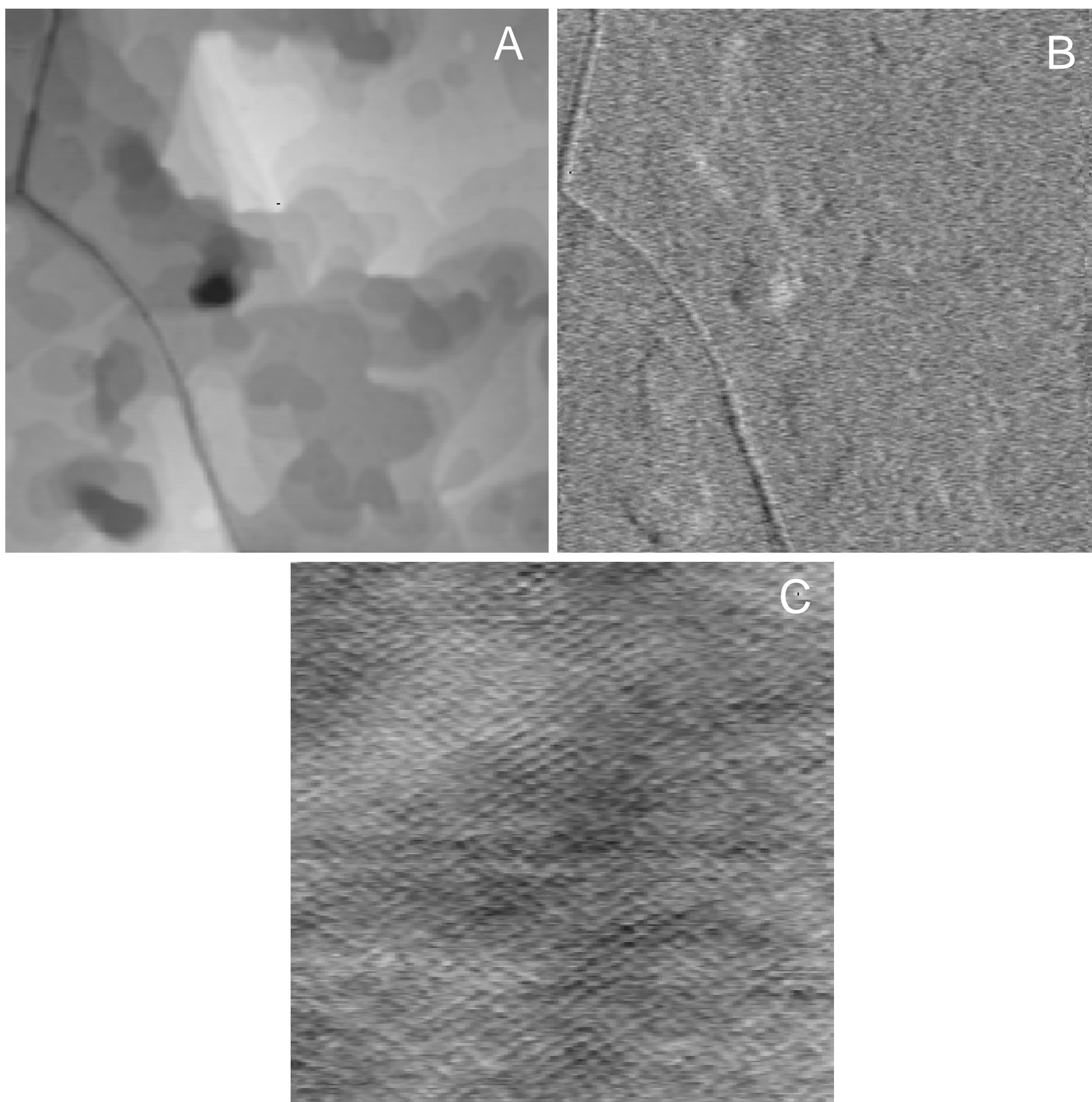

Figure 3.5. AFM images of a bare CH_3 SAM surface. (**A**) 1 μm x 1 μm contact mode image showing the surface topography. The image reveals the underlying (111) Au terraces and step edges. (**B**) The simultaneously recorded lateral force image for the scan in **A**. (**C**) Contact mode imaging in a different, smaller area (17 nm x 17 nm) of the bare SAM reveals the molecular lattice.

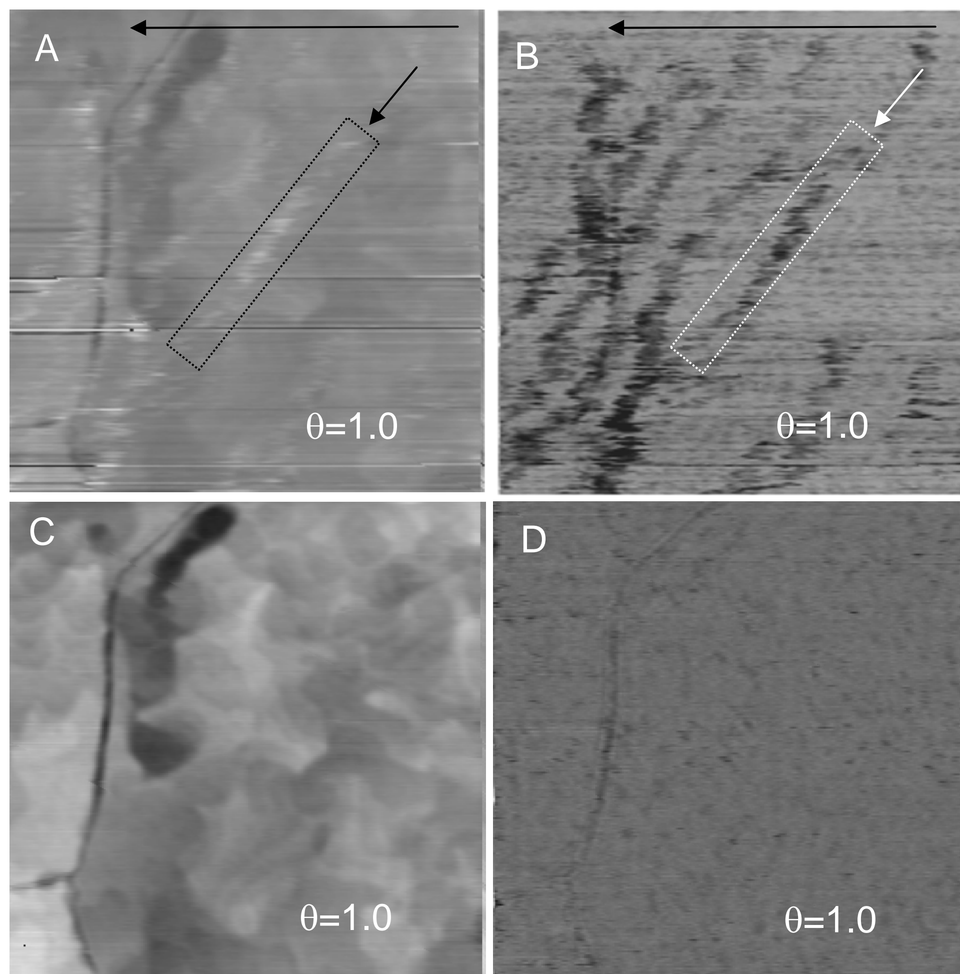

Figure 3.6. Sequentially taken contact (topography) (**A**, **C**) and lateral force (**B**, **D**) AFM images (1 μm x 1 μm) of a fixed area of a CH_3 SAM surface deposited Ti at θ=1.0. (**A**, **B**): The images show the AFM tip coming into contact with a metal cluster, causing the tip to rise, as seen in the topography, and bend laterally, as seen in the lateral force image. As the tip scans laterally across the surface (in the direction of the top black arrows) a newly contacted cluster is pushed ahead of the tip and typically rolled off to the lower side with the tip passing out of contact to the left. Once the tip is returned to a new position just below the original starting point the next scan line typically recontacts the cluster and moves it again towards the lower left. The arrows point to a region which shows the typical locus of the motion of a cluster being swept off to the lower left during

the first scan (faint white spots in contact mode). After completion of the first scan in the indicated area most clusters end up being swept off the image area at the lower left. (**C**, **D**): With the removal of the clusters the topography image regains some sharpness in the resolution of the underlying Au features (**C** vs **A**). In the lateral force image (**D**) note the appearance of small depressions or pits which remain after the clusters are swept off the surface.

and lateral directions. The clusters are observed to be swept by the tip down the image and slightly to the left. The imaging was done in a series of pairs of scans initiated by a linear scan to the left followed by a reset to the right-hand side and slightly down for the next scan to the left. This causes the tip to initially come into contact with the clusters on the bottom left quadrant of the tip, thus pushing the clusters down and to the left as the pairs of scans continue. The lateral force image shows this effect quite clearly as seen by circled diagonal track of a cluster as it is continually imaged and pushed down and to the left. Once the initial scan of the surface area is complete most of the clusters have been swept away as seen by the absence of these features in either in the topography (**c**) or lateral force (**d**) images. Images of the lattice are possible at this stage but the detailed features are not as clear as in the bare monolayer. Possible causes include a slight disordering of the monolayer, dulling of the tip caused by reaction with titanium, or clusters adhering to the tip.

While the Ti clusters are easily moved by the AFM tip at low coverages (Figure 3.6, $\theta = 1.0$), with increasing deposition the clusters start to become firmly attached. For

example, figures 4.7A-4.7C show contact mode images of a surface for $\theta = 5$ where the images were taken after multiple initial scans in which all the smaller clusters were "swept" aside. It is still possible to see signs of the underlying structure of the Au, however, only the larger features are evident and the steps on the surface are not as sharp as in bare monolayer images. The diminishing of the image quality is likely due to contributions from both intrinsic sample degradation and diminishing of the tip sharpness from continued scanning across the rough surface. Some of the clusters at this growth stage are too large to be easily moved by the tip, and even after multiple scans are not removed from the scan area, as seen by the small, light colored features, marked by arrows in figures 4.7A,B. While the smaller clusters have been moved out of the image, signs of where they originally were are evident in the form of pits left behind. The length of the pits (~10-50 nm) is determined by the tip induced translation across the surface. The depth (~0.2-1 nm), however, seems intrinsic to the deposition process and is assigned primarily to the chemical attack of the deposited metal atoms on the SAM in which carbide phases form at the Ti metal/SAM interface. Continued chemical attack at the alkyl chains would drive this interface deeper into the SAM. Formation of the pits then could occur dynamically by fracture at these buried SAM/carbide interfaces to remove the inorganic composite object. The reason some clusters stay in place under tip contact is likely due to the specific details of the carbide-SAM interface topography.

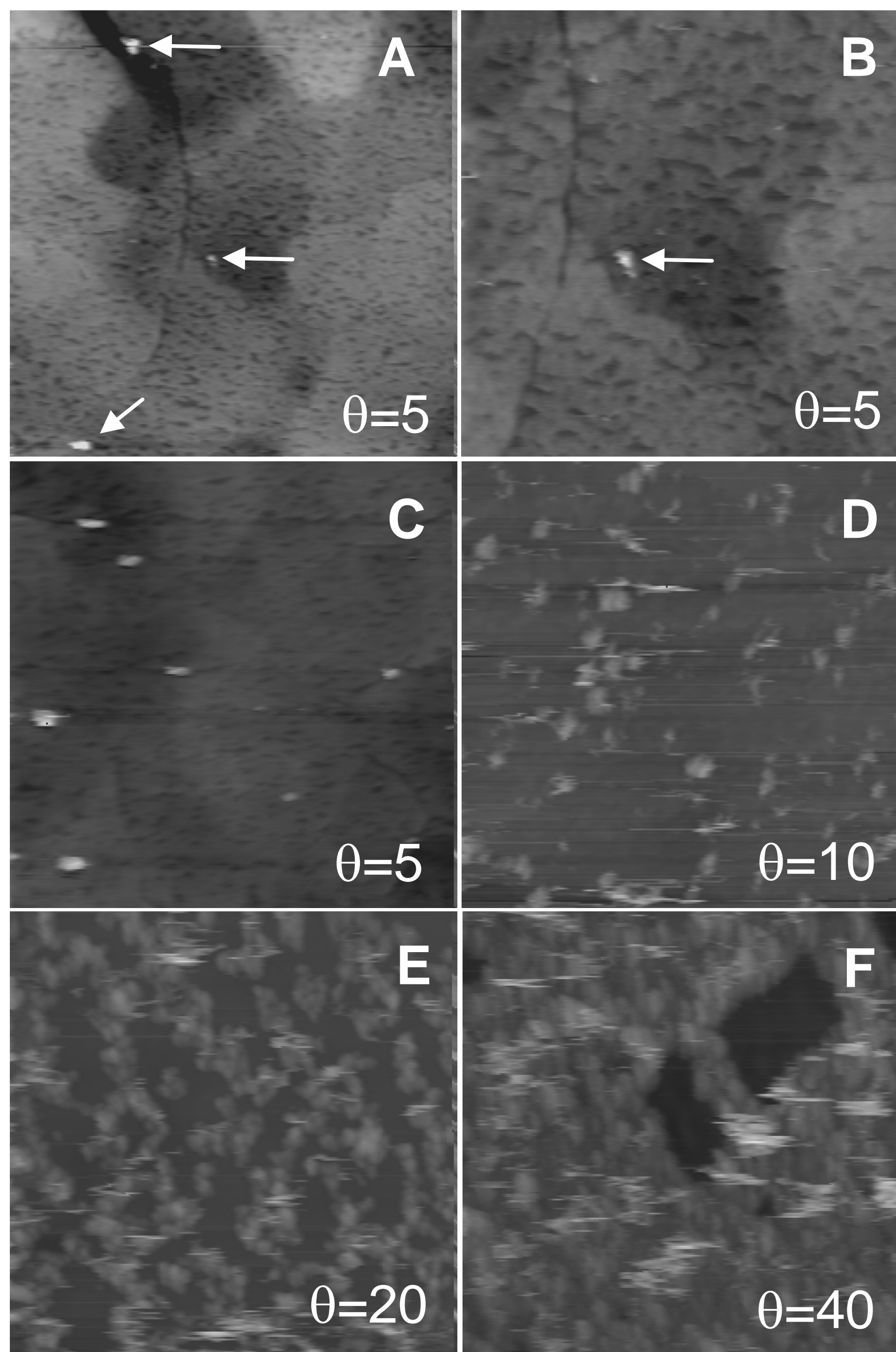

Figure 3.7. Contact mode AFM images of SAMs after deposited Ti. (**A**) A 1 μm x 1 μm image of a $\theta = 5$ deposition sample after sweeping the surface with the tip for multiple full scans to remove most of the Ti clusters. Notice the small pits (dark spots)

scattered all across the surface which show where the metal clusters originally grew and reacted with the monolayer. The arrows indicate firmly anchored Ti clusters that were not moved by the tip. (**B**) The same region as in **A** but a 0.5 μm x 0.5 μm image which shows the pits in more detail. Typically, the pits are rectangular or oblong as a result of the tip dragging the metal clusters to the left with the initial scan and they vary in depth from ~0.2 – 1.0 nm. (**C**) A 1 μm x 1 μm image for the θ = 5 sample taken in different area which shows both pits and several of the more firmly anchored remaining clusters. (**D, E, F**) 1 μm x 1 μm images of θ = 10, 20 and 40 samples taken on the first scan after an initial scan to sweep the surface. Note that at these higher coverages the tip is generally unable to move the clusters at the forces used and sweeping has little effect on subsequent scans. The surface density of clusters increases with the amount of deposited metal until at θ = 40 the sample surface is almost entirely covered. The open rectangular patches at θ = 40 appear to be intrinsic to the surface structure since these types of features with varying shapes and sizes are seen scattered on the surfaces for different samples and surface regions. The presence of these features indicates that complete contact of the surface by the deposited metal requires quite high coverages.

As the deposition increases to the range of tens of Ti atoms per SAM molecule it becomes difficult to move any of the clusters during scanning. For example, in Figure 3.7D for θ=10, many smaller clusters remain on the surface after an initial contact mode scan and periodically cause ‘tip jumps’ or streaks in the images when the tip comes in

contact with them. With increasing deposition (Figure 3.7E, θ=20) more clusters form and the typical sizes increase as the SAM begins to be covered with the metal overlayer. Finally, at the highest coverage shown (Figure 3.7F, θ=40) the metal nearly completely covers the SAM. Note the open areas which are typically observed across different regions of the surfaces. These areas indicate that incoming vapor Ti atoms still appear to scatter off of exposed SAM regions with a high probability since all areas are uniformly exposed to the atom flux. In general, imaging of the high Ti coverage samples (θ>10) becomes increasingly difficult as the tip sticks to the surface in many places, likely caused by the silicon tip forming a chemical bond to the Ti surfaces. Force curves done on the surface to find the adhesive force were unsuccessful due to a limited z scan range (~100 nm) such that the tip was not able to retract far enough to disengage with the surface.

3.3.4 ToF-SIMS – Localized Chemical Degradation

The ToF-SIMS data (Figure 3.8) were collected primarily to further clarify the heterogeneity and the interface chemistry of the evolving metal overlayers. The heterogeneity is demonstrated by the slow decreases of the Au^+ substrate ion peak (Figure 3.8A) and the adsorbate molecular peaks ($[AuS(CH_2)_{16}]^+$, Figure 3.8B; Au_2M^- and AuM_2^-, where M = adsorbate molecule, Figure 3.8CD). All of these signals are observed even up to a coverage of θ~50. Given the shallow sampling depth of the technique (~1 nm) these data are consistent with the gradual covering of the SAM by a Ti overlayer, leaving large fractions of open SAM areas until high deposition amounts, in agreement with the AFM observations.

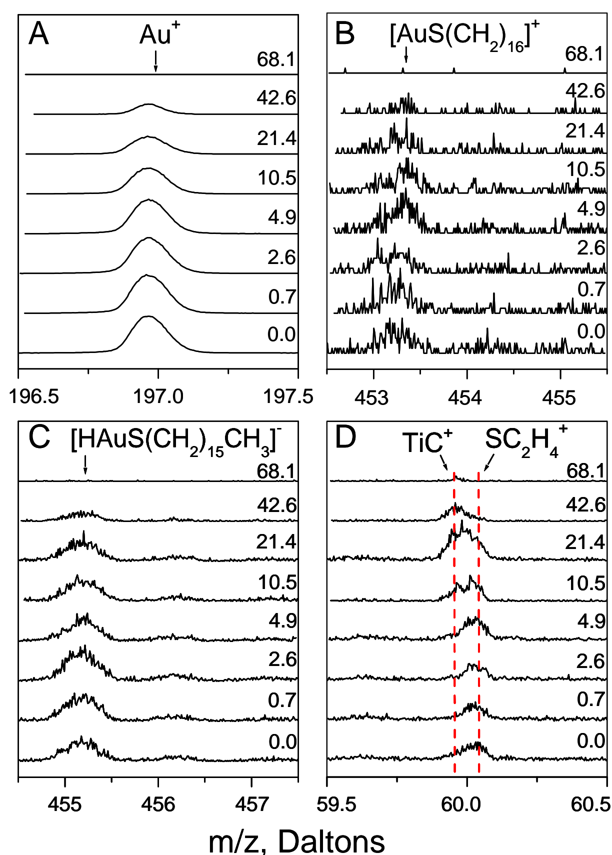

Figure 3.8: High resolution ToF-SIMS spectra of selected ion peaks at varying total coverages of deposited Ti on the SAM. (**A**) Au^+, (**B**) AuM^+, (**C**), $HAuM^-$; where M ≡ -$S(CH_2)_{16}$, (**D**) $^{48}TiC^+$ and $SC_2H_4^+$. The peak intensities are in arbitrary units with different scales for each spectrum.

Evidence for a chemical reaction of Ti with the SAM to form some type of carbide species is supported by the appearance of the $^{48}TiC^+$ peak (Figure 3.8D; the accompanying $SC_2H_4^+$ cluster peak is marked for clarity) as the deposition increases.

This feature becomes relatively strong for $\theta \sim 20$ but eventually starts decreasing for $\theta \sim 50$, consistent with the point at which complete Ti overlayers form. The lack of a significant signal at early deposition times could imply that no carbides form or that the carbides form at the SAM/metal interface under a Ti metal cluster or nanoparticle which would diminish any ion signals. Since the XPS data indicate early formation of carbide we conclude that the carbide products form at the Ti/SAM interface, as would be expected on the basis of reaction at the metal-molecule contact point.

3.4 Discussion

The combined data for our specific deposition conditions all point to a complex deposition process involving both scattering of the Ti atoms from the SAM surface and severe degradation of the alkyl chains in localized regions across the surface. The main features of the mechanism concluded from our data are summarized pictorially in the schematic in Figure 3.9 and the proposed set of underlying kinetic processes are listed in steps 1-7. We note at the outset of this discussion that these results and conclusions are specific to the conditions of a room temperature sample with a Ti deposition rate of ~0.15 Ti atoms$\cdot$nm$^{-2}\cdot$s^{-1} (~0.033 Ti atoms$\cdot$molecule$^{-1}\cdot$s^{-1}; or equivalently ~1.0 Ti atom$\cdot$molecule^{-1} every 30 s).

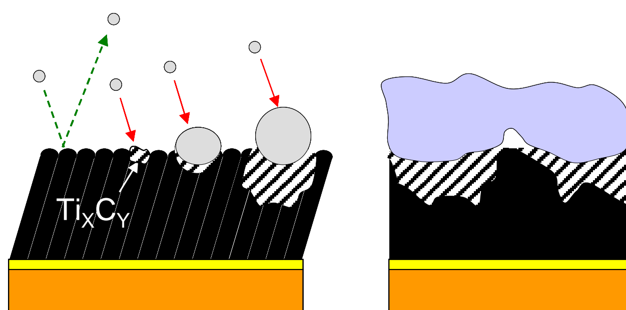

Figure 3.9: Schematic of the major features arising in the vapor deposition of Ti atoms on a hexadecanethiolate/Au SAM as concluded from the data obtained from multiple in-situ characterization probes. The left hand drawing illustrates for an incoming Ti atom, from left to right, unreactive scattering of an incoming Ti atom off the SAM surface, formation of a carbide reaction product after collision of a Ti atom with the SAM surface, nucleation and growth of a Ti cluster or nanoparticle at a previously reacted surface site, and continued reaction of deposited Ti atoms with -CH_2- units deep into the SAM. The right hand drawing illustrates the possible characteristics that arise in the later stages of deposition where a complete metal overlayer can form. Note the extensive carbide interphase that forms and the likely formation of voids at the SAM/inorganic interface, which would be caused by the highly heterogeneous character of the growth process across the surface.

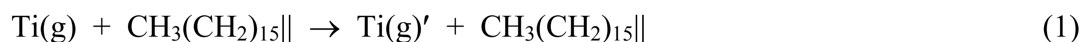

$$Ti(g) + CH_3(CH_2)_{15}|| \rightarrow Ti(g)' + CH_3(CH_2)_{15}|| \quad (1)$$

$$Ti(g) + CH_3(CH_2)_{15}|| \rightarrow Ti(s) \quad (2a)$$

$$Ti(g) + {}^*CH_3(CH_2)_{15}|| \rightarrow {}^{\pm}(\mathbf{Ti\text{-}CH_3})(CH_2)_{15}|| \quad (2b)$$

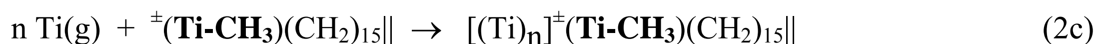

$$n\,Ti(g) + {}^{\pm}(\mathbf{Ti\text{-}CH_3})(CH_2)_{15}|| \rightarrow [(Ti)_n]^{\pm}(\mathbf{Ti\text{-}CH_3})(CH_2)_{15}|| \quad (2c)$$

$$Ti(s) \rightarrow Ti(s)' \quad (3a)$$

$$n\,Ti(s) \rightarrow [Ti(s)]_n \quad (3b)$$

$$\mathrm{Ti(s)} + {}^{*}\mathrm{CH_3(CH_2)_{15}}|| \rightarrow {}^{\pm}(\mathbf{Ti\text{-}CH_3})\mathrm{(CH_2)_{15}}|| \quad (4)$$

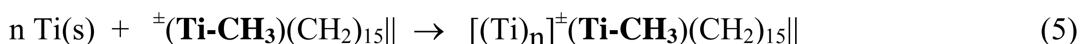

$$\mathrm{n\ Ti(s)} + {}^{\pm}(\mathbf{Ti\text{-}CH_3})\mathrm{(CH_2)_{15}}|| \rightarrow [\mathrm{(Ti)_n}]^{\pm}(\mathbf{Ti\text{-}CH_3})\mathrm{(CH_2)_{15}}|| \quad (5)$$

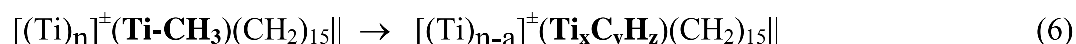

$$[\mathrm{(Ti)_n}]^{\pm}(\mathbf{Ti\text{-}CH_3})\mathrm{(CH_2)_{15}}|| \rightarrow [\mathrm{(Ti)_{n\text{-}a}}]^{\pm}(\mathbf{Ti_xC_yH_z})\mathrm{(CH_2)_{15}}|| \quad (6)$$

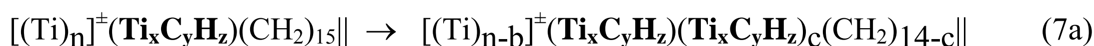

$$[\mathrm{(Ti)_n}]^{\pm}(\mathbf{Ti_xC_yH_z})\mathrm{(CH_2)_{15}}|| \rightarrow [\mathrm{(Ti)_{n\text{-}b}}]^{\pm}(\mathbf{Ti_xC_yH_z})(\mathbf{Ti_xC_yH_z})_c\mathrm{(CH_2)_{14\text{-}c}}|| \quad (7a)$$

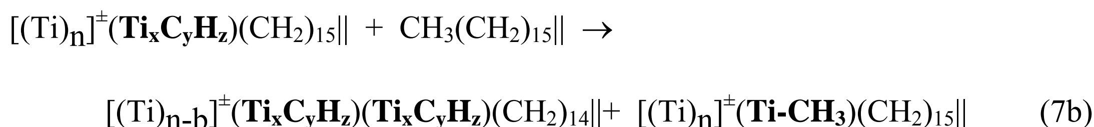

$$[\mathrm{(Ti)_n}]^{\pm}(\mathbf{Ti_xC_yH_z})\mathrm{(CH_2)_{15}}|| + \mathrm{CH_3(CH_2)_{15}}|| \rightarrow$$

$$[\mathrm{(Ti)_{n\text{-}b}}]^{\pm}(\mathbf{Ti_xC_yH_z})(\mathbf{Ti_xC_yH_z})\mathrm{(CH_2)_{14}}|| + [\mathrm{(Ti)_n}]^{\pm}(\mathbf{Ti\text{-}CH_3})\mathrm{(CH_2)_{15}}|| \quad (7b)$$

It is clear from the QCM and XPS data that a large fraction of the incoming Ti vapor atoms in the initial stages of deposition simply scatter off the surface [extreme left of Figure 3.9 and step 1 (g signifies gas phase; || signifies surface)]. Thus in spite of the high chemical reactivity of Ti, as evidenced in later stages by the severe degradation of the molecules, the sticking coefficient does not reach unity after ~ 30 Ti atoms per molecule have adhered at the surface (Figure 3.1). As the deposition continues from the initial stages an increasing number of Ti atoms are accommodated at the surface to create nucleation sites. This could occur by a combination of thermal accommodation to simply lower the kinetic energy of the Ti to prevent release from the surface [step 2a (s signifies surface)] or immediate chemical reaction with a CH_3 group (step 2b). Reaction could occur if the impacting Ti atom is on the high end of the Boltzmann energy tail, sufficient to overcome an activation barrier, and/or if the adsorption site is a surface defect of some type which facilitates the energetics or configurational requirements of the reaction (as marked by a * in the reaction step). Such defects could include, for example, a

disordered chain end or a molecular ensemble which has been topographically elevated due to underlying substrate defects. The intermediate reaction product in step 2b [where the ± represents a reacted chain and (**Ti-CH_3**) represents a reaction product with one Ti] presumably involves some type of insertion of a Ti atom into a C-H bond of the CH_3 tail group. If any Ti(s) species form they could diffuse across the surface and eventually cluster (steps 3a,b) to form unreacted Ti clusters or react with a CH_3 group (step 4). The growth of unreacted clusters (step 3b), however, seems somewhat unlikely since the combination of the XPS, IRS and AFM data suggest that reaction to carbide starts in the very initial stages of deposition, so the probability of unreacted metal being directly in contact with the SAM is small.

The continual increase in the sticking coefficient with increasing Ti coverage implies that an increasing number of nucleation centers appear, which can either accommodate incoming Ti(g) atoms or trap surface diffusing Ti(s) atoms. The AFM, XPS and IRS suggest the nucleation centers consist mostly of reacted CH_3 groups [step 2c for Ti(g) and step 5 for Ti(s)], as shown by the continual formation of carbide product(s) and increasingly deep monolayer damage (from AFM). As the Ti surface coverage grows it is important to note that the AFM (Figure 3.7) shows a significant fraction of open surface, even up to tens of Ti atoms adsorbed per SAM molecule. This result is supported by the ToF-SIMS data (Figure 3.8) which indicate long deposition times are required to completely block the SAM and prevent ejection of SAM and Au substrate fragments. These data suggest that in bare areas of the SAM surface the sticking coefficient remains at the low values observed in the initial stages of the deposition. This implies to us that initial nucleation requires a reactive surface defect of

some type (steps 2b or 4) such that any local region free of such defects will remain bare until late in the deposition.

As the deposition proceeds to values of $\theta \vee 5$ the IRS and AFM data indicate attack begins to proceed deep into the SAM, progressing along the methylene units of the alkyl chains. The AFM data clearly show that this degradation proceeds at growing Ti cluster sites, which suggests a mechanism involving diffusion of Ti atoms from the growing cluster into the contiguous SAM molecules and down the chains, either on the originally reacted chain (steps 6 and 7a) or onto a neighboring unreacted chain (step 7b). This seems reasonable in view of the extensive destruction of the hydrocarbon material which should lead to a nanoporous carbide/hydride material with multiple diffusion channels for Ti atoms.

In the final stages of the deposition a complete overlayer forms. As depicted in Figure 3.9, however, it is likely that the highly heterogeneous morphology of the Ti film, especially with open areas such as seen in the AFM image in Figure 3.7F, will likely lead to incomplete contact across the surface, i.e., the formation of voids at the SAM/Ti interface.

3.5 Conclusions

The combination of four in-situ surface analysis techniques show that under the conditions of Ti deposition at ~0.15 Ti atoms$\cdot$nm$^{-2}\cdot$s^{-1} onto the surface of an ambient temperature $CH_3(CH_2)_{15}S$-/Au{111} SAM, a very heterogeneous Ti overlayer forms in a process in which a large fraction of impinging Ti atoms do not stick to the bare SAM surface in spite of the high reactivity of Ti atoms with the SAM molecules. Initial

nucleation of Ti at the surface appears to involve primarily chemical degradation with the CH_3 groups of the SAM to form carbide, and presumably hydride, products. Growth of Ti clusters appears to be concentrated at these scattered reaction centers. The SAM molecules in the local vicinity are subsequently degraded to inorganic products, progressing deeper into the SAM as the deposition proceeds with reaction reaching depths of ~0.5 nm, approximately halfway along the alkyl chains to give a highly heterogeneous inorganic/organic nanocomposite. A complete overlayer does not form until metal coverages approach 50 Ti atoms per SAM molecule. The highly heterogeneous morphology of the growing film until these last stages suggests that the underlying SAM/Ti interface is not complete and exhibits voids.

These data show that for applications such as molecular electronics devices, where the formation of a clean, uniform metal/SAM interface is typically desired, the use of Ti may be highly problematic, suffering from both a highly heterogeneous contact area and the presence of inorganic products such as nonstoichiometric carbides and hydrides. On the other hand, by the use of careful control of the deposition conditions, kinetic energy of the metal atoms in the vapor, sample temperature, background gas pressure and SAM chemical composition, there would appear to be opportunities to synthesize unique types of thin film inorganic composites with unique and useful properties for a variety of applications. The most promising variables would appear to be the control of the incoming atom energies and the sample temperatures and such experiments are underway in our laboratories.

3.6 Acknowledgements

The authors gratefully acknowledge financial support from the National Science Foundation (NSF), the Defense Advanced Project Agency, The Air Force Office of Scientific Research and the Penn State NSF MRSEC program.

References

[1] Jung, D. R.; Czanderna, A. W. *Crit. Rev. Solid State* **1994**, *19*, 1-54.

[2] Herdt, G. C.; King, D. E.; Czanderna, A. W. *Z. Phys. Chem.* **1997**, *202*, 163-196.

[3] Hooper, A.; Fisher, G. L.; Konstadinidis, K.; Jung, D.; Nguyen, H.; Opila, R.; Collins, R. W.; Winograd, N.; Allara, D. L. *J. Am. Chem. Soc.* **1999**, *121*, 8052-8064.

[4] Fisher, G. L.; Hooper, A. E.; Opila, R. L.; Allara, D. L.; Winograd, N. *J. Phys. Chem. B* **2000**, *104*, 3267-3273.

[5] Fisher, G. L.; Walker, A. V.; Hooper, A. E.; Tighe, T. B.; Bahnck, K. B.; Skriba, H. T.; Reinard, M. D.; Haynie, B. C.; Opila, R. L.; Winograd, N.; Allara, D. L. *J. Am. Chem. Soc.* **2002**, *124*, 5528-5541.

[6] Walker, A. V.; Tighe, T. B.; Reinard, M. D.; Haynie, B. C.; Allara, D. L.; Winograd, N. *Chem. Phys. Lett.* **2003**, *369*, 615-620.

[7] Walker, A. V.; Tighe, T. B.; Stapleton, J.; Haynie, B. C.; Upilli, S.; Allara, D. L.; Winograd, N. *Appl. Phys. Lett.* **2004**, *84*, 4008-4010.

[8] Walker, A. V.; Tighe, T. B.; Cabarcos, O. M.; Reinard, M. D.; Haynie, B. C.; Uppili, S.; Winograd, N.; Allara, D. L. *J. Am. Chem. Soc.* **2004**, *126*, 3954-3963.

[9] Zhou, C.; Deshpande, M. R.; Reed, M. A.; Jones, L.; Tour, J. M. *Appl. Phys. Lett.* **1997**, *71*, 611-613.

[10] Collet, J.; Vuillame, D. *Appl. Phys. Lett.* **1998**, *73*, 2681-2693.

[11] Allara, D. L.; Dunbar, T. D.; Weiss, P. S.; Bumm, L. A.; Cygan, M. T.; Tour, J. M.; Reinerth, W. A.; Yao, Y.; Kozaki, M.; Jones, L. *Ann. N. Y. Acad. Sci.* **1998**, *852*, 349-

370.

[12] Collier, C. P.; Wong, E. W.; Belohradsky, M.; Raymo, F. M.; Stoddart, J. F.; Kuekes, P. J.; Williams, R. S.; Heath, J. R. *Science* **1999**, *285* , 391-394.

[13] Chen, J.; Reed, M. A.; Rawlett, A. M.; Tour, J. M. *Science* **1999**, *286*, 1550-1552.

[14] Chen, J.; Wang, W.; Reed, M. A.; Rawlett, A. M.; Price, D. W.; Tour, J. M. *Appl. Phys. Lett.* **2000**, *77*, 1224-1226.

[15] Reed, M. A.; Chen, J.; Rawlett, A. M.; Price, D. W.; Tour, J. M. *Appl. Phys. Lett.* **2001**, *78*, 3735-3737.

[16] Collier, C.P.; Mattersteig, G.; Wong, E.W.; Luo, Y.; Beverly, K.; Sampaio, J.; Raymo, F.M.; Stoddart, J.F.; Heath, J.R.; *Science*, **2000**, *289*, 1172-1175.

[17] Collier, C. P.; Jeppesen, J. O.; Luo, Y.; Perkins, J.; Wong, E. W.; Heath, J. R.; Stoddart, J. F. *J. Am. Chem. Soc.* **2001**, *123*, 12632-12641.

[18] Metzger, R. M.; Xu, T.; Peterson, I. R. *J. Phys. Chem. B* **2001**, *105*, 7280-7290.

[19] Chen, J.; Reed, M. A. *Chem. Phys.* **2002**, *281*, 127-145.

[20] Chang, S. C.; Li, Z. Y.; Lau, C. N.; Larade, B.; Williams, R. S. *Appl. Phys. Lett.* **2003**, *83*, 3198-3200.

[21] Vuillaume, D.; Lenfant, S. *Microelectron. Eng.* **2003**, *70*, 539-550.

[22] Lenfant, S.; Krzeminski, C.; Delerue, C.; Allan, G.; Vuillaume, D. *Nano Letters* **2003** , *3*, 741-746.

[23] McCreery, R.; Dieringer, J.; Solak, A. O.; Snyder, B.; Nowak, A. M.; McGovern, W. R.; DuVall, S. *J. Am. Chem. Soc.* **2003**, *125*, 10748-10758.; McCreery, R.; Dieringer, J.; Solak, A. O.; Snyder, B.; Nowak, A. M.; McGovern, W. R.; DuVall, S.

J. Am. Chem. Soc. **2004**, *126*, 6200.

[24] de Boer, B.; Frank, M. M.; Chabal, Y. J.; Jiang, W. R.; Garfunkel, E.; Bao, Z. *Langmuir* **2004**, *20*, 1539-1542.

[25] Jung, G. Y.; Ganapathiappan, S.; Li, X.; Ohlberg, D. A. A.; Olynick, D. L.; Chen, Y.; Tong, W. M.; Williams, R. S. *Appl. Phys. A* **2004**, *78*, 1169-1173.

[26] McCreery, R. L. *Chem. Mater.* **2004**, *16*, 4477-4496.

[27] Stewart, D. R.; Ohlberg, D. A. A.; Beck, P. A.; Chen, Y.; Williams, R. S.; Jeppesen, J. O.; Nielsen, K. A.; Stoddart, J. F. *Nano Letters* **2004**, *4*, 133-136.

[28] Lau, C. N.; Stewart, D. R.; Williams, R. S.; Bockrath, M. *Nano Letters* **2004**, *4*, 569-572.

[29] Haick, H.; Ambrico, M.; Ghabboun, J.; Ligonzo, T.; Cahen, D. *Phys. Chem. Chem. Phys.* **2004**, *6*, 4538-4541.

[30] Konstadinidis, K.; Taylor, A.J.; Miller, A.C.; Opila, R.L. *J. Adhes.*, **1994**, *46*, 197-213.

[31] Tachibana, T.; Williams, B. E.; Glass, J. T. *Phys. Rev. B* **1992**, *45*, 11975-11981.

[32] Bodo, P.; Sundgren, J. E. *J. Vac. Sci. Technol. A* **1984**, *2*, 1498-1502.

[33] Bodo, P.; Sundgren, J. E. *J. Appl. Phys.* **1986**, *60*, 1161-1168.

[34] Ohuchi, F. S.; Freilich, S. C. *J. Vac. Sci. Technol. A* **1986**, *4*, 1039-1045.

[35] Du, M.; Opila, R. L.; Case, C. *J. Vac. Sci. Technol. A* **1998**, *16*, 155-162.

[36] Konstadinidis, K.; Zhang, P.; Opila, R. L.; Allara, D. L. *Surf. Sci.* **1995**, *338*, 300-312.

[37] Allara, D. L.; Nuzzo, R. G. *Langmuir* **1985**, *1*, 52-66.

---

[38] Nuzzo, R. G.; Dubois, L. H.; Allara, D. L. *J. Am. Chem. Soc.* **1990**, *112*, 558-569.

[39] Laibinis, P. E.; Whitesides, G. M.; Allara, D. L.; Tao, Y. T.; Parikh, A. N.; Nuzzo, R. G. *J. Am. Chem. Soc.* **1991**, *113*, 7152-7167.

[40] MacPhail, R. A.; Strauss, H. L.; Snyder, R. G.; Elliger, C. A. *J. Phys. Chem.* **1984**, *88*, 334-341.

[41] Laibinis, P. E.; Nuzzo, R. G.; Whitesides, G. M. *J. Phys. Chem.* **1992**, *96*, 5097-5105.

[42] Braun, R.M.; Blenkinsopp, P.; Mullock, S.J.; Corlett, C.; Willey, K.F.; Vickerman, J.C.; Winograd, N. *Rapid Commun. Mass. Spec.*, **1998**, *12*, 1246-1252.

[43] In order to achieve high signal/noise, custom built phase locked loop setups were utilized using a Hewlett Packard 8656B signal generator, an EG&G 5202 lock-in-amplifier, 2 Hewlett Packard 3478A Multimeters, and a Hewlett Packard 53181A Frequency Counter. The latter two were interfaced to a PC using National Instruments LabVIEW software. This setup gave a ±0.05 Hz noise level, which is equivalent to $_M$ = ±0.02. The SAM functionalized QCM crystal and Au reference crystals were placed side by side, the same distance from the deposition source and the sample QCM holder temperature controlled at ~25 °C (the approximate SAM sample temperatures in the actual analysis experiments) using circulated water. The SAM QCM crystals (Cold Springs R&D, Syracuse, NY) were highly polished on one side to an rms roughness (tapping mode AFM) of 0.1-0.2 nm which resulted in the QCM SAM surfaces having near identical rms roughnesses to those of the SAMs prepared on silicon substrates.

[44] Sticking probabilities were estimated from the area ratios of the metal core level peaks to the Au 4f and C 1s peaks using instrument determined cross sections [e.g., see Briggs, D.; Grant, J. T. (Eds.); Surface Analysis by Auger and X-ray Photoelectron Spectroscopy, IM Publications, West Sussex, UK, **2003**]. Estimates were not made above θ=10 because of the increasing uncertainty in applying the

necessary photoelectron mean free path corrections to the heterogenous Ti films with varying thicknesses of metal across the surface (*e.g.*, as shown by our AFM data).

45 Georgiev, D. G.; Baird, R. J.; Newaz, G.; Auner, G.; Witte, R.; Herfurth, H. *App. Surf. Sci.* **2004**, *236*, 71-76.

46 Wagner, C. D.; Naumkin, A. V.; Kraut-Vass, A.; Allison, J. W.; Powell, C. J., Rumble, J. R. (Eds.); *NIST X-ray Photoelectron Spectroscopy Database 20*, v*ersion 3.4* (Web Version), NIST, Gaithersburg, MD, **2003**.

47 Schmiedgen, M.; Graat, P.C.J.; Baretzky, B.; Mittemeijer, E.J.; *Thin Solid Films*, **2002**, *415*, 114-122.

48 In general, because of the heterogeneous nature of the deposited Ti (e.g., see AFM data), quantitative analysis of the various core level peaks in the XPS spectra was not performed.

49 Parikh, A. N.; Allara, D. L. *J. Chem. Phys.*, **1992**, *96*, 927-945.

50 Strunksus, T.; Grunze, M.; Kochendoerfer, G.; Wöll, Ch. *Langmuir* **1996**, *12*, 2712-2725.

51 Poirier, G.E.; Tarlov, M.J. *Langmuir* **1994**, *10*, 2853-2856.

52 Delamarche, E.; Michel, B.; Gerber, C.; Anselmetti, D.; Guntherodt, H.J.; Wolf, H.; Ringsdorf, H. *Langmuir* **1994**, *10*, 2869-2871.

Chapter 4

Investigation of the Growth Mechanisms and Interface Properties of α,ω-Mercaptoalkanoic Acid Multilayer Films

4.1 Introduction

The use of self-assembled, multilayer molecular films as precision spacers (“molecular rulers”) for lithographic processing has been reported recently.[1-4] These reports indicate that appropriate molecular ruler films (MRFs), in conjunction with liftoff or other standard lithographic techniques, can be used on surfaces with nominal micrometer scale patterns, previously created by standard lithographic processing (e.g., photolithography), to create final topographical features in the 1-100 nm width range. Such a capability, if sufficiently precise and generally applicable, would fill a longstanding gap in patterning by providing designed, precision dimensions down to the molecular scale.

The present state-of-the-art is based on alkanethiol-gold chemistry and thus presently is limited to patterning gold features,[1-4] though suitable chemistries should allow extensions to other materials. In detail, multilayer stacks of self-assembled monolayers (SAMs), each with a predesigned thickness, are formed layer by layer on a foundation SAM of an ω-carboxyalkanethiolate SAM on Au{111} [$HO_2C(CH_2)_nS$–/Au].[5] The foundation SAM is prepared on a surface with gold features, e.g., μm-width gold posts or lines on a silicon oxide substrate, with the SAM forming selectively on and conformal to the gold features. While a number of methods are available for forming conformal multilayers,[6-15] the current work is based on the method developed by Ulman and co-workers[6] which uses stacks of α,ω-mercaptoalkanoic acid layers ligated at their interfaces by copper ions. The self-assembly was proposed[6] to follow steps represented schematically in Figure 4.1. Once the foundation SAM is formed, by iterations of the subsequent steps with selected constituent molecules of specific molecular lengths the

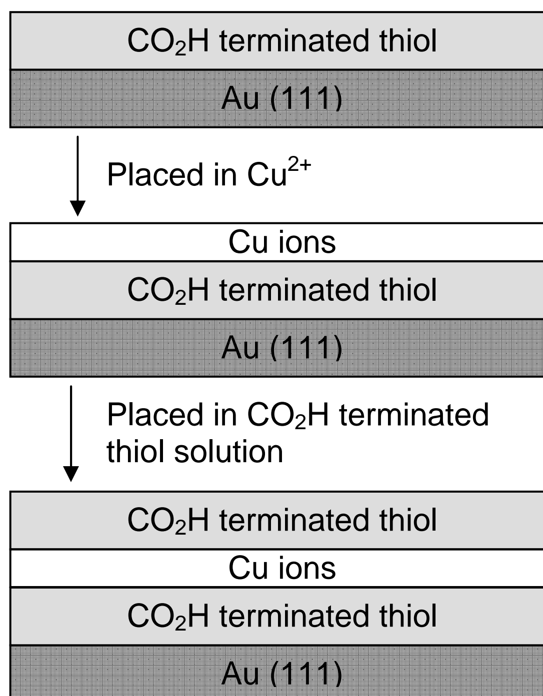

Figure 4.1: Schematic summarizing the formation of multilayers using the method of Ulman and co-workers (reference 6). The steps are: 1.) formation of an α,ω-mercaptoalkanioc acid/Au SAM; 2.) coordination of neighboring CO_2H terminal groups with Cu^{2+} ions; 3.) formation of an overlayer of α,ω-mercaptoalkanoic acid molecules via (RSH)−Cu interaction. Steps 2 and 3 are repeated to build the stack layer by layer.

thickness of the final stack, in principle, can be precisely controlled. Following the current reports,[1-4] a typical patterning process would involve: 1.) fabrication of gold features on the oxide layer of a silicon substrate, 2.) selective formation of a conformal MRF stack, terminated by a simple alkanethiol SAM, on the gold features, 3.) vapor

deposition of gold over the entire surface, and 4.) removal of the gold (liftoff) selectively from the low energy MRF surface. In this mode the MRF acts as a release agent. This process results in formation of a new gold feature formed between the original ones with original-new feature separation gaps determined by the selected thickness of the MRF stack. As a final step the feature edges can be cleaned by oxidative or other methods. Variations of the process steps can be designed to give different types of new features and gaps.

The success of MRFs in forming precision nanometer scale features with sharp, highly replicating feature edges and gap widths will depend critically on the ability to control the precision of the thickness and surface roughness of the MRFs as well as the interfacial topography and adhesive interaction of the deposited metal overlayer with the molecular films. In this regard, the growth of the α,ω-mercaptoalkanoic acid/Cu^{2+} MRFs has been proving to be problematic. For example, recent work has shown that while <10 nm junctions can be fabricated with MRF liftoff processing, poor reproducibility in the electronic characteristics of the resulting structures limits the quality of the information obtainable.[16] In similar work by Weiss and co-workers,[4] the rate of successfully nanofabricated separation using multilayer lithographic techniques decreased as the area of the interface increased.

In order to reliably control the final feature characteristics it is clear that one needs to understand the details of the multilayer growth mechanisms and intermediate layer structures. In the case of the thiocarboxylic acid/Cu^{+2} strategy critical details are lacking. With respect to the interlayer structures and chemistry, the work of Ulman and co-workers provided few details about the interlayer binding chemistry and molecular

packing structures.[7] In a subsequent study, Bard and coworkers,[8] determined that the self-assembly of an α,ω-thioalkanoic acid layer on a CO_2H terminated surface, previously coordinated with Cu^{2+} ions, leads to reduction of the metal to the Cu^{+1} state, but details of the actual molecular structures, coverages and packing were not provided.

Given our long term interest in producing highly precise gaps and features for building molecular electronics devices and other applications, it was of interest to study the details of MRF structures and their growth mechanisms. Since the thiocarboxylic acid/Cu^{+2} films are currently the "standard" system, we focused our initial efforts on these films. In this study we address the nature of the interfacial layers and the chemical reactions that govern them by use of infrared reflection spectroscopy (IRS), X-ray photoelectron spectroscopy (XPS), and single wavelength ellispsometry SWE, along with other ancillary probes. The study is split into three efforts. First, we characterize the interfacial properties of a simple bilayer film built from adsorption of hexadecanethiol [$CH_3(CH_2)_{15}SH$] molecules and their deuterated analogs onto the Cu^{+2}–coordinated surface of $-CO_2H$ terminated SAMs formed from 16-mercaptohexadecanoic SAMs on Au{111} [$HO_2C(CH_2)_{15}S$-/Au], wherein the only interaction of the adlayer with the foundation SAM can be with the SH group. This simplified model system is limited intentionally so that it can only have one interfacial layer to provide maximum information from the characterization data. Second, we used 16-mercaptohexadecanoic acid [$CO_2H(CH_2)_{15}SH$] to form the adlayer and studied the effects of the carboxylic acid on the bilayer formation. Finally, we used and CO_2H terminated SAM formed from 15-mercaptopentadecanoic acid [$CO_2H(CH_2)_{14}S$-/Au] in order to determine if any odd–even alkane chain length variation affects critical features of the multilayer films.[9,17-19] The

results of these experiments improve the understanding of the mechanism and parameter space for growth of this multilayer film and facilitate/enable the use of “molecular ruler” type nanolithography for fundamental research and industrial applications.

4.2. Experimental

4.2.1 Materials

Copper (II) perchlorate hexahydrate [$Cu(ClO_4)_2{\cdot}6H_2O$] (98%, Aldrich), hexadecanethiol [$CH_3(CH_2)_{15}SH$] (95%, Fluka), hydrochloric acid (HCl) (38%, J.T. Baker), ethanol (neat, Pharmco), acetone (98% Aldrich), Milli-Q® water (Millipore Products, Bedford, MA), and hexadecane (99.5%, Aldrich) were used as received. Hexadecanethiol (**MH**) [$CH_3(CH_2)_{15}SH$] (95%, Fluka) and 16-Mercaptohexadecanoic acid (**MHA**) (90%, Aldrich) were recrystallized before use. Deuterated hexadecanethiol ($CD_3(CH_2)_{15}SH$) and 15-Mercaptopentadecanoic acid (**MPA**) were synthesized as previously described.[20,21]

4.2.2 Sample Preparation

The metal films were deposited on silicon substrates (with a native oxide) which were first cleaned with a H_2O_2/H_2SO_4 solution,[22] rinsed with water and ethanol, and finally blown dry with N_2. The metal films were prepared via vapor deposition of a ~ 10 nm thick Cr adhesion layer followed immediately by a ~ 200 nm thick Au layer deposited using a resistively heated boat (pressure maintained continuously at ~10^{-8} torr during both depositions.) The Au/Cr/SiO_2/Si films typically showed roughness RMS values of 1.2 ± 0.2 nm by tapping mode AFM with most values at the lower end of the range. The

freshly evaporated substrates were removed from the deposition chamber, immediately characterized by single wavelength ellipsometry (several spots on each sample) and then placed into the monolayer solution. The total time for this sequence was within ~5 minutes.

The multilayer films were prepared in the following sequential manner: 1.) immersion of the Au substrate in a ~1mM ethanol solution of the MHA or MPA for a pre-selected time in the range of 2 to 24 hours; 2.) removal of the sample, rinsing in ethanol, followed by 5% HCl in ethanol (concentrated aqueous HCl diluted in ethanol) and finally pure ethanol; 3.) immersion in a ~5 mM solution of $Cu(ClO_4)_2$ in ethanol for varying times of up to 3 minutes, removal and washing with neat ethanol; 4.) immersion in a ~5 mM MH ($C_{16}D_{33}SH$ for the IRS samples and MHA or MPA for trilayer samples) solution in ethanol for varying times from 10 minutes to 24 hours, followed by rinsing in ethanol and drying in a N_2 stream. In some cases the final samples were cycled through steps 3 and 4 multiple times. All solutions were made and stored in screw top fluoroware containers. Prior to sample analysis all samples were rinsed with ethanol and blown dry with N_2. All analyses were started within 15 minutes of exposure to atmosphere. For each processing sequence SWE and IRS analyses were done at each step.

4.2.3 Characterization Methods

4.2.3.1 Single Wavelength Ellipsometry (SWE)

The SWE measurements were recorded using a stokes ellipsometer (Gaertner Scientific Corporation, LSE Stokes Ellipsometer, Skokie, IL) set at 632.8 nm and a 70° angle of incidence. The thickness was based on an isotropic film model for the alkane thiol layers

with n, the real part of the complex refractive index, set to 1.5 and k, the imaginary (loss) part, set to zero.[23] For the Cu^{+2} at the SAM surface, n was set to 2.0 with k = 0.[24] More rigorous anisotropic models[25] were not considered since accurate values for the elements of the diagonalized refractive index tensor are not available for the copper interface and the adlayer. In all cases, measurements were taken on three separate points on each sample and the calculated thicknesses then averaged together.

4.2.3.2 Infrared Reflection Spectroscopy (IRS)

Analyses were collected using a custom, in house modified FTIR spectrometer (DigiLab, FTS-7000, Randolph, MA) as described in detail elsewhere[26]. The spectrometer and external optics were purged with CO_2 and H_2O scrubbed air to minimize spectral interferences from these gases. All spectra were taken at an 86° angle of incidence with *p*-polarized light and the instrument resolution set to 2 cm^{-1}. Reflection spectral intensities are reported as $-\log(R/R_0)$, where R is the power reflectivity of the IR beam and R_0 is the reflectivity of a reference sample. R_0 is the spectrum of a $C_{16}D_{33}$-S-/Au{111} SAM or a $C_{16}H_{33}$-S-/Au{111} SAM depending on the specific spectral region of interest for the sample.

Quantitative IRS in conjunction with theoretical simulations was used to determine the average molecular tilt (θ) and twist (ψ) angles of the molecules in the SAMs (Figure 4.2). The analyses used are briefly summarized for reference; for details see previously published work.[26,27] The vibrational modes utilized in the orientation analysis and the

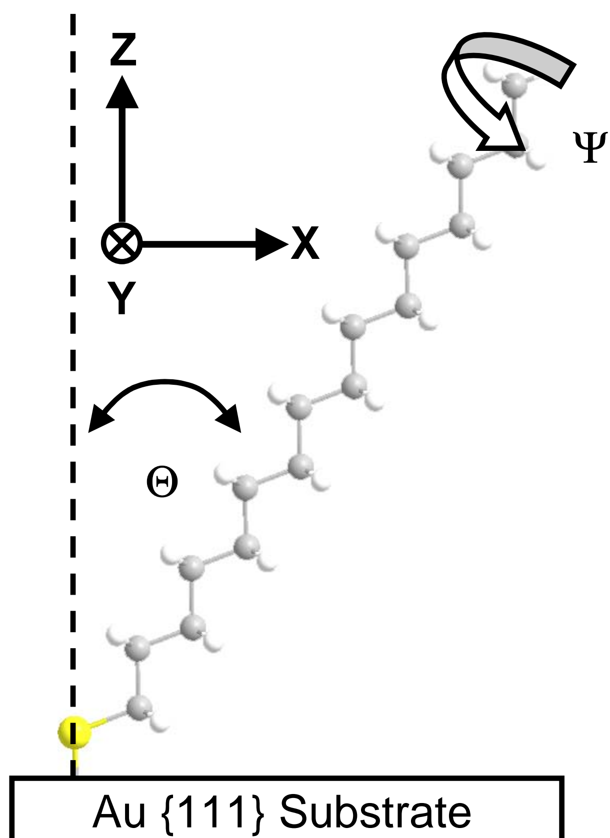

Figure 4.2. Definition of the tilt (θ) and twist (Ψ) angles of an alkane thiol molecule relative to the laboratory coordinate system, where the laboratory coordinate Z is perpendicular to the sample surface, the xyz molecular coordinate system is aligned with the laboratory XYZ system.

assigned transition dipole directions were based on literature assignments.[26-33] Quantitative transmission spectra of a pure compound dispersed in KBr were used to generate optical function spectra (n,k).[26] Using these data and standard algorithms,[26] sets of simulated anisotropic monolayer spectra were generated for varying molecular tilt and twist angles at selected thickness of the film of spectral interest. As shown previously, the r^+, r_a^- and r_b^- modes are problematic for determining the molecular orientations, and were not fitted in this study.[26]

4.2.3.3 X-Ray Photoelectron Spectroscopy (XPS)

The XPS analyses were performed on a monochromatic Al Kα source instrument (Kratos, Axis Ultra, England) operating at 14 kV and 20ma for an X-Ray power of 280 watts. Spectra were collected with a photoelectron take off angle of 90°, energy steps of 0.15 eV, and a pass energy of 40 eV for all atoms except for sulfur, which used a pass energy of 20 eV.[34] The spectra were collected on at least 7 separate locations of the same sample and reproduced with similar results for 3 different samples at each processing step. This was done to minimize both the reduction of copper[7,8] before analysis and minimize beam damage to the monolayer. For each type of sample, irradiation power-time studies were done to determine the damage characteristics of the analyses. All spectra were referenced to the Au $4f_{7/2}$ binding energy at 84.0 eV.

4.2.3.4 Contact Angle

Advancing and receding contact angles were measured using a home-built video interfaced apparatus. All measurements were made with the sample at ambient conditions. A 20 μL drop of the probe liquid was dispensed onto the surface using a flat

tipped micrometer syringe (GS-1200, Gilmont Instruments, Barrington, IL). The advancing contact angle was measured as the drop expanded. The drop was then partially retracted into the syringe and the receding angle measured. Images of the drop were captured digitally using a CCD camera and contact angles were analyzed using ImageJ 1.32j software (National Institutes of Health, USA). Measurements were made on at least 3 separate spots for each sample with 4 samples taken for each processing step. Milli-Q® water and hexadecane were used as probe liquids. In the case of hexadecane all contact angles were always less than 15°.

4.3 Results and Discussion

4.3.1 MHA/MH Bilayer Films

4.3.1.1.1 Formation of the MHA SAM

The first step in the formation of multilayer structures is the formation of a clean, densely packed ordered monolayer of a carboxylic acid terminated SAM. We characterized the initial SAMs via IR, XPS, SWE, and contact angle to determine the cleanliness of the bare SAMs. Detailed characterization of the relevant IR modes have been presented in detail elsewhere[26-33] and are summarized for convenience in Table 4.1. In Figure 4.3 the high frequency modes are shown for the bare MHA SAM (**A** see Table 4.2.) The d^+ and d^- modes are at 2851 and 2919 cm^{-1}, respectively. Comparison of simulated and experimental spectra for the d^+ and d^- modes, shown in Figure 4.3A, yielded the best fit for an all-trans structure with an average chain tilt (θ) of 33±3˚ from surface normal and a twist (Ψ) of 52±3˚.[35] This analysis agrees with previous work.[5]

Table 4.1 Selected Infrared Mode Assignments for Alkanethiolate and Mercaptoalkanoic Acid SAMs

Frequency (cm^{-1})	Mode assignments
3300-2500	–OH stretch
~2918	$–CH_2–$ antisymmetric C–H stretch (d^-)
~2850	$–CH_2–$ symmetric C–H stretch (d^+)
~2700-2500	–OH– carboxylic acid stretch
~2220	$–CD_3–$ methyl antisymmetric C-D stretch (r_a^-)
~2194	$–CD_2–$ methylene antisymmetric C-D stretch (d^-)
~2156	$–CD_3–$ methyl antisymmetric C-D stretch (r_b^-)
~2090	$–CD_2–$ methylene antisymmetric C-D stretch (d^+)
~2073	$–CD_3–$ methyl symmetric C-D stretch (r^+)
~1741	$–CO_2H–$ C=O non-hydrogen bonded stretch
~1718	$–CO_2H–$ C=O hydrogen bonded stretch
~1695-1540	Copper carboxylate symmetric C=O stretch
~1450-1335	Copper carboxylate antisymmetric C=O stretch
~1471	$–CH_2–$ scissor deformations (δ)
~1412	$–CH_2–$ scissor deformations (a)
~1100	$–ClO_4^-–$ symmetric stretch
~945	$–ClO_4^-–$ antisymmetric stretch

Inspection of the lower IR frequencies reveal a doublet at 1742 and 1717 cm^{-1} (Figure 4.4A) the peaks are the non-hydrogen bonding and hydrogen bonding carboxylic acid stretches, respectively. Also, the CH_2 scissor modes can also be seen at 1469 and 1411 cm^{-1}. A critical step in the formation of reproducible multilayer results is the cleaning of the bare monolayer with a weak HCl solution. A surface that has not been cleaned properly will show contamination most easily observed in the carbonyl stretching regions of the IR spectra in the evidenced by a decrease in the intensity of the carboxylic acid

Table 4.2 Explanation of figure and table abbreviations used for each step of the multilayer films growth. a) prime notation used to indicate systems constructed with monolayers of MPA, such as **A'** for a bare monolayer of MPA.

sample	abbreviation
monolayer of MHA [a]	**A**
monolayer of MHA + Cu^{2+}	**B**
bilayer of MHA|MH	**C**
bilayer of MHA|MH + Cu^{2+}	**D**
bilayer of MHA|MH + Cu^{2+} + MH	**E**
bilayer of MHA|MHA	**F**
bilayer of MHA|MHA + Cu^{2+}	**G**
bilayer of MHA|MHA + Cu^{2+} + MH	**H**

modes and added presence of carboxylate peaks (Figure 4.4.) Without the dilute acid rinse amounts of physisorbed material on the surface of the MHA SAM will impede the addition of copper to the surface, thus reducing the reactive sites available. The removal of this contamination was found to produce a significant improvement in the reproducibility of our results. Another good indicator of cleanliness is the advancing and receding contact angles of H2O as clean carboxylic acid terminated samples should be completely wetting with advancing (θ_{adv}) and receding (θ_{rec}) water contact angles <10˚, see Table 4.3A. [6,7,36] While multilayer surfaces are able to be fabricated after very short thiol solution depositions (~1hr), our results found that extended depositions of 12 to 24 hours resulted in more conformationally ordered monolayers, observed by the IR

Table 4.3 Thickness and contact angle measurements for bilayers of MHA|MH (A-E) and MPA|MH (A'-E') for each step of their respective MH bilayer growth.

Sample	Thickness	Θadv	Θrec
A	20±1	<10˚	<10
B	21±1	22˚±3˚	<10
C	39±1	83˚±7˚	33˚±4˚
D	34±1	72˚±9˚	27˚±3˚
E	42±1	84˚±2	37˚±3˚
A'	19±1	<10˚	<10
B'	20±1	21˚±6˚	<10
C'	39±2	84˚±7˚	25˚±5˚
D'	35±2	62˚±4˚	<15
E'	42±2	83˚±7˚	35˚±9˚

peak positions of the d^+ and d^- modes.[31] This higher ordering is indicative of a higher packing density on the surface. This is beneficial to the formation of MRFs since it should lead to a higher adlayer density since there are more reactive surface sites for copper addition.

4.3.1.1.2 Formation of the MPA SAM

In order to explore the odd-even chain length effects on the construction of multilayer films[17-19] SAMs of MPA were used which allowed a comparison of 15 and 16 carbon atom chains. The pure MPA films were found to be 19 Å thick and completely wetting measured by contact angle, see Table 4.3. IR studies of pure monolayers of the MPA surface confirmed that it also forms an ordered monolayer with all-trans alkane chains with similar orientations. Best fit IR simulations yield an average chain tilt of 32±3˚

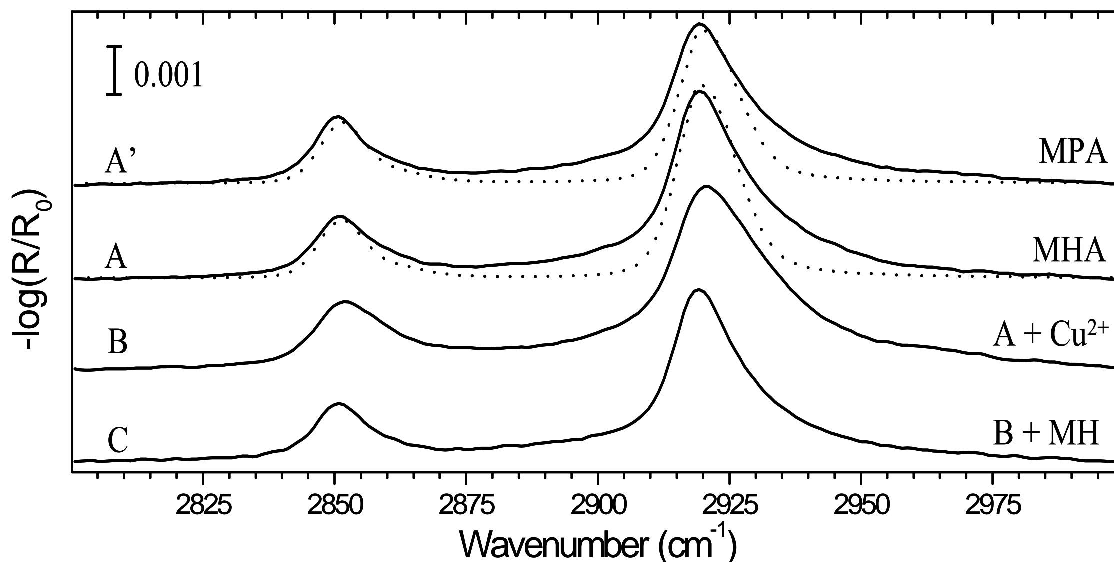

Figure 4.3. Infrared spectra of the C-H stretching modes for stages **A**-**C** of growth of a bilayer film. Infrared spectra of the **MHA**-Au SAM (A): experiment (—), simulated spectrum (···). The best fit simulation (shown) yields an average chain tilt (θ) of 33±3° from surface normal and twists (Ψ) of 52±3°. Infrared spectra of the **MPA**-Au SAM (A’): experiment (—), simulated spectrum (···). The best fit simulation (shown) yields an average chain tilt (θ) of 32±3° from surface normal and twists (Ψ) of 49±3°. The addition of the Cu^{2+} ions (**B**) causes a slight disordering of the alkane chains observed in both the d^+ and d^- modes as a +2 cm^{-1} shift relative to the bare monolayer (**A**) . The addition of a thiol adlayer causes a shift back to the original frequency (**C**).

from surface normal and twists of 49±3° for monolayers of MPA, very similar to that found for MHA (Figure 4.4.) The all-trans structure will lead to different orientations of the carboxylic acid terminal group of the monolayer (Figure 4.5.) Evidence of this can be seen easily in the IR spectra of the two bare monolayers (Figure 4.4A and 4A') the carboxylic acid regions of MHA (**A**) have a higher portion of hydrogen bonding C=O stretch than monolayers of MPA (**A'**). Monolayers of MHA have more hydrogen bonding between each other presumably due to the orientation of the carboxylic acid groups being parallel to the surface of the gold providing more sites for hydrogen bonding than monolayers of MPA which are oriented at an angle to the surface. Both monolayers were found to organize best after ~24 hour deposition times, showing higher conformational ordering measured by IR.[31] However monolayers of MPA usually needed to be cleaned more thoroughly and were more difficult to keep clean. This was found to cause significant variations in the reproducibility of multilayers formed on MPA when longer solution times were used, for example larger variations in the total thickness of multilayers of ±5 Å instead of ±2 Å. Impurities at the interfacial layers formed more easily on the odd oriented chains reducing the number of available sites for adlayers of thiols to form on the surface (see Figure 4.4.) By using short deposition times of 10-30 minutes for the adlayers, the effects of these impurities was significantly reduced and the resultant IR and XPS results were found to be both very similar and highly reproducible. For example, the molecular orientation of the adlayer films of MH was found to be identical to each other within experimental error.

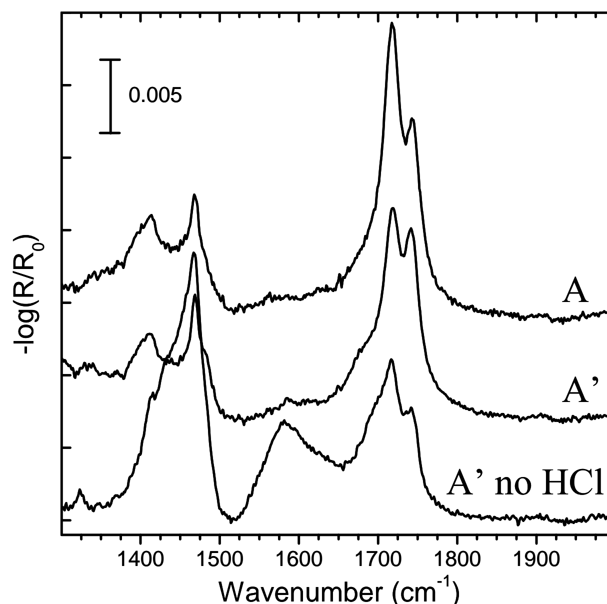

Figure 4.4. Infrared spectra of the carbonyl stretches for a MHA-Au SAM (**A**) and a MPA-Au SAM (**A'**). The ratio between hydrogen bonding (~1718 cm-1) and non hydrogen bonding (~1741 cm-1) stretching indicates a change in the orientation of the carboxylic acid head groups of the two molecules. (**A' no HCl**) An example of an uncleaned MPA-Au SAM, the surface has lower intensity carboxylic acid carboxylate peaks than a pure clean MPA surface (A) along with the presence of carboxylate peaks.

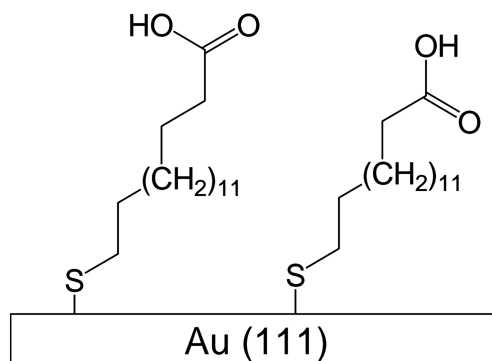

Figure 4.5. Odd-even effect of an all-trans alkane chains causes a different orientation in the carboxylic acid terminal groups.

4.3.1.2 Formation of the MHA-Cu^{+2} coordinated surface

To form a copper coordinated surface the cleaned MHA SAMs were placed in a 5 mM Cu(II) perchlorate solution in ethanol for varying times from 5-180 seconds to determine how long the coordination would take to complete. We found that 30 s is enough time to completely react the carboxylic groups on the surface, as observed by IR and XPS. However, no adverse effects were found at this stage when using longer soak times. After the initial soak the SWE thickness of the film (see Table 4.3) increases by ~1 Å to 21±1 Å (modeling as Cu^{2+} addition with n ~ 2.0.)[23] Reaction of the MHA SAM with the Cu^{2+} ion results in the disappearance of the two carboxylic acid stretching modes, see Figure 4.6B, and the formation of carboxylate species symmetric and antisymmetric stretches, observed at 1603 and 1444 cm^{-1} respectively. The CH_2 scissor modes can also be seen as shoulders on the copper carboxylate antisymmetric stretch. The ClO_4^- stretches which are normally intense features at 1100 and 945 cm^{-1} were not present in any of the IR spectra confirming its removal from the surface either into the Cu^{2+} solvent or during the ethanol rinses. This was supported by the lack of any Cl 2p XPS core level features.

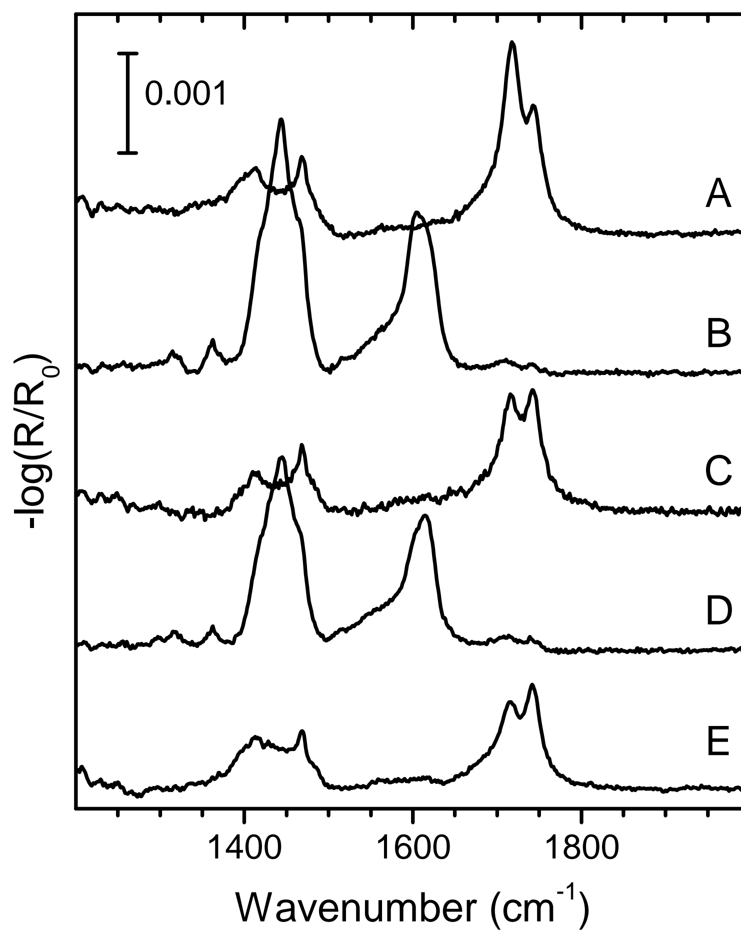

Figure 4.6. Infrared spectra of the lower frequency region for stages **A**-**E** of growth for a bilayer film detailing the changes to the carboxylic acid functional group during the growth of a MHA|MH bilayer.

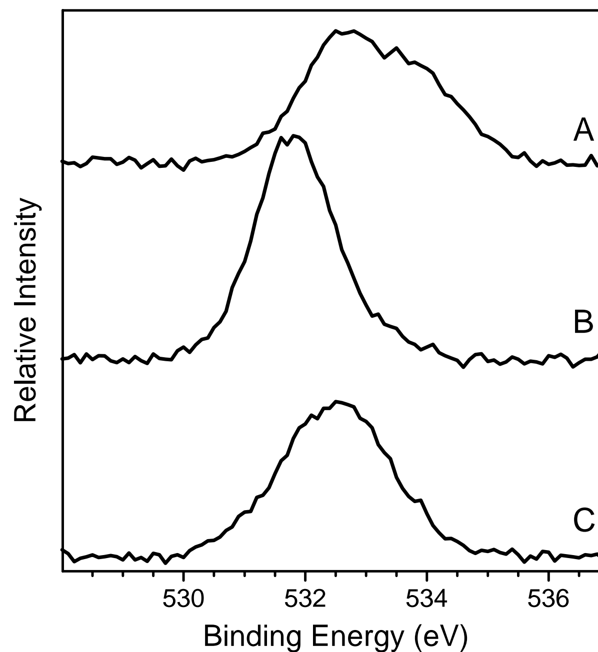

Figure 4.7. The O 1s XPS spectra for stages **A**-**C** of growth for a bilayer film. The bare monolayer (**A**) displays a doublet at 532.6 and 534.0 eV from the two oxygen atoms on the carboxylic acid. The addition of the Cu2+ ions to the carboxylic acid (**B**) forms carboxylate ions in which the oxygen atoms are chemically equivalent and form a singlet at 531.8 eV. (**C**) The addition of a MH adlayer leaves a broad peak at 532.5 eV indicating that the interface has a mix of both the carboxylic acid and the carboxylate functional groups.

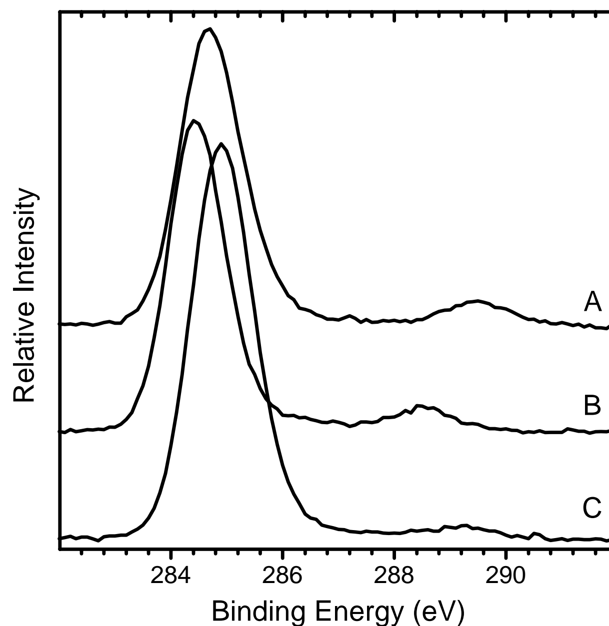

Figure 4.8. The C 1s XPS spectra for stages **A-C** of growth for a bilayer film.

Further experimental evidence of a copper reaction to the carboxylate groups on the surface is seen in the XPS spectra of the MHA and copper coordinated surfaces. The O 1s XPS spectra for the MHA SAM (Figure 4.7A) displays a doublet at 532.6 and 534.0 eV, formed by the two different oxygen species in the -CO_2H terminal group. After reacting with the copper causes the two oxygen atoms appear to become chemically equivalent and form a singlet at 531.8 eV, Figure 4.7B. Figure 4.9B shows the XPS of the Cu $2p_{3/2}$ region once the copper is added to the surface (the bare MHA monolayer shows no copper.) The spectra has regions indicative of both the Cu(II) (934.7 eV with satellite

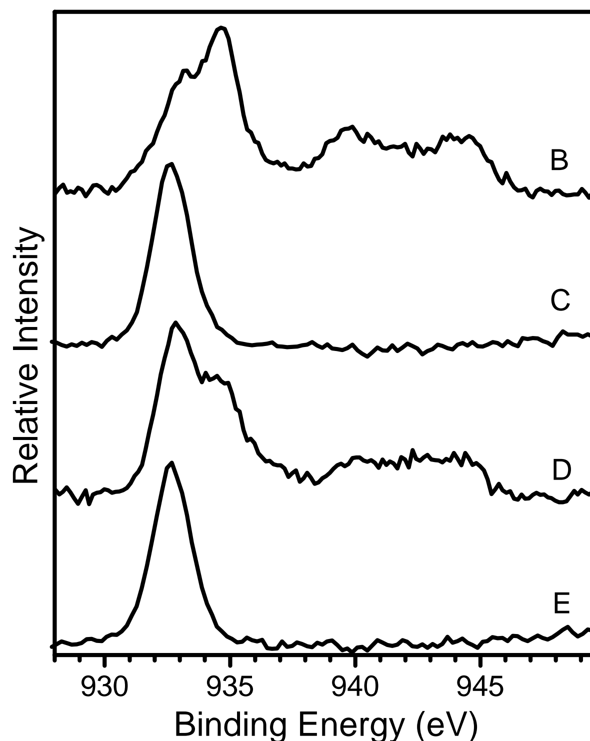

Figure 4.9. The Cu 2p 3/2 XPS spectra for stages **B-E** of growth for a bilayer film.

peaks at 940 and 944 eV)and Cu(I) (932.8 eV) oxidation states. Previous reports[7,8] indicate the Cu(II) ions on the surface can be reduced to their Cu(I) state upon exposure to the X-Ray beam. This is easily observed experimentally by varying the XPS beam irradiation time, the ratio of Cu(II) to Cu(I) changes dramatically with longer exposures resulting in higher amounts of Cu(I) observed. This agrees with the previous experiments[7,8] on similar surfaces that the copper found on the surface is initially in the Cu(II) state. Figures 9A and 9B show that the S 2p spectra do not change upon the

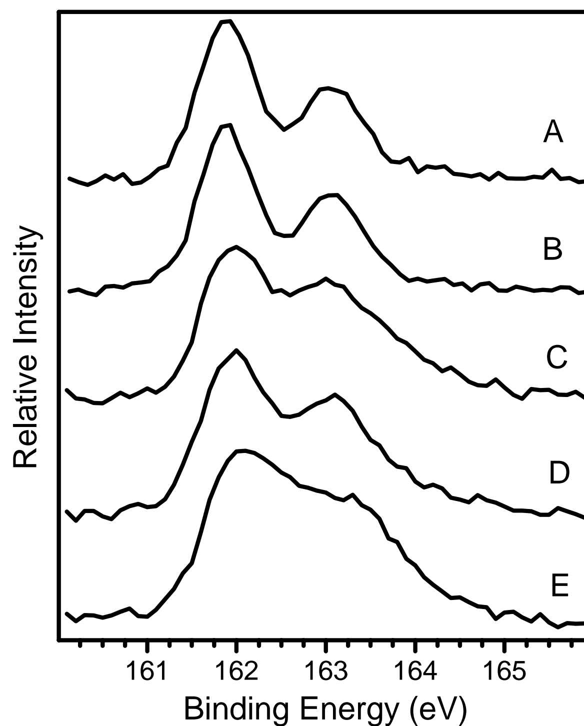

Figure 4.10. The S 2p XPS spectra for stages **A-E** of growth for a bilayer film.

formation of a Cu complex on the MHA SAM. Both of these spectra can be fit with two peaks at 161.9 and 163.1 eV, in agreement with previous reports of sulfur bound to gold surfaces.[37]

The IR and XPS reveal a complete disappearance of the carboxylic acid components and indicates their conversion to a carboxylate species. The data indicate that the carboxylate species is formed by the following metathesis reaction with the copper ions in solution:

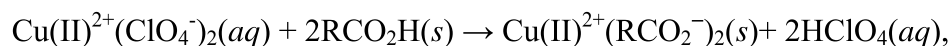

$$Cu(II)^{2+}(ClO_4^-)_2(aq) + 2RCO_2H(s) \rightarrow Cu(II)^{2+}(RCO_2^-)_2(s) + 2HClO_4(aq),$$

where, R ≡ $-S(CH_2)_{15}-$, *aq* = aqueous, *s* = surface.

An ancillary effect of this reaction can be seen in the high frequency IR spectra (Figure 4.3B) which shows that after reacting with the Cu^{2+} ions in solution the d^+ and d^- modes shift, by +2 and +1 cm^{-1} to slightly higher wavenumbers 2852 and 2921 cm^{-1} respectively. This shift indicates a slightly less organized monolayer than in the initial MHA SAM.[31] This disordering is believed to be caused by the interaction of the two different CO_2^- groups attached to one Cu^{2+} ion. As the carboxylic acid groups are pushed apart by electronic repulsion forces slight kinks in the CH_2 backbone chain will be formed. Another effect of this reaction can be observed in the C 1s XPS spectra, Figure 4.8. The bare MHA monolayer (Figure 4.8A) has two C 1s peaks, one for the main chain at 284.7 eV and another for the carboxylic acid component at 289.4 eV. The addition of the copper ions (Figure 4.8B) causes both peaks to shift to slightly lower binding energies, the main chain by 0.3 eV and the carboxylic acid component by 0.9 eV. These shifts have been previously reported on similar surfaces and were attributed to surface charging. [6,7,38]

4.3.1.3 Formation of a MHA|MH bilayer film

The next step in the formation of a bilayer structure is the addition of MH. The copper coordinated samples were placed in ~5 mM MH solutions in ethanol for varying times ranging from 10 minutes to 24 hours, the results given in this section are for a 30 min solution deposition time unless otherwise stated. The addition causes an increase in the thickness of the samples by ~18 Å for a total of ~39±1 Å, and yields water contact angle

values of 83±7° (θ_{adv}) and 33±4° (θ_{rec}) (see Table 4.3 for SWE and CA results). The 50° hysteresis suggests a much lower packing density than a full bare monolayer of MH on gold (8°), and a higher number of surface defects in the MH adlayer.[39] Previous studies of an n-octadecylsiloxane monolayer with uniform 50% coverage assembled on a hydrophilic surface had slightly higher advancing water contact angles around 95°.[40] Suggesting that the MH adlayers have a coverage less than 50% or that the adlayer might be organized differently.

Results of the adlayer interface chemistry can be seen in the XPS spectra very clearly. The O 1s spectra (Figure 4.7C) changes from a sharp feature, at 531.8 eV, to a relatively broad feature at 532.5 eV after adlayer formation. This peak seems to have components from both the CO_2H and CO_2^- oxygen species. The C 1s spectra (Figure 4.8C) shows the carboxylic acid component peak, it is also broad at 288.9 eV relative to the widths of the CO_2H and CO_2^- carbons observed in the two previous surfaces, indicating a possible combination of the free acid, 289.4 eV, and the carboxylate ion, 288.5 eV. The relative intensity of the carboxylic acid component of the bilayer is much lower than in the unreacted and Cu^{2+}-SAM films, this effect is presumably due to adlayer atoms screening photoelectrons from underneath and to a higher number of equivalent alkane carbons in the main peak. The Cu $2p_{3/2}$ XPS region (Figure 4.9C) shows a single peak, at 932.8 eV, which is indicative of either elemental or Cu (I) species. However, the Cu LMM Auger line at 916 eV indicates that the copper species are in a Cu(I) state,[34] in agreement with previous work.[8] The S 2p spectra (Figure 4.10C) changes dramatically upon adlayer formation as evidenced by the change from 2 distinct peaks to a single triangularly shaped peak. This line shape is the result of two different sulfur species being present on

the surface, one for the Au-S at 161.9±0.1 eV and another for a Cu-S species at 162.4±0.1 eV.[41] While XPS results confirm the reduction of the copper and the presence of both carboxylic acid and carboxylate ions at the interface it also gives an estimation of the relative coverage of the two layers by way of the S 2p spectra. By peak fitting[42] and accounting for photoelectron mean free path[37,43,44] effects, the S 2p spectra gives a 0.4:1 (±0.1) Cu-S to Au-S ratio between the two different sulfur peak areas. This ratio is indicative of a ~50% adlayer coverage on the surface of the MHA underlayer, with a 1 to 1 ratio between the Cu(I) ions and the adlayer molecules. A schematic of this structure is shown in Figure 4.11.

The IR samples were modified with a deuterated adlayer in order to easily distinguish between the initial monolayer and the adlayer. The mid frequency IR is shown in Figure 4.12 revealing the C-D stretches from the adlayer. The d^+ and d^- modes for the C-D stretches are at 2092 and 2194 cm^{-1} respectively. Interestingly these values are very close to that found for a deuterated MH monolayer on Au {111}, 2090 and 2194 cm^{-1} for the d^+ and d^- modes respectively,[45] indicating that adlayer has a similar degree of conformational order to the bare MHA monolayer.[31] Using a thickness of 18 Å (Table 4.3) the best fit IR simulations (Figure 4.12) of the spectra yields an average chain tilt of 41±3˚ from surface normal and twists of 41±3˚ for the deuterated adlayer. The tilt and thickness of the adlayer molecules are consistent with the molecule's physical length.[46] This tilt is significantly higher than that of a MH monolayer on gold[26], implying a lower packing density of the adlayer. The low frequency IR (Figure 4.6C) shows the

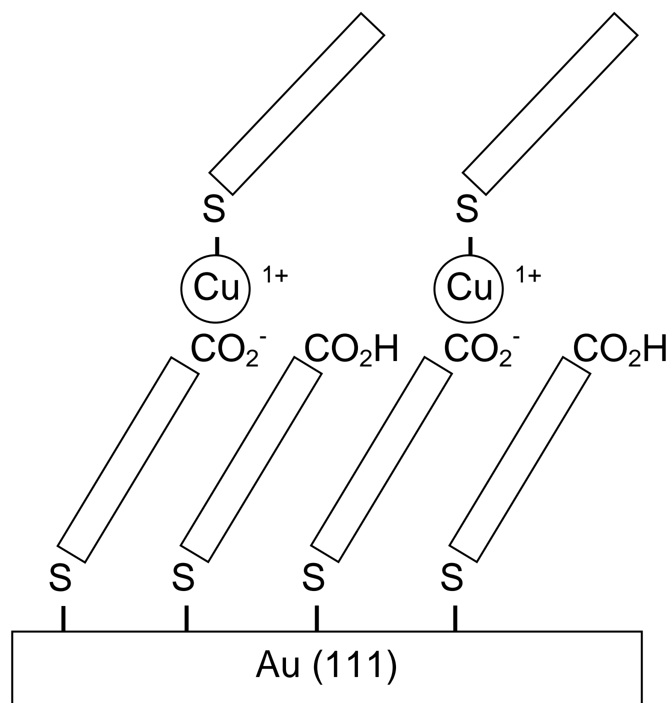

Figure 4.11. Schematic of MH bilayer on an α,ω-mercaptoalkanioc acid/Au SAM.

carboxylate stretches diminish completely while the carboxylic acid stretches reappear, though not as ntense as in the bare monolayer. A close inspection of the carboxylic acid stretches reveals that the ratio of hydrogen bonded C=O to nonbonded C=O is reduced when compared to the bare monolayer. These changes relative to the bare MHA monolayer may be due to the heterogeneous nature of the underlayer where the reduction of the copper produces a surface with both CO_2^- groups and CO_2H groups leaving fewer neighboring groups on the surface for hydrogen bonding.

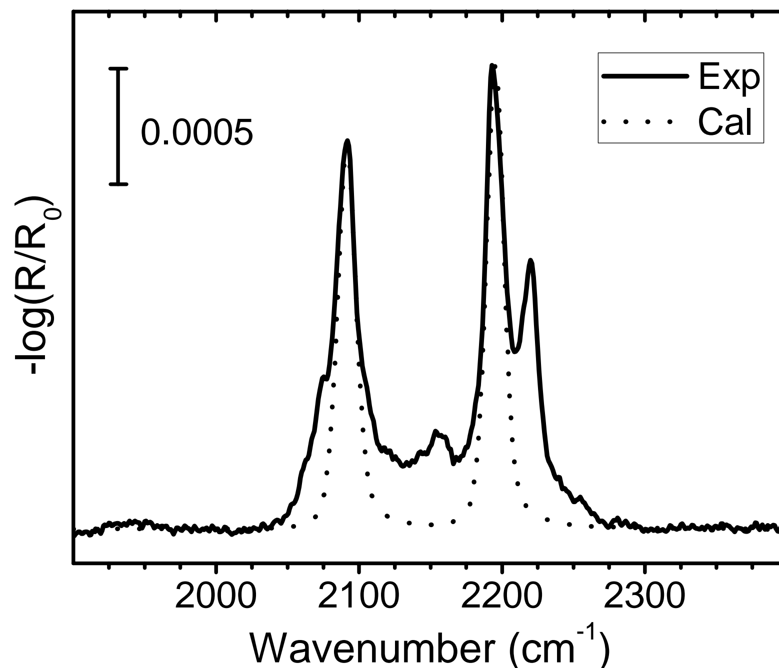

Figure 4.12. Infrared spectra of the C-D stretches of a deuterated MH adlayer in a MHA|MH-Au sample: experiment (—), simulated spectrum (···). The calculated spectra yields an average chain tilt of 41±3˚ from surface normal and twists of 41±3˚.

The XPS and IR data points to a reduction of the Cu (II) to Cu (I) by the thiol group on the MH adlayer. The reduction in turn liberates the thiol proton which is then used to balance the carboxylate anion charge, thereby forming a carboxylic acid group. This reaction scheme indicates that the resulting surface can not have an adlayer coverage greater than 50% of the underlying carboxylic acid monolayer, as seen in Figure 4.11.

This is in agreement with a 1/1 ratio of CO_2^- to CO_2H groups at the interface of the two layers (R'=$HSC_{16}H_{33}$).

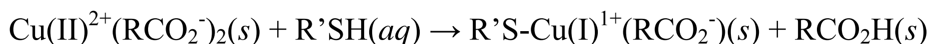

$$Cu(II)^{2+}(RCO_2^-)_2(s) + R'SH(aq) \rightarrow R'S\text{-}Cu(I)^{1+}(RCO_2^-)(s) + RCO_2H(s)$$

where, R ≡ $-S(CH_2)_{15}-$, *aq* = aqueous, *s* = surface.

An IR inspection of the MHA layer's C-H stretches (Figure 4.3C) reveal a shift to the slightly lower wavenumbers 2851 and 2919 cm^{-1} respectively, indicating that the carboxylic acid monolayer is as ordered as the initial samples. This increase in conformational order, relative to the copper complexed surface, is caused by the reaction of the thiol with the copper ions. The bending of the alkane chains to allow two different carboxylate groups to interact with the copper is no longer existent, since the copper ions have been reduced they each only interact with one carboxylate group. The reduction of the copper by the thiol releases a hydrogen ion at the interface, this hydrogen then reacts with a neighboring carboxylate group forming a carboxylic acid. The protonation of the carboxylate group reduces ionic interactions between the terminal groups. This reduction in coulombic interaction at the headgroup allows the alkyl chains to reorder and adopt their original unreacted orientation.

With longer solution deposition periods, (30+ min) insertion of deuterated MH into the carboxylic acid layer will cause the intensity of the C-H stretches to decrease.[47] This insertion and exchange causes significant problems to our bilayer model system since the new underlayer has less reactive sites for the copper reduction available. To minimize insertion we used very short solution depositions, thirty minutes was found to be enough to completely reduce the copper, observed via IR and XPS.

4.3.1.4 Readdition of copper and MH to densify the bilayer film

4.3.1.4.1 Addition of Cu^{2+} to the MHA|MH bilayer film

Further experiments were performed in order to explore the proposed mechanism and the character of the copper interface between the two monolayers. Since our data show that this interface has a significant fraction (~ 50%) of $–CO_2H$ groups present, it should be possible to attach additional adlayer molecules and create a denser adlayer by coordinated copper ions to these 'free' carboxylic acid groups. This was done by placing the samples in a 5 mM Cu(II) perchlorate solution in ethanol for varying times from 5-180 s, the data given here is for 30s unless otherwise mentioned. Evidence of a reaction with the carboxylic acid groups can be seen in both the O 1s and C 1s XPS spectra. The O 1s XPS peak sharpens and shifts to 532.0 eV while the carboxylic acid component of the C 1s spectra shifts to 288.6 eV, the results suggest that a copper carboxylate complex is formed again since to the peak positions are similar to those after the initial addition of the Cu^{2+} ions. This is also evidenced in the low frequency IR (Figure 4.6D) by the carboxylic acid stretches diminishing,[48] while the carboxylate stretches gain in intensity. The $Cu_{2p\ 3/2}$ XPS (Figure 4.9D) shows species indicative of both the Cu(II) (934.7 eV with satellite peaks at 940 and 944 eV) and Cu(I) (932.8 eV) chemical state. It differs significantly from the initial adsorption of copper ions in that more of the Cu(I) chemical state is present (see Figure 4.9B). This is due to the presence of Cu(I) bonded to the adlayer before the second addition of Cu(II) ions. The IR in combination with the XPS provides evidence for the complete oxidation of the carboxylic acid groups on the surface with a combination of Cu(I) and Cu(II) carboxylates. Also, the C-H d^- mode shifts to a slightly higher wavenumber, +1 cm^{-1}, though not as far as initial addition of Cu^{2+} ions to

2920 cm^{-1}. This lower shift can be explained in the same manner as in the initial coordination of Cu^{2+} ions. In this case, however, there are fewer COOH terminal groups at the interface available and thus a smaller frequency shift is expected due to the smaller portion of kinked chains on the surface. The IR and XPS results indicate that readdition of the Cu^{2+} ions again causes the same metathesis reaction on the interface carboxylic acids as the initial addition, where the carboxylic acid groups are ionized to form copper carboxylates.

After the Cu^{2+} addition to the MHA|MH bilayer a loss of material is observed by a decrease in film thickness as measured by SWE (Table 4.3). Additionally, a lower packing density and an increase in surface defects are measured by a higher hysteresis in the contact angle contact angle (Table 4.3). The loss is also evidenced in the C 1s XPS spectra, after the readdition of the Cu the C 1s signal will decrease in intensity, though it does not indicate which layer the loss occurs in. IR spectra in conjunction with the sulfur XPS data can be used to determine which layers on the surface lose material. A loss of intensity of the C-D IR stretches (Figure 4.13D) indicates significant loss of material from the deuterated adlayer. While the C-H stretching intensities are not significantly perturbed indicating that this layer is not affected. This loss of adlayer material can also be seen in the S 2p XPS spectra, Figure 4.10. While both sulfur species are present their intensity ratio changes. The spectra shown is for a 2 minute immersion time, the ratio between Cu-S and Au-S is reduced to 0.3±0.1:1 indicating a loss of the adlayer material relative to before the addition of the copper to the MHA|MH surface (see Figure 4.10Dand 10C).

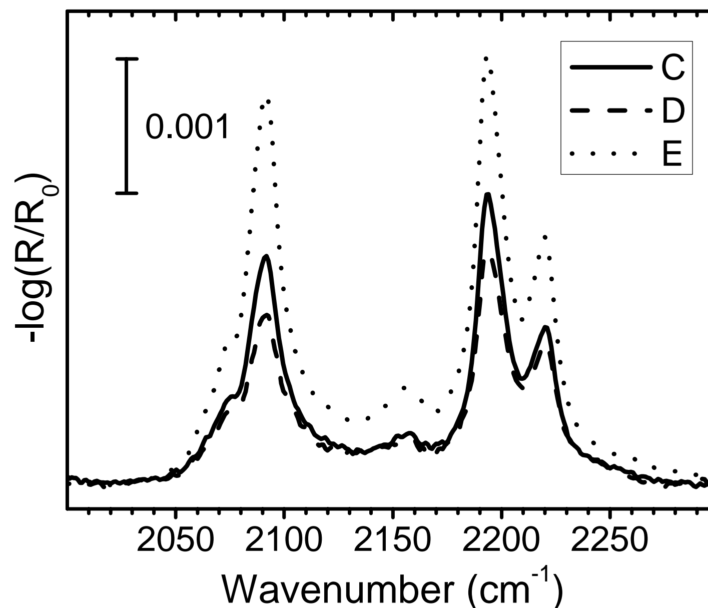

Figure 4.13. Infrared spectra of the C-D stretching modes for the C-E stages of growth of a bilayer film.

The data suggest that a second metathesis reaction occurs with the ClO_4^- ions exchanging with the COO^- ions and the resulting ClO_4^- $Cu(I)^+$-SR complexes dissociating from the surface:

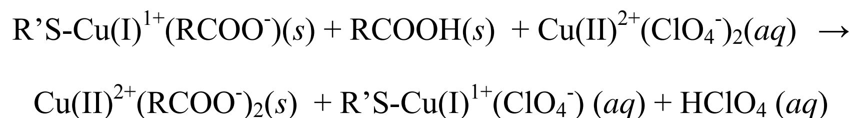

$$\text{R'S-Cu(I)}^{1+}(\text{RCOO}^-)(s) + \text{RCOOH}(s) + \text{Cu(II)}^{2+}(\text{ClO}_4^-)_2(aq) \rightarrow$$

$$\text{Cu(II)}^{2+}(\text{RCOO}^-)_2(s) + \text{R'S-Cu(I)}^{1+}(\text{ClO}_4^-)(aq) + \text{HClO}_4(aq)$$

where, R ≡ $-S(CH_2)_{15}-$, R' ≡ $-(CH_2)_{14}CH_3$, *aq* = aqueous, *s* = surface.

The reaction would result in a loss of material from the adlayer of the surface. The amount of loss was found to vary significantly with time, we found that ~30 seconds was enough time to repeatably ionize all the carboxylic acid groups on the surface, measured

by IR and XPS. Longer deposition times resulted in a greater loss of material from the adlayer and in larger variations in the adlayer quality/reproducibility. Similar reactions to this can be used to remove the adlayer more completely such as immersion in an dilute HCl solution.[47] In this case there is a significant amount of material lost after 30 s of immersion in a copper perchlorate solution, the thickness of the film lowers by ~2 Å (Table 4.3), with longer copper solution rinse duration, losses of 5-7 Å were common.

4.3.1.4.2 Readdition of MH to a MHA|MH bilayer film

The samples were then placed in ~5 mM MH solutions in ethanol for varying times ranging from 10 minutes to 24 hours to attempt to denisfy the adlayer by reacting the MH thiol groups with the added Cu(II) ions on the surface. The results presented in this section are for a 30 min solution deposition time unless otherwise stated. The thickness of the bilayer structure increases by 4 Å to a total of ~42±1 Å, (Table 4.3.) The water advancing contact angle (Table 4.3) increases slightly to 84±2°, also the hysteresis is slightly reduced (47˚ vs 50˚) indicating a slightly higher packing density than of the previous MHA|MH surface.[39] The low frequency IR (Figure 4.6E), shows the carboxylate stretches diminish completely while the carboxylic acid stretches reappear, though not as intense as in the bare monolayer. Similar to the original MH adlayer addition, the ratio of hydrogen bonded to non-hydrogen bonded species shifts, indicating a lower amount of non-hydrogen bonded species relative to both the MHA and original MHA|MH bilayer surfaces. This is also evidenced by the O 1s and C 1s XPS, the peaks shift to energies similar to those observed after the initial addition of the MH viz, 532.4 and 288.9 eV respectively. Indicating that this surface also has interface with a mix of carboxylate and carboxylic acid components between the two layers. The Cu $2p_{3/2}$ XPS

region (Figure 4.9E) shows a single peak at 932.8 eV, indicative of the Cu(I) species. As before the C-H d^+ and d^- stretches shift back to their original value 2919 and 2851 cm^{-1} respectively, as the chains 'unkink' from one another. With longer solution deposition times, 2 to 24 hours, a small shoulder peak at ~2962 cm^{-1} is observed indicating protonated CH_3 groups present on the surface due to the adsorption of organic materials on the surface, most likely ethanol. The XPS data points to a reduction of the Cu(II) to Cu(I) and a protonation of carboxylate groups to carboxylic acid. This reaction is presumably the same reaction observed in the initial MH addition to a Cu(II) coordinated surface. However this time it results in an interface between the two layers with significantly more COO^- groups than CO_2H groups which leaves less hydrogen bonding neighbors around them. As in the original MH addition the solution deposition time was optimized at 30 minutes to allow for the complete reduction of the Cu^{2+} ions and to minimize both exchange and physisorbtion of MH and ethanol.

Evidence of more MH molecules present on the surface can be seen in the mid frequency IR, see Figure 4.13E. The IR shows a significant increase in the intensity of the C-D modes on the surface, indicating more of the deuterated MH molecules have absorbed on the surface relative to the original MHA|MH bilayer. The increase in adlayer material is also observed in the S 2p XPS spectra, Figure 4.10E. While both sulfur species are still present the ratio between the two changes.[49] The ratio between Cu-S and Au-S species increases to 0.7±0.1:1 and indicates a significant gain of the Cu-S content from that seen in the first addition of the MH, Figure 4.10C. This data indicates that the second time the MH is added the coverage of the adlayer is higher than that of the original addition.

This higher coverage of the MH adlayer on the surface, than was found in the original addition is expected, given our reaction scheme. If little to no loss of the adlayer took place in the second copper addition step then the MH coverage would remain close to the theoretical maximum of 50%. The remaining 50% of the surface is covered with Cu^{2+} ions, so the new MH molecules can form on each of the copper sites. Add that to the original MHA|MH bilayer, the total coverage may be as high as 75% of the carboxylic acid layer. Theoretically this could continue until close to uniform coverage of the adlayer is present. However, MH insertion into the MHA monolayer, ion exchange, and physisorbtion of organic residue impede this process from continuing in this model system. We have found no advantage for continuing on after the second addition of the adlayer as the surface coverage is either similar to the second addition, or deteriorations in film quality are observed.

4.3.2 MHA|MHA|MH Trilayer films

4.3.2.1 Formation of a MHA|MHA bilayer

After investigating the growth mechanism for a MH|MHA bilayer, further experiments were performed to investigate how our model and it's mechanisms apply to multilayer MHA films. Thicker trilayer films were constructed and examined using similar deposition conditions to those used in the bilayer structure. The first two steps in constructing the multilayer film are the same as in the bilayer case, the formation of a bare carboxylic acid terminated monolayer followed by a metathesis reaction with Cu^{2+} ions. The initial adlayer however is a layer of a carboxylic acid terminated thiol molecule, in this case MHA. The copper coordinated MHA surfaces were placed in ~5 mM MHA solutions in ethanol for varying times ranging from 10 minutes to 24 hours,

the results given in this section are for a 2 hour solution deposition time unless otherwise stated. The thickness increases by ~15 Å to 36±1Å, slightly thinner than that of the MHA|MH bilayer (~18 Å). Since the MHA is slightly longer than the MH molecule[50] it is unlikely that the molecular tilt of the two different adlayer molecules are the same. The IR of this bilayer structure is shown in Figure 4.14. Large amounts of OH stretching vibrations can be seen from 2500 to 3300 cm^{-1} and the shoulder peak seen at 2500 to 2700 cm^{-1}.[28] The presence of these stretches indicates an interaction between the carboxylic acid head groups and possible H_2O adsorption on the surface. These stretches are not present in the original monolayer or when a MH is used as the adlayer. The interaction between carboxylic acid groups can also be seen in the carboxylic acid stretches, Figure 4.13d, at ~1741 and 1719 cm^{-1}. The peak shape for these stretches is very different from the original monolayer in that the hydrogen bonding portion of the doublet, 1719 cm^{-1}, increases dramatically. The hydrogen bonding evidenced in all of these regions is presumed to be due to the interactions of the adlayer with itself, since we know that the hydrogen bonding at the copper interface decreases when a MH molecule forms the adlayer, see Figure 4.6C. The results from the MH bilayer experiments indicate that the adlayer density should be less than half of the first layer. This lower packing density would presumably allow adlayer chains more room to move around relative to a full monolayer on Au, thus enabling the carboxylic acid groups to interact more with one another. This interaction of the head groups on the adlayer is believed to

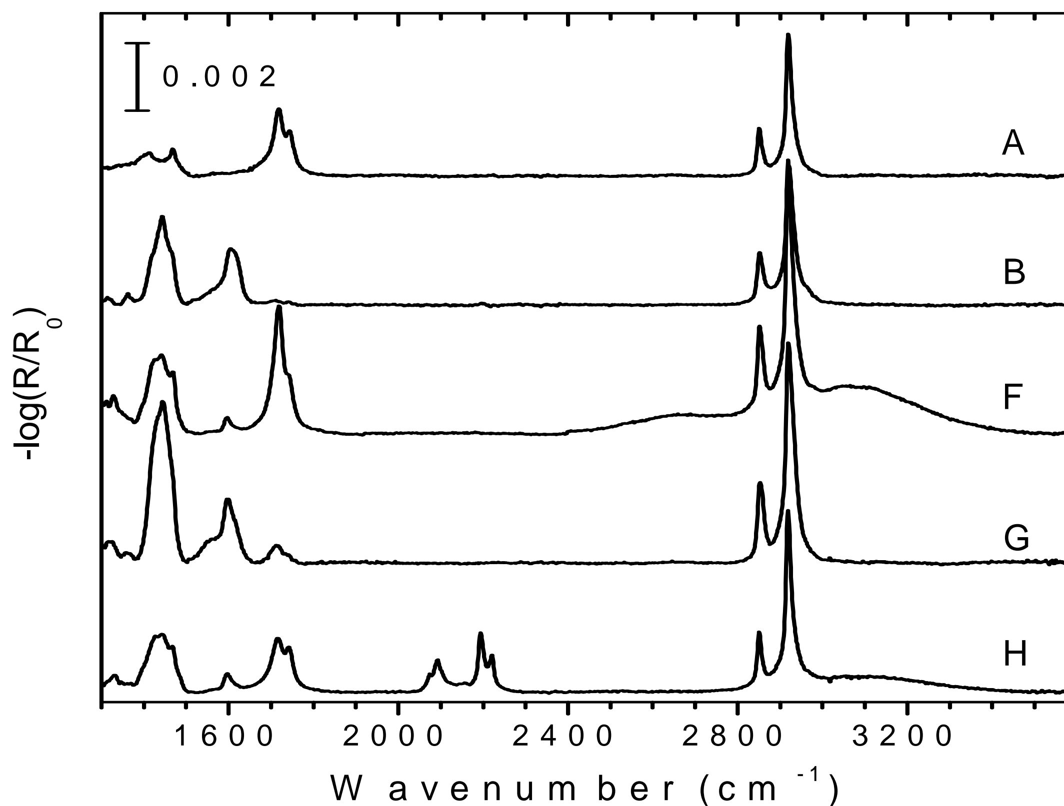

Figure 4.14. Infrared spectra for the 5 steps of growth of a trilayer film.

be the cause of the slightly lower thickness for the MHA layer than that of a MH layer, since the alkane chains are 'bending in' to enable the carboxylic head groups to interact with one another.

Further evidence of bending of the adlayer chains can be seen in the IR C-H stretching modes. Since the adlayer is protonated the –CH– d^+ and d^- modes increases in intensity at 2919 and 2852 cm^{-1}. The peak positions are a combination of both the adlayer and the

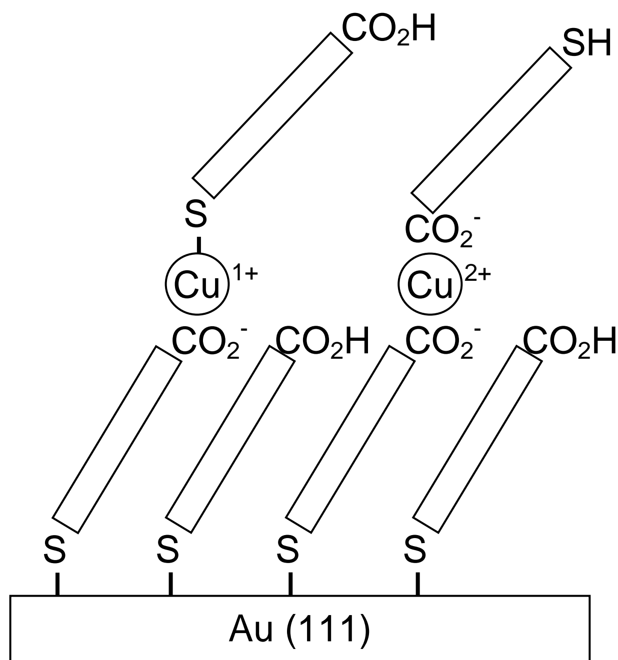

Figure 4.15. Schematic of two possible α,ω-mercaptoalkanioc orientations for a MHA bilayer on Au.

original layer. To determine the peak position of just the adlayer, the spectra for the original monolayer can be subtracted from it. This subtraction reveals peaks with higher wavenumbers of 2923 and 2855 cm^{-1}. These higher wavenumbers are indicative of less conformationally ordered alkane chains in the adlayer relative to that of the underlying MHA layer.[31]

4.3.2.2 Copper Coordination of adlayers of MHA; thiol vs. carboxylic acid

In the case of the MH adlayer there is only one possible coordination of the adlayer to the copper ions, via the thiol groups reducing the copper ions. When using carboxylic acid terminated thiols as the adlayer there is also the possibility that the adlayer carboxylic acid groups will interact with the copper ions ionically and insert into the monolayer upside down, Figure 4.15. Previous XPS results have suggested that α,ω-mercaptoalkanioc adlayers do not insert carboxylic acid group down.[6,7] However, we have found evidence that a portion of the adlayer is bound to the surface through the carboxylic acid group. Figure 4.16 shows the IR spectra of the carboxylic acid regions for the first three steps of growth for both the MH and the MHA adlayers. In the case of the MH adlayer, Figure 4.16C, the carboxylate stretches completely disappear. However, in the case of the MHA adlayer, Figure 4.16F, the carboxylate stretches, 1600 and1440 cm^{-1}, do not disappear completely.[51] While the intensity of both the symmetric and antisymmetric peaks decreases the area ratio between the two changes dramatically compared to that of the initial addition of Cu^{2+}, Figure 4.16B. Since a p-polarized infrared beam reflecting off a metal substrate excites only longitudinal optical modes[26,52] this change in relative intensity is caused by a change in the orientation of the vibration relative to the surface. When the Cu^{2+} ions are first on the surface the tilt of the carboxylic head groups causes both the symmetric and antisymmetric modes to have oriented partially in a longitudinal direction, Figure 4.17a. Conversely, if a copper ion were to complex with another carboxylic acid from solution and not bound to the gold surface the two carboxylic acid groups would arrange in a linear fashion, Figure 4.17b. If this were perpendicular to the surface the symmetric mode would be a purely longitudinal optical mode while the antisymmetric mode would be a purely transverse optical mode

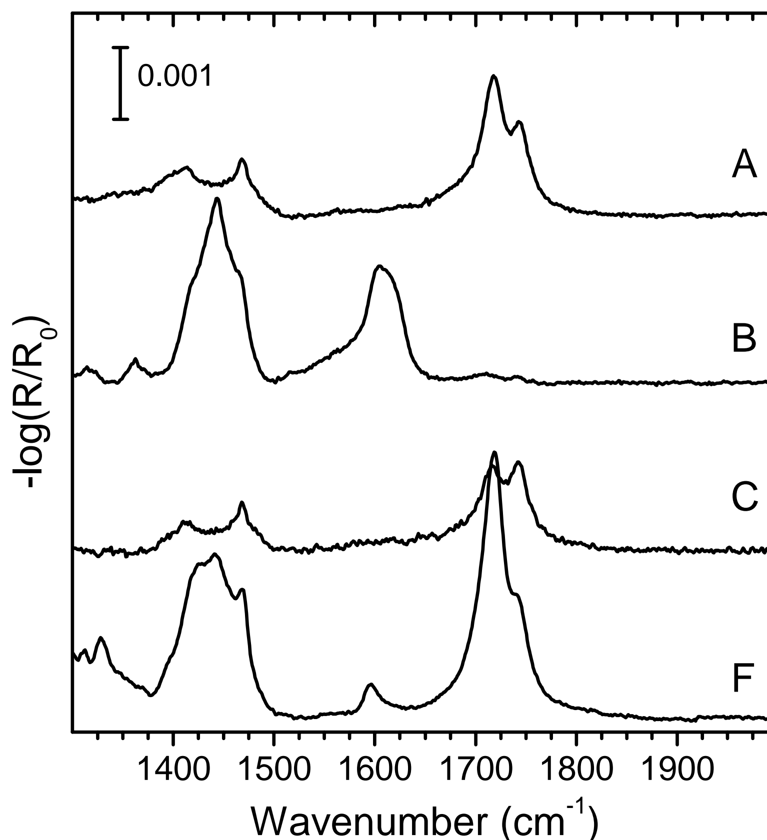

Figure 4.16. Infrared spectra for the first 3 steps of growth for both a bilayer and a trilayer film. (**A**) the bare MHA monolayer shows the carboxylic acid stretches of the monolayer, while (**B**) the Cu^{2+} coordinated MHA surface results in the complete disappearance of the carboxylic acid groups replaced by carboxylate groups. The addition of a MH adlayer to the Cu^{2+} coordinated MHA surface (**C**) results in the complete loss of both carboxylate stretches and the replacement of the carboxylic acid stretches. The addition of MHA to a Cu^{2+} coordinated MHA surface (**F**) reveals the presence of both carboxylate ions and carboxylic acid components.

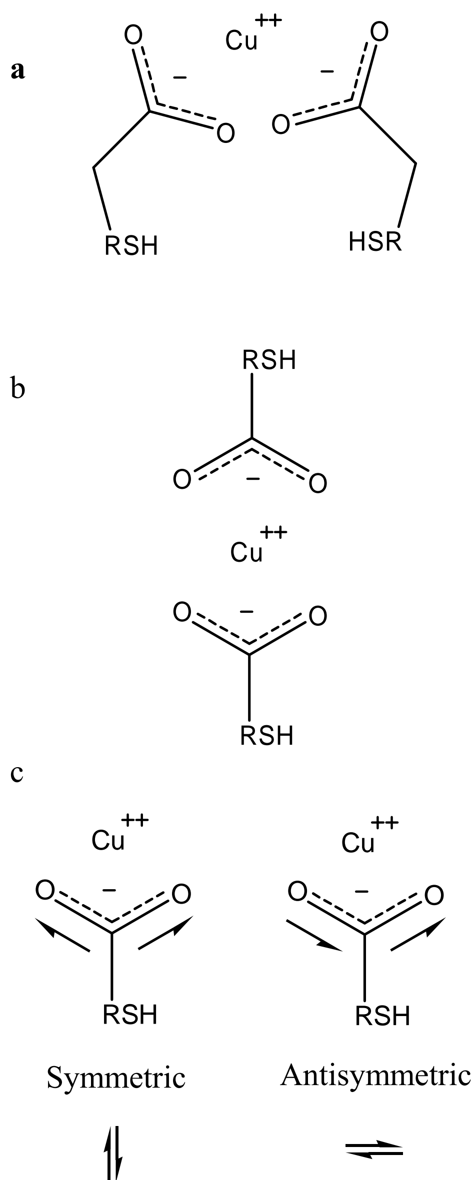

Figure 4.17. (**a**) Schematic of the orientation of the copper carboxylate complex formed on the surface after the initial addition of Cu^{2+} ions to a α,ω-mercaptoalkanioc SAM. (**b**) Schematic of the structure of the copper carboxylate complex formed if one or both species are unconstrained geometrically, i.e. bound to a surface. (c) Directions of the symmetric and antisymmetric vibrations of a carboxylate ion.

and thus not observable via our IR instrumentation. The spectra, Figure 4.16F, has a large symmetric adsorption at ~1440 cm^{-1}, and a small antisymmetric adsorption at ~1600 cm^{-1}, indicating that the complex is not oriented completely perpendicular to the surface, but instead has a slight tilt.[53] The presence of these peaks suggests that some of the adlayer is in fact oriented carboxylic acid group down.

The XPS results corroborate the orientation conclusion drawn from the IR spectra. The Cu $2p_{3/2}$ XPS spectra for the MHA bilayer structure, formed after a 30 min MHA solution immersion, can be seen in Figure 4.18F. Unlike the addition of the MH layer (Figure 4.9C) significant amounts of Cu(II) are observed. When a MHA|MH bilayer is formed the thiol group was found to reduce all of the Cu(II) ions on the surface to Cu(I). In this case some of the Cu(II) ions are not reduced, which is presumably due to the unreduced Cu(II) species forming a ionic complex with the carboxylate groups. This complex would form a physical impediment to a thiol molecule preventing it from reacting with the Cu(II) ion. This results in an interface with both Cu(I) and Cu(II) species. The mixture of orientations of the adlayer would result in three different sulfur species in the S 2p XPS spectra (Figure 4.19); Au-S at 161.9 eV, Cu-S at 162.4 eV, and a free thiol species at 163.5-164 eV.[37,41,54] Due to the proximity of the binding energies of the three species it is impossible to determine an accurate estimation of the proportion of each component. However, an approximate fit of the components can be made to identify each of the sulfur components, see Figure 4.19.[42] Importantly, the amount of adlayer coordinated via the carboxylic acid reduces with longer solution deposition times up to two hours in duration, after which no significant change is observed via IR or XPS, indicating an equilibrium of thiol and carboxylate ion species bound to the copper ions.

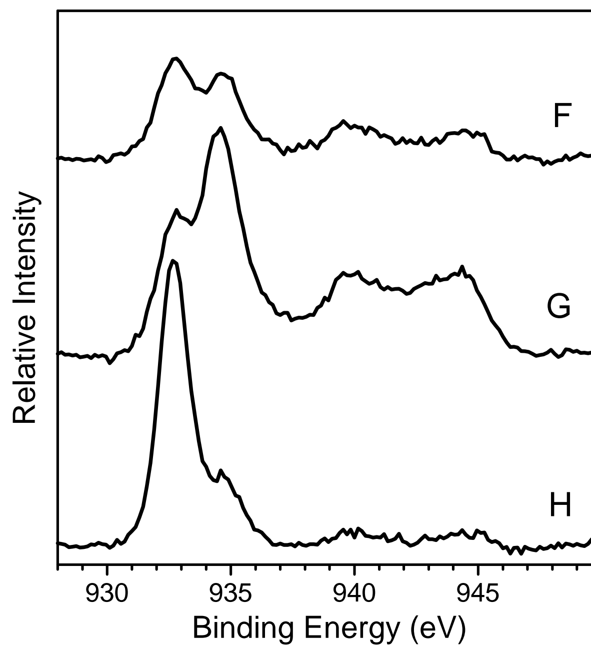

Figure 4.18. The XPS Cu 2p 3/2 region spectra for the F-H stages of growth for a trilayer film.

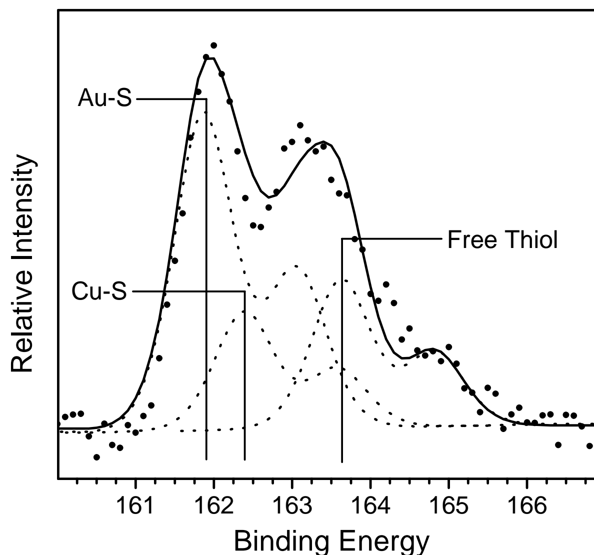

Figure 4.19. The XPS S 2p region spectra. The experimental (·····) and a fitting of the 3 different sulfur components for a bilayer of MHA, total simulated fit (——), each labeled component fit (· · ·).

4.3.2.3 Addition of Cu^{2+} to a MHA|MHA bilayer

The addition of copper to the MHA|MH samples resulted in the ionization of "free" carboxylic acid groups at the interface between the two layers and a loss of MH adlayer molecules. The MHA|MHA differs from a MHA|MH bilayer in that there are carboxylic acid groups both at the interface between the two layers and on the surface of the bilayer. Also, the MHA adlayer molecules interact with one another through hydrogen bonding. To determine what/if any effects these differences might have experiments were

performed to explore the addition of Cu(II) ions to a α,ω-mercaptoalkanoic acid multilayered surface. This was done by placing the samples in a 5 mM Cu(II) perchlorate solution in ethanol for varying times from 5-180 s, the data given here is for 30 s unless otherwise mentioned. The addition of Cu(II) ions to the surface can be clearly seen in the Cu $2p_{3/2}$ XPS spectra as a clear increase in Cu(II) signal relative to the MHA|MHA bilayer film, see Figure 4.18G and 18F. The effect on the carboxylic head groups on the surface is evident in the IR spectra. Figure 4.14G reveals a loss of the carboxylic acids –OH stretches at 2500-3300 and 2500 to 2700 cm^{-1}. The carboxylic acid carbonyl stretches, 1741 and 1718cm^{-1}, are both greatly reduced in intensity, while the symmetric and antisymmetric carboxylate stretches, 1600 and 1440cm^{-1}, increase in intensity. The carboxylic acid peaks do not however completely disappear, and longer Cu^{2+} solution deposition times (+ 30 s) did not reduce the intensity of this peak significantly, indicating that some of the groups on the surface were 'protected,' presumably by steric hindrance of the MHA adlayer molecules. As in the case of the MHA|MH bilayer, the second addition of copper was found to correspond to a loss of material in the adlayer. Evidence of this loss of material is observed via a reduction of intensity of–CH_2– d^+ and d^- modes in the IR and in the reduction of carbon signal in the C 1s XPS spectra. However, the thickness of the sample increases by ~1 Å to 37±2Å. The overall increase in thickness of the samples is presumably due to a balance between the addition of Cu^{2+} ions to the carboxylic acids on both the original layer and the adlayer with the loss of adlayer molecules.

It is unclear if the free thiols on the inverted MHA molecules react with the copper and allow for the formation of an adlayer at that site as well. Previous work on dithiol

multilayers suggest that it would be a site for another thiol molecule to react with.[8] When Cu (II) ions were added to a dithiol monolayer the copper was reduced to Cu(I) by reacting with the free thiols on the surface. This allowed further growth of adlayers of thiols by the coordination of the Cu^{1+} ions and an adlayer thiol molecule. We are unable to draw any conclusive conclusions from our data to confirm if this reaction was occurring, though based on this previous work it is likely that it does occur.

4.3.2.4 Formation of a MH capping layer to a MHA|MHA bilayer

The addition of a MH 'capping' layer is then used to cover the surface with a nonreactive terminal group to limit the further growth of the film to 3 layers. The copper coordinated MHA|MHA surfaces were placed in ~5 mM MH solutions in ethanol for varying times ranging from 10 minutes to 24 hours, the results given in this section are for a 2 hour solution deposition time unless otherwise stated. A reduction of the Cu(II) on the surface is clearly observed in the Cu $2p_{3/2}$ XPS spectra (Figure 4.18H) as a significant reduction in the Cu(II) and increase in Cu(I) content on the surface relative to that before the MH addition to the Cu^{2+} coordinated MHA|MHA bilayer (Figure 4.18G.) However, the presence of some Cu(II) ions in the multilayered film can also be seen, as a shoulder peak at 934.5eV, their presence is attributed to the inverted carboxylic acid molecules in the second layer sterically preventing the MH molecules from reacting with the Cu(II) ions. The presence of inverted adlayer MHA molecules in the second layer is also evidenced in the IR spectra by the carboxylate stretches clearly seen, see Figure 4.14H. We are unable to determine if the amount of Cu(II) in the multilayered film is similar to of the MHA|MHA bilayer due to both the attenuation of the XPS signal and the autoreduction of the copper under exposure to the X-Ray beam. The S 2p XPS spectra

shows a significant increase in the Cu-S component at 162.4 eV relative to the Au-S component at 161.9 eV, see Figure 4.20H. Unlike the MHA|MH bilayer, the relative depths of the sulfur atoms at the three interfaces is unclear, and thus it is impossible to get an accurate proportion of how much sulfur is at each interface in this case. The XPS result suggests that the addition again causes a reduction of copper from Cu(II) to Cu(I) ions by a thiol group, and consequentially the protonation of the carboxylate groups to carboxylic acids, through the same reaction observed for previous additions of a thiol molecule.

Further evidence of this reaction can be seen in IR spectrum of the trilayer structure (Figure 4.14H.) The carboxylic acid stretches return, at 1742 and 1717 cm^{-1}, indicating that the carboxylate ions in the film were protonated into carboxylic acids. Hydrogen bonding is also observed in the high frequency IR by the presence of the broad OH stretching present at ~2800 to 3400 cm^{-1}, though it is significantly weaker than seen in a MHA|MHA bilayer (Figure 4.14F). This reduced hydrogen bonding, observed with previous MH additions, is again believed to be due to the mixture of carboxylic acids and carboxylate ions at the Cu-S interfaces. The addition of the deuterated MH molecules is evident in the addition of C-D stretches, while a slight loss of intensity in the C-H stretches indicates some MHA molecule loss, presumably due to exchange with MH molecules. We are unable to determine weather the MHA molecular loss occurs at the Au-S interface or at the Cu-S interface.

The addition of MH to the surface is presumed to occur at both of the two different copper carboxylate interfaces resulting in a mixed second layer and a third layer of pure MH. Upon addition of the MH the thickness of the sample increases to 48±2Å. This is

significantly lower than from previously proposed thickness estimations based on the number of layers in a system (3 layers ~60 Å) [6,7]. This thickness is attributed to a relatively low coverage of the third layer. The second layer had an MHA adlayer coverage of less than 50% of the first layer, after the addition of the MH this layer is densified by the added presence of MH molecules. The third layer, however, has a reduced number of copper carboxylate complexes to react with and form an MH adlayer on (the middle MHA layer is presumed to have slightly less than a 50% MHA coverage relative to the MHA underlayer assuming minor MHA loss due to copper exchange) this would result in a coverage less than 25% of the MHA underlayer. When a carboxylic acid terminated monolayer is used as the third layer this lower top layer coverage would also be the case. However, since the 'holes' in the second layer would be filled with possible reaction sites (either the carboxylic acid or thiol functional groups would be the terminal function group), further additions of copper and carboxylic acid terminated adlayers would increase the density in each of the lower layers and build up the thickness of the multilayered film. This delayed build up and densification can be continued by the sequential addition of Cu^{2+} ions followed by α,ω-mercaptoalkanoic acid until a desired film thickness is achieved.

By repeating the copper and MH addition steps a denser multilayered structure will be formed in the same manner as the MHA|MH bilayer structure. Results of both the ionization of the carboxylic acid groups and adlayer exchange are seen with the addition of the Cu^{2+} ions. The addition of Cu^{2+} ions to this trilayer structure causes a loss of intensity of both the C-D and C-H stretches in the IR spectrums, implying a loss of material in both the second and third adlayers. The results of the second addition of the

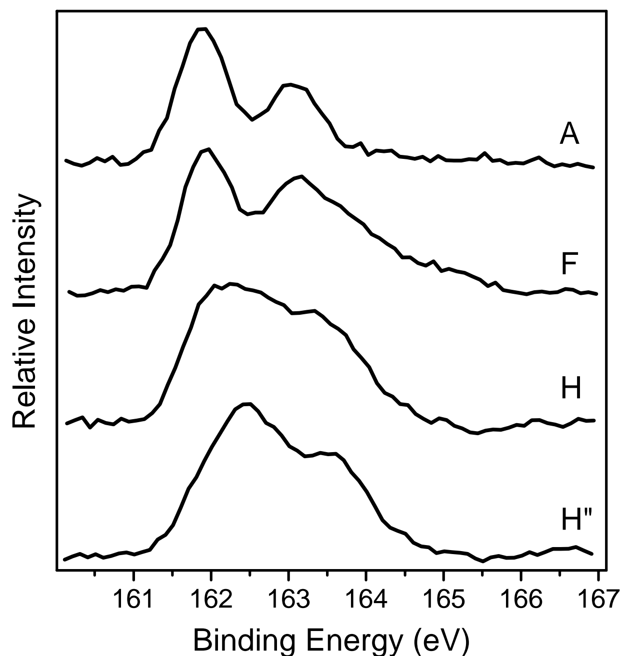

Figure 4.20. XPS spectra for steps A, F, H and H” of growth for a trilayer film.

MH is also very similar to the previous MH additions and results in a final thickness of 56±2Å. The S 2p XPS spectra is of note since the thickness of the film is enough that the emission of the Au-S species are more difficult to see due to signal attenuation. While this happens throughout the growth of the film it is most evident after the second addition of the MH to the trilayer films where the Cu-S species dominates the spectra with only a shoulder of the Au-S is observable, see Figure 4.20H”.

4.4 Conclusions

The results of this study point to a different growth mechanism than what has been previously proposed, and provides details on how to reproducibly grow multilayer films. The film growth was found to follow the following growth scheme. The addition of the Cu^{2+} ions to a α,ω-mercaptoalkanioc acid/Au SAM results in the complete and uniform metathesis reaction of the Cu^{2+} ions and the carboxylic acid groups on the surface to form a copper carboxylate complex with two $–CO_2^-$ groups bound to each Cu^{2+} ion. The interaction between two charged $–CO_2^-$ terminal groups causes a conformational disordering of the SAM alkane chains as the terminal groups are forced apart by electrostatic forces. The addition of an adlayer thiol molecule was found to reduce the Cu^{2+} ions to Cu^{1+} ions and the protonation of 50% of the carboxylates on the surface to carboxylic acids. The results support RS-Cu(I)-O_2C– interfacial bonding and a 50% adlayer coverage relative to the original α,ω-mercaptoalkanioc acid molecules on the surface. The mixed interface of carboxylate ions and carboxylic acid functional groups removes the ionic interaction between the underlayer's terminal groups and causes a complete recovery in the conformational ordering of the α,ω-mercaptoalkanioc acid underlayer. The adlayer coverage can be increased past this point by continued cycles of Cu^{2+} ions complexation of the free -CO_2H groups followed by chemisorption of RSH. If an alkanethiol is used then the overall number of layers in the stack does not increase, rather the adlayer densifies. These denser multilayers could lead to the formation of MRFs that are more resistive to metal penetration. If the adlayer molecules are thiocarboxylic acids this results in a delay in the buildup of the multilayer films with much of the copper ions and thiocarboxylic acid molecules being used to fill 'holes' in

the multilayer film and increase the total thickness of the film simultaneously. This delayed build up does not produce multilayer thicknesses that are integer multiples of the length of the thiocarboxylic acid molecules, but it does allow for a continuous growth of the film. The delayed build up of the multilayer and formation of 'holes' could be responsible for rough topographies in MRFs if the layers are not allowed to densify fully.

In disagreement with previous reports,[7] we find that adlayers of thiocarboxylic acids coordinate to a Cu(II) coordinated interface via sulfur copper and carboxylate copper complextion. The fraction of thiocarboxylic acids coordinated to the copper via carboxylate terminal groups can be reduced by extending the solution exposure time but cannot be completely removed. This is unfortunate for one of the original suggested uses of multilayer films in nonlinear optical applications[6,7] which require noncentrosymmetric materials, however it is unclear how much of an effect this symmetry would have on the optical properties of multilayered films. However, this is not believed to have a negative effect on MRFs since Cu(II) has been used to form multilayer structures with thiol terminated surfaces and thiol adlayer molecules.[8] A comparison of odd and even chain length α,ω-mercaptoalkanioc acid molecules for use in multilayer structures showed differences arising presumably from the different orientations of the -CO_2H groups. The odd-length chains, however, were found to be more prone to contamination than the even-length chains. This contamination could then lead to less reproducible results. However, with care both surfaces were found to produce similar results.

---

[1] Hatzor, A.; Weiss, P. S. *Science* **2001,** *291*(5506), 1019-1020

[2] Anderson, M. E.; Tan, L. P.; Tanaka, H.; Mihok, M.; Lee, H.; Horn, M. W.; Weiss, P. S. *J. Vac. Sci. Technol., B.* **2003,** *21*(6), 3116-3119

[3] Anderson, M. E.; Smith, R. K.; Donhauser, Z. J.; Hatzor, A.; Lewis, P. A.; Tan, L. P.; Tanaka, H.; Horn, M. W.; Weiss, P. S. *J. Vac. Sci. Technol., B.* **2002,** *20*(6), 2739-2744

[4] Anderson, M. E.; Srinivasan, C.; Jayaraman, R.; Weiss, P. S.; Horn, M. W. *Microelectron. Eng.* **2005,** *78-79* 248-252.

[5] Nuzzo, R.G.; Dubois, L.H.; Allara, D.L. *J. Am. Chem. Soc*. **1990**, *112*, 558-569

[6] Evans, S. D.; Ulman, A.; Goppertberarducci, K. E.; Gerenser, L. J. *J. Am. Chem. Soc*. **1991,** *113*(15), 5866-5868

[7] Freeman, T. L.; Evans, S. D.; Ulman, A. *Langmuir* **1995,** *11*(11), 4411-4417

[8] Brust, M.; Blass, P. M.; Bard, A. J. *Langmuir* **1997,** *13*(21), 5602-5607

[9] Auer, F.; Nelles, G.; Sellergren, B. *Chem-Eur J.* **2004,** *10*(13), 3232-3240

[10] Cheng, W. L.; Dong, S. J.; Wang, E. K. *Chem. Mater.* **2003,** *15*(13), 2495-2501

[11] Lee, H.; Kepley, L. J.; Hong, H. G.; Mallouk, T. E. *J. Am. Chem. Soc*. **1988,** *110*(2), 618-620

[12] Lee, H.; Kepley, L. J.; Hong, H. G.; Akhter, S.; Mallouk, T. E. *J. Phys. Chem.* **1988,** *92*(9), 2597-2601

[13] Tillman, N.; Ulman, A.; Penner, T. L. *Langmuir* **1989,** *5*(1), 101-111

---

[14] Ansell, M. A.; Zeppenfeld, A. C.; Yoshimoto, K.; Cogan, E. B.; Page, C. J. *Chem. Mater.* **1996,** *8*(3), 591-594

[15] Zhang, W. W.; Lu, C. S.; Zou, Y.; Xie, J. L.; Ren, X. M.; Zhu, H. Z.; Meng, Q. J. *J. Colloid and Interface Sci.* **2002,** *249*(2), 301-306

[16] McCarty, G. S. *Nano Lett.* **2004,** *4*(8), 1391-1394.

[17] Nishi, N.; Hobara, D.; Yamamoto, M.; Kakiuchi, T. *J. Chem. Phys.* **2003,** *118*(4), 1904-1911

[18] Azzam, W.; Cyganik, P.; Witte, G.; Buck, M.; Woll, C. *Langmuir* **2003,** *19*(20), 8262-8270

[19] Lin, S. Y.; Tsai, T. K.; Lin, C. M.; Chen, C. H.; Chan, Y. C.; Chen, H. W. *Langmuir* **2002,** *18*(14), 5473-5478

[20] Tidwell, C. D.; Ertel, S. I.; Ratner, B. D.; Tarasevich, B. J.; Atre, S.; Allara, D. L.; *Langmuir* **1997**, *13*(13), 3404-3413.

[21] Bain, C. D. Ph.D. Thesis, Harvard University, **1988**.

[22] Stapleton, J. J.; Harder, P.; Daniel, T. A.; Reinard, M. D.; Yao, Y. X.; Price, D. W.; Tour, J. M.; Allara, D. L. *Langmuir* **2003,** *19*(20), 8245-8255.

[23] Shi, J.; Hong, B.; Parikh, A. N.; Collins, R. W.; Allara, D. L. *Chem. Phys. Lett.* **1995,** *246*(1-2), 90-94. Given that other approximations were required, e.g., the refractive index of the Cu-SAM interfaces (see next two footnotes), the use of isotropic chain model, as opposed to a more accurate an anisotropic chain model, seemed appropriate.

[24] As no refractive indexes at 632.8 nm were available for the type of Cu^{+2} species that would be present in the carboxylate surface layer the average refractive indexes of

different simple copper salts was used to provide an estimate of an average value: Atacamite ($Cu_2(OH)_3Cl$) ~1.9, Azurite ($Cu_3(OH)_2(CO_3)_2$) ~1.8, Malachite ($Cu_2(OH)_2(CO_3)$) ~1.8, Marshite (CuI) ~ 2.3, and Nantokite (CuCl) ~1.9.

[25] *Effects of Optical Anisotropy on Spectro-Ellipsometric Data for Thin Films and Surfaces* , A. N. Parikh and D. L. Allara, in *Optical Studies on Real Surfaces and Inhomogeneous Thin Films*, Vol. 19, Physics of Thin Films Series, M. Francombe, ed., Academic Press, 1994, pp. 279-323

[26] Parikh, A. N.; Allara, D. L. *J. Chem. Phys.* **1992,** *96*(2), 927-945.

[27] Stapleton, J. J.; Harder, P.; Daniel, T. A.; Reinard, M. D.; Yao, Y. X.; Price, D. W.; Tour, J. M.; Allara, D. L. *Langmuir* **2003**, *19*, 8245-8255.

[28] Socrates, G. *Infrared and Raman Characteristic Group Frequencies*; John Wiley & Sons, LTD: Chichester, 2001.

[29] Laibinis, P. E.; Nuzzo, R. G.; Whitesides, G. M. *J. Phys. Chem.* **1992**, *96*, 5097-5105

[30] Xu, C.J.; Sun, L.; Kepley, L.J.; Crooks, R.M.; Ricco, A.J. *Anal. Chem.* **1993**, *65*, 2102-2107

[31] Snyder, R.G.; Strauss, H.L.; Elllger C.A. *J. Phys. Chem.* **1982**, 86, 5145-5150

[32] Snyder, R. G.; S. L. Hsu S. L.; Krimm S. *Spectrochima Acta A* **1978**, 34, 395-406

[33] Arnold R.; Azzam W.; Terfort A; Woll C. *Langmuir* **2002**, 18, 3980-3992

[34] Moulder J.F., Ed.; *Handbook of X-ray photoelectron spectroscopy*; Perkin-Elmer Corporation: Eden Prairie, Mn, 1992

[35] The thickness for all simulations are base on the SWE measurements taken for each film. A refractive index of 1.48 was used for the organic layers

---

[36] Whitesides G.M.; Laibinis P.E. Langmuir 1990, 6, 87-96

[37] Duwez, A. S. *J. Electron Spectrosc. Relat. Phenom.* **2004,** *134*(2-3), 97-138.

[38] For general information on charging effects observed in XPS see- Briggs, D.; Grant J.T. Surface *Analysis by Auger and X-Ray Photoelectron Spectroscopy*; IM Publications and SurfaceSpectra Limited: West Sussex, UK 2003

[39] Bain, C. D.; Troughton, E. B.; Tao, Y. T.; Evall, J.; Whitesides, G. M.; Nuzzo, R. G. *J. Am. Chem. Soc.* **1989**, *111*, 321-335.

[40] Parikh, A. N.; Liedberg, B.; Atre, S. V.; Ho, M.; Allara, D. L. *J. Am. Chem. Soc.* **1995,** *99*(24), 9996-10008

[41] Laffineur, F.; Delhalle, J.; Guittard, S.; Geribaldi, S.; Mekhalif, Z. *Colloids Surf. A.* **2002,** *198* 817-827

[42] The peaks in each Sulfur spectra were constrained in the same manner so as to have a self consistent comparison. The area of the $S_{2p\ 1/2}$ electrons are set to ½ that of the $S_{2p\ 3/2}$ electrons, the positions of the $S_{2p\ 1/2}$ electrons are fixed to be 1.2 eV higher than that of the $S_{2p\ 3/2}$ electrons, the positions of the $S_{2p\ 3/2}$ electrons were fixed to the literature values of 161.9 for Au-S, 162.4 for Cu-S and 163.5 for S-H. The full width half maximums of the peaks are allowed to range from 0.8 to 1.0 eV based upon the FWHM of bare monolayer spectrums and the FWHM of all the peaks are fixed equal to each other. If different constraints are used the ratio between the sulfurs can differ significantly, but the trend between what happens to the ratios is consistent.

[43] Jablonski, A.; Powell, C. J. *Surf. Sci. Rep.* **2002,** *47*(2-3), 35-91.

[44] To calculate the relative intensity it is necessary to first take into account the depth of the samples and how much the signal is attenuated. The intensity of each sulfur

atoms were adjusted using the following equation. $I(S)=I_0(S)e^{-d/\lambda \sin \theta}$ where I(S) is the intensity from the gold photoelectrons attenuated by the monolayer, $I_0(S)$ is the intensity of a clean sulfur substrate, d is depth, θ if the take off angle (90°), and λ is the photoelectron mean free path (3.6 nm). By manipulating the equation the ratio S-Cu to S-Au can be found $I_{S\text{-}Au} / I_{S\text{-}Cu} = e^{-\Delta d/\lambda}$ where Δd is the difference in the depth between the two sulfurs. For 16-Mercaptohexadecanoic acid the ratio is $I_{S\text{-}Au} / I_{S\text{-}Cu} = 0.558$ and for 15-Mercaptoheptadecanoic acid the ratio is $I_{S\text{-}Au} / I_{S\text{-}Cu} = 0.574$.

[45] The positions for the d^+ and d^- C-D modes taken from the deuterated MH monolayers used in these experiments as IR reference spectra.

[46] MH molecules physical length is ~23.5 Å using a tilt angle of 41° the thickness of the adlayer should be 17.7 Å which is within the experimental error of the Ellipsometry measured thickness of 18 Å. The physical length is derived from information in reference 23

[47] As much as 35% reductions were seen over the longer solution deposition time periods, ranging from 1 to 24 hrs. By rinsing the surface in a 5% HCl ethanolic solution, the IR will return to its original spectrum of a clean carboxylic acid terminated surface. In many cases amounts of C-D stretches can be seen along with a slight deterioration of the C-H stretches. We believe that this is due to insertion of the deuterated MH into the 16-Mercaptohexadecanoic acid monolayer and not an incomplete reaction of the HCl with the Copper ions. By using both the reduction in intensity of C-H stretches and the intensity of the C-D stretches relative to a full monolayer accurate measurements for insertion percentage can be taken.

---

[48] An average of 5% of the original intensity often remains, this intensity does not significantly decrease with longer copper solution deposition times. The remaining signal is attributed to a small fraction of the reactive carboxylic acid sites at the interface being protected by hexadecane thiol molecules physically blocking the path to the acid group.

[49] With deposition times, above 2 hours, the presence of free thiol 164 eV can sometimes be seen in the sulfur XPS spectra. Indicating significant amounts of physisorbed hexadecane thiol on the surface.

[50] The size estimates are made with Chem3D Ultra. The distances from the sulfur atom to the farthest away hydrogen are used for comparison. For Hexadecane thiol the distance from S to H_{33} is 21.3 Å, for 16-Mercaptohexadecanoic acid it is 22.3 Å.

[51] It is possible that some of the adlayer did not react with the copper thus forming an incomplete adlayer, however longer deposition times did not reduce these peaks significantly.

[52] Yen, Y.S.; Wong J.S. *J. Phys. Chem.* **1989**, 93(20), 7208-7216

[53] With out knowing the surface density of these adsorptions and due to the overlapping CH wagging modes it is difficult/impossible to accurately determine what this orientation is.

[54] Castner, D. G.; Hinds, K.; Grainger, D. W. *Langmuir* **1996,** *12*(21), 5083-5086

Chapter 5

Electronic and Chemical Stability of Isocyanide Bound Molecular Wire Monolayers on Palladium Surfaces

5.1 Introduction

With the increased interest in fabricating electronic devices based on molecules and molecular assemblies, it is becoming critically important to understand the detailed way in which the molecules bond and organize at electrode surfaces. Self-assembled monolayers (SAMs) have become a useful test bed for investigating the electronic properties of device candidate molecules [1] as well as being the most common configuration for such devices. One family of candidate structures used extensively in recent studies is based on SAMs made from various derivatives of 4,4'-di(phenylene-ethynylene)benzenethiol[2] [commonly referred to as oligo(phenylene-ethynylene)thiol or OPE-SH]. It has been shown that the current-voltage behavior of these molecules can be altered by changing ring substituents.[3 - 5] Further flexibility in tailoring the electrical properties of the SAMs is possible by altering the headgroup used to anchor the molecule to the base electrode and by varying the electrode material.[6] While attachment of molecules to a gold substrate via a sulfur atom has been studied extensively[7,8] far less attention has been paid to alternative attachment chemistries. Of particular note are recent reports showing that bonding to gold via tellurium,[9] selenium,[10 - 20] and the isocyanide group (-N≡C) [21- 35] is possible. Furthermore, there has been little work done on the assembly of organic molecules on alternate metals such as palladium, an attractive alternate for device contacts,[21, 36] despite the fact that electrical measurements of isocyanide SAMs bound on Pd appear to exhibit improved junction properties over those on Au.[37]

Given the reports that -NC/noble metal junctions exhibit lower conduction barriers than the corresponding thiol-based junctions,[28] it is important for molecular

electronic applications to establish in detail the attachment mechanism(s) of isocyanide terminated device type molecules since the attachment mode could affect the molecular orientation and packing. The differences in charge transport properties between -S and -NC bound molecules are presumably due to variances in the electronic structure of the headgroups which result from different orbital overlaps between the molecular and the electrode surface states. Calculations of a CH_3S- moiety bound to a $(Au)_{16}$ cluster indicate that bonding at a (111) hollow site results in transfer of ~0.4 e^- to the S atom with residual positive charge on the surrounding gold atoms.[38] The nature of the ArNC-metal bond (where Ar = an aryl group, the common constituent structure of device molecules) is complicated by possible multiple bonding interactions with the metal substrate. For example, in the case of commonly used transition metal electrodes, coordination of ArNC- typically results in a σ-type bond via donation by the carbon lone pair to the metal substrate. When the metal has filled d-orbitals capable of overlapping the π* antibonding orbitals of the -N≡C moiety, a back donation π-type bond also may form.[39] In the specific case of Au, two reports concluded that the (ArNC)-Au bond is formed dominantly by σ-donation from the carbon lone pair of the isocyanide group to a gold atom (figure 5.1, structure I).[21,27]

In one study directly comparing aromatic isocyanide SAM bonding on Pd and Au, Bennett and co-workers, used infrared spectroscopy (IR) to characterize the surface bonding.[21] For adsorption of 1,4-diisocyanobenzene on thermally evaporated Pd film surfaces, they observed a strong IR band at ~1960 cm^{-1}, considerably lower in frequency than the uncoordinated isocyanide (2127 cm^{-1}), which was interpreted in terms of a back bonded type of species assigned to either or both of two structures (II and III in figure

1).[21] In addition, another large band observed at 2170 cm^{-1} was assigned to a σ-donation species (structure I, figure 5.1).[40] Time dependent adsorption studies suggested that the isocyanide group initially bonds through σ donation and eventually shifts to more stable σ/π sites. Such a result would indicate that the specific morphology of the metal substrate could have a strong effect on the type of bonding. No details of molecular structure such as molecular orientation were given in their paper.

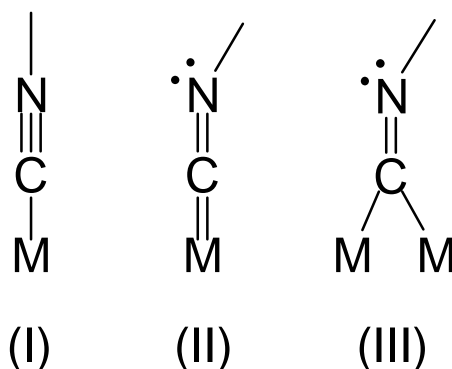

Figure 5.1. Bonding structures for OPE-NC SAMs on Au (I) and Pd (II or III)

In a more recent study, Allara and co-workers [41], the preparation and characterization of SAMs of the terminal isocyanide derivative of 4,4'-di(phenylene-ethynylene)benzene (OPE-NC, in figure 5.2) on Pd{111} was done. The study explored in detail the attachment chemistry and SAM molecular structure for the OPE system, used commonly for device measurements, on a closely controlled study of Pd surfaces. Of particular interest was the chemical stability of the molecule-metal bonding under normal preparation and handling conditions since the behavior of a molecular device will depend critically on the integrity of the molecules and their attachment.

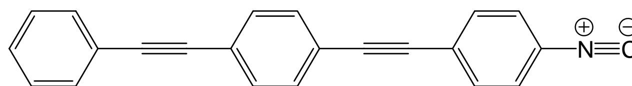

Figure 5.2. Chemical structure of OPE-NC.

The methodology utilized multiple characterization techniques including quantitative infrared reflection spectroscopy (IRS), x-ray photoelectron spectroscopy (XPS), single wavelength ellipsometry (SWE), atomic force microscopy (AFM; tapping mode), liquid drop contact angles, and quantum chemical calculations. The results were in contrast to the earlier results[21], and show that a σ/π type bond forms on Pd when smooth, {111} textured surfaces are used. More importantly, with implications for molecular devices, the study showed that even brief exposures to an ambient environment for minutes to hours can result in significant degradation of the attachment bonding of the SAMs on Pd. Exposure was found to result in a crosslinking reaction of the -NC groups to a quasi-2D imine polymer, again with loss of chemical bonding. This effect will result in significant loss in the junction integrity of a molecular device. In this study the implications of this prediction are confirmed directly by conducting probe atomic force microscope measurements for the Pd case.

5.2 Experimental

5.2.1 Synthesis

Details of the synthesis and characterization of OPE-isocyanide compound (**OPE-NC**, figure 5.2) are given in Appendix C.

5.2.2 Sample Preparation

The metal films were deposited onto silicon substrates (~1.5 nm of native oxide) which were cleaned with H_2O_2/H_2SO_4 solution, rinsed copiously with water and ethanol then blown dry with N_2. The Pd depositions were carried out using argon ion sputtering (saddle field ion guns obtained from South Bay Tech, Torrance, CA) of the metal targets (Kurt J. Lesker, Cleveland, OH) and sequential deposition of ~5 nm Cr and ~175 nm Pd films onto a rotating substrate. The Pd/Cr/SiO_2/Si films typically showed a rms roughness of 0.8(±0.15) nm by tapping mode AFM. X-ray diffraction analysis of the Pd films (using the CHESS facility at Cornell) showed a highly {111} textured surface with the grains oriented 3(±9)º from the surface normal.[42] The freshly evaporated metal substrates were immediately characterized by SWE and then used within 15 minutes ambient exposure to form the SAM.

Monolayer preparation was carried out in a nitrogen-purged glove box with the O_2 concentration kept below 2 ppm to avoid oxidative degradation of the reagents and the SAMs. All solutions were mixed and stored in screwtop fluoroware containers. SAMs of OPE-NC were formed in 1 mM solutions prepared by dissolving the compound in dichloromethane (freshly distilled over P_2O_5 under a nitrogen atmosphere). The substrates then were added and the solution stored overnight (~18-24 h). After monolayer formation the wafers were rinsed with distilled dichloromethane and dried under a stream of N_2. Prior to removal from the glove box and to minimize ambient exposure the samples were sealed in nitrogen filled bags for transfer to the load lock of the UHV-AFM. After the initial measurements were made the samples were placed back in the load lock and vented to atmosphere for ~18hrs, then placed back into vacuum for post exposure analysis.

5.2.3 Conducting Probe Atomic Force Microscopy (CP-AFM)

The conducting probe measurements (CP-AFM) were performed in a UHV chamber (base pressure 10^{-10} Torr) outfitted with a RHK 350 scan head controlled by a RHK SPM 100 electronics system (RHK technologies, Troy, MI). Electrical measurements were made with double side Pt-Ir(90/10) coated cantilevers (EFM type tips, spring constant ~2.8 N/m, tip radius ~20 nm; Molecular Imaging, Tempe, AZ). Current-voltage (I-V) measurements were made for each SAM as follows. First, tip damage was minimized by careful sample approach, tip retract approach mode.[43] Once surface contact was established force−distance measurements were used to verify the tip integrity, any damaged tips were discarded.[44] During I−V measurements the applied force on the tip was kept as low as possible, generally settling in around 10 nN due to the limitations of the attractive forces.[45] The measurements were then performed by sweeping the surface bias over ±1 V.[46]

5.3 Results

5.3.1 Conductance (CP-AFM) Measurements on the Chemically Degraded 1-Pd SAM

The measurements were made by introducing the sample into the measurement chamber (base pressure 1×10^{-10} Torr) through a loadlock system, selecting a specific cantilever from a set of available ones stored in the vacuum chamber and then performing sets of ±1 V sweeps.[46] In order to obtain good statistics, a set of 4 consecutive scans was made with the selected tip at a given surface location. The tip was then moved to another

location to repeat the scan set such that at least 12 arbitrarily chosen different locations on the surface were sampled. The I-V data was then averaged for each tip giving at least 48 data points. In addition, complete sets of I-V measurements were performed using 3 different tips. This protocol was followed for different **1**-Pd SAMs in which each SAM was sampled when freshly made and again after ambient exposure for 18 hrs. Representative results, shown in figure 3, are based on 3 tips scanning a total of 62 different spots (standard deviation of ±60 pA at 1 V bias) for the unexposed sample and 3 tips scanning a total of 80 different spots (standard deviation of ±8 pA at 1 V bias) after 18 hr ambient exposure.[47]

The results clearly show on average a severe decrease of the SAM-Pd junction conductance, by ~2 orders of magnitude, after 18 hr exposure to ambient. The much larger fluctuations in the measurements for the exposed sample (±60 *vs* ±8 pA at +1 V) are due primarily to spot to spot variations across the sample surface. Given the approximate tip-molecule contact area of ~10 nm^2 (an ~ 20 nm radius of tip curvature applied with ~10 nN force), contact involves <100 molecules. This result suggests that the integrity of the molecule-Pd contact varies roughly over this distance scale, or greater, across the ambient exposed SAM surface. Presuming that the loss of conductance is due to conversion of –N=C=Pd moieties to poly(imine) the data further suggest that polymerization initiates at scattered defects in the SAM, possibly where reactive oxygen species can readily diffuse to the substrate.

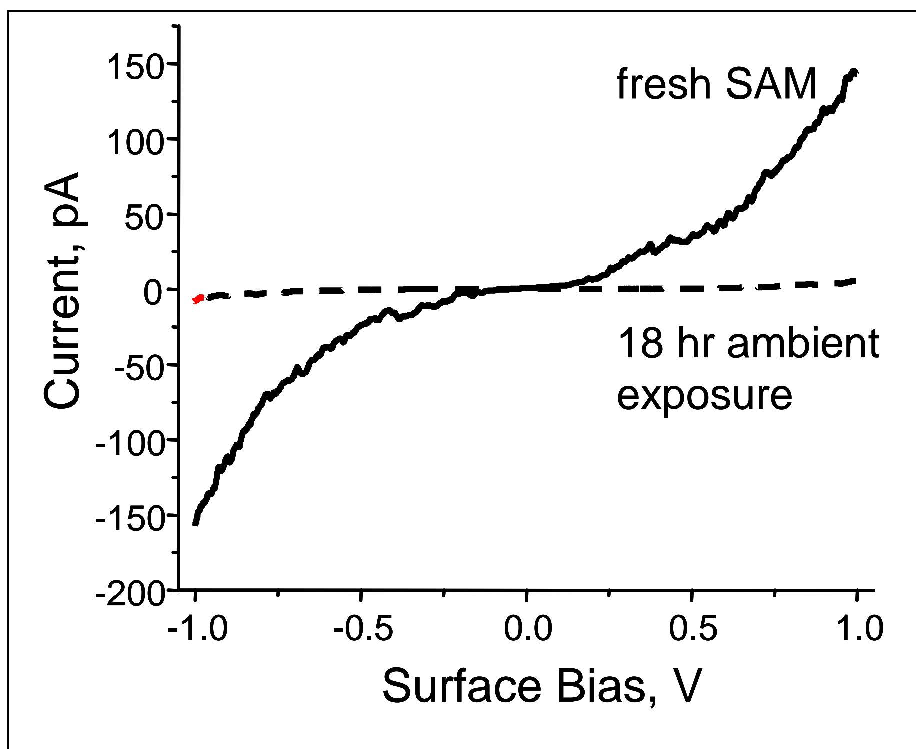

Figure 5.3. CP-AFM I-V scans for a representative OPE-NC/Pd SAM before and after 18 hr ambient exposure. The curves represent an average of 186 and 240 measurements for the fresh and exposed SAM, respectively with respective standard deviations of ±60 and ±8 picoAmps. For details see text.

5.4. Summary and Conclusions

The results are summarized with reference to the schematic illustrations in figure 5.4, which show that intrinsic SAM structures involve a two-fold type of coordination for the palladium surface. This conclusion is supportive of the work previously done by, Allara and coworkers,[41] but conflicts with the earlier proposal of an additional σ/Pd

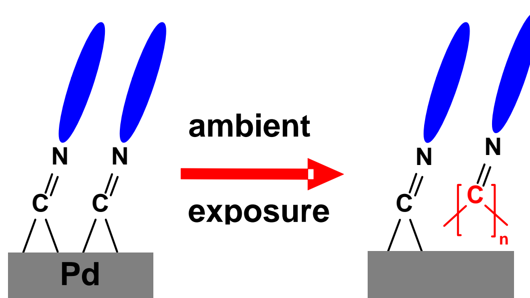

Figure 5.4. Schematic illustration of the main chemical and structural features of the OPE-NC SAMs on a Pd substrate prepared under rigorous conditions with minimum exposure to laboratory ambient and after storage in laboratory ambient. The illustration shows the same type of tilted molecule structure but with an initial bridge bonded isocyanide group which slowly converts to a polymeric species over time at ambient temperature. The headgroups, while stable to oxidation reactions, slowly convert with time to a poly(imine) type of polymer film with associated loss in organization and packing of the molecules.

bonding mode.[21] This discrepancy is attributed to differences in substrate character such as morphology and conclude that on smooth, highly {111} textured Pd surfaces only the σ/Pd bonding mode forms. Further work to resolve this issue would require UHV studies involving single crystals.

With the SAM on Pd loss of chemical bonding to the substrate can occur via polymerization of the isocyanide to poly(imine). While substrate debonding does occur,

solvent resistance of the SAM remains, presumably due to the polymeric character of the degraded regions of the SAM.[41] The debonding observed for the SAMs suggests that the electrical integrity of SAM molecule-electrode substrate contacts would be severely degraded. This is confirmed for the case of the degraded OPE-NC/Pd SAM, where electrical contact might be expected to be maintained since polymerization should hold the molecules in place adjacent to the electrode surface. Extensive CP-AFM measurements, in fact, show that the electrical conductance of ambient exposed OPE-NC/Pd SAMs can be reduced by roughly two orders of magnitude, even for only 18 hrs ambient exposure. Finally, we note that a series of preliminary experiments with ω-octadecyl and other alkyl isocyanides, performed on Pd substrates identical to the present ones, show no evidence for formation of isocyanate under any of the above conditions.[48] Thus the propensity for ambient induced degradation appears much higher for the aromatic based analogs. This difference could be due to the intrinsic differences in the isocyanide groups in the alkyl and aryl molecules, e.g., polarity of and conjugation effects, or to the higher packing density of the alkyl systems which could slow diffusion of reactive species to the substrate surface. A further understanding of the fundamental mechanisms involved in these surface degradation processes will require extensive experimental work, including single crystal substrates, *in-situ* characterization, controlled UHV conditions with dosing by oxygen and other reactants.

Overall these results illustrate the care that must be taken in the preparation and subsequent exposure of these films in order to obtain and maintain the intrinsic molecular and substrate junction structure. The loss of direct headgroup bonding to the metal substrates, which can arise upon storage, can be highly deleterious for such applications

as molecular electronic devices where the interface integrity can be a critical parameter in evaluating the intrinsic electrical character of the interface and in the ultimate performance characteristics of the devices.

5.5. Acknowledgements

Financial support is acknowledged from the Naval Research Laboratories (JS, DA, JN, RS), the Army Research Office (JS, DA), the Defense Advanced Research Project Agency (SU, DA) and the Office of Naval Research (OC, DA).

References

[1] (a) James, D.K.; Tour, J.M. *Chem. Mater.* **2004**, *16*, 4423-4435. (b) Salomon, A.; Cahen, D.; Lindsay, S.; Tomfohr, J.; Engelkes, V.B.; Frisbie, C.D. *Adv. Mater.* **2003**, *15*, 1881-1890.

[2] Tour, J. M. *Acc. Chem. Res.* **2000**, *33*, 791-804.

[3] Rawlett, A. M.; Hopson, T. J.; Nagahara, L. A.; Tsui, R. K.; Ramachandran, G. K.; Lindsay, S. M. *Appl. Phys. Lett.* **2002**, *81*, 3043-3045.

[4] Chen, J.; Wang, W.; Reed, M. A.; Rawlett, A. M.; Price, D. W.; Tour, J. M. *Appl. Phys. Lett.* **2000**, *77*, 1224-1226.

[5] Chen, J.; Reed, M. A.; Rawlett, A. M.; Tour, J. M. *Science* **1999**, *286*, 1550-1552.

[6] Seminario, J. M.; Zacarias, A. G.; Tour, J. M. *J. Am. Chem. Soc.* **1999**, *121*, 411-416.

[7] Schreiber, F. *Prog. Surf. Sci.* **2000**, *65*, 151-256.

[8] Ulman, A. *Chem. Rev.* **1996**, *96*, 1533-1554.

[9] Nakamura, T.; Yasuda, S.; Miyamae, T.; Nozoye, H.; Kobayashi, N.; Kondoh, H.; Nakai, I.; Ohta, T.; Yoshimura, D.; Matsumoto, M. *J. Am. Chem. Soc.* **2002**, *124*, 12642-12643.

[10] Monnell, J.D.; Stapleton, J.J.; Jackiw, J.J.; Dunbar, T.; Reinerth, W.A.; Dirk, S.M.; Tour, J.M.; Allara, D.L.; Weiss, P.S. *J. Phys. Chem. B.* **2004**, *108*, 9834-9841.

[11] Sato, Y.; Mizutani, F. *Phys. Chem. Chem. Phys.* **2004**, *6*, 1328-1331.

[12] Protsailo, L. V.; Fawcett, W. R.; Russell, D.; Meyer, R. L. *Langmuir* **2002**, *18*, 9342-9349.

[13] Patrone, L.; Palacin, S.; Bourgoin, J. P.; Lagoute, J.; Zambelli, T.; Gauthier, S. *Chem. Phys.* **2002**, *281*, 325-332.

[14] Aslam, M.; Bandyopadhyay, K.; Vijayamohanan, K.; Lakshminarayanan, V. *J. Colloid Interface Sci.* **2001**, *234*, 410-417.

[15] Han, S. W.; Kim, K. *J.Colloid Interface Sci.* **2001**, *240*, 492-497.

[16] Bandyopadhyay, K.; Vijayamohanan, K.; Venkataramanan, M.; Pradeep, T. *Langmuir* **1999**, *15*, 5314-5322.

[17] Bandyopadhyay, K.; Vijayamohanan, K. *Langmuir* **1998**, *14*, 625-629.

[18] Huang, F. K.; Horton, R. C.; Myles, D. C.; Garrell, R. L. *Langmuir* **1998**, *14*, 4802-4808

[19] Dishner, M. H.; Hemminger, J. C.; Feher, F. J. *Langmuir* **1997**, *13*, 4788-4790.

[20] Samant, M. G.; Brown, C. A.; II, J. G. G. *Langmuir* **1992**, *8*, 1615-1618.

[21] Murphy, K. L.; Tysoe, W. T.; Bennett, D. W. *Langmuir* **2004**, *20*, 1732-1738.

[22] Caruso, A. N.; Rajesh, R.; Gallup, G.; Redepenning, J.; Dowben, P. A. *J. Phys.-Condens. Mat.* **2004**, *16*, 845-860.

---

[23] Joo, S. W.; Kim, W. J.; Yun, W. S.; Hwang, S.; Choi, I. S. *Appl. Spectrosc.* **2004**, *58*, 218-223.

[24] Kim, H. S.; Lee, S. J.; Kim, N. H.; Yoon, J. K.; Park, H. K.; Kim, K. *Langmuir* **2003**, *19*, 6701-6710.

[25] Joo, S. W.; Kim, W. J.; Yoon, W. S.; Choi, I. S. *J. Raman Spectrosc.* **2003**, *34*, 271-275.

[26] Bae, S. J.; Lee, C. R.; Choi, I. S.; Hwang, C. S.; Gong, M. S.; Kim, K.; Joo, S. W. *J. Phys. Chem. B.* **2002**, *106*, 7076-7080.

[27] Henderson, J. I.; Feng, S.; Bein, T.; Kubiak, C. P. *Langmuir* **2000**, *16*, 6183-6187.

[28] Hong, S.; Reifenberger, R. *Superlattice. Microstruct.* **2000**, *28*, 289-303.

[29] Lin, S.; McCarley, R.L. *Langmuir* **1999**, *15*, 151-159.

[30] Huc, V.; Bourgoin, J. P.; Bureau, C.; Valin, F.; Zalczer, G.; Palacin, S. *J. Phys. Chem. B.* **1999**, *103*, 10489-10495.

[31] Ontko, A. C.; Angelici, R. J. *Langmuir* **1998**, *14*, 3071-3078.

[32] Ontko, A. C.; Angelici, R. J. *Langmuir* **1998**, *14*, 1684-1691.

[33] Henderson, J. I.; Feng, S.; Ferrence, G. M.; Bein, T.; Kubiak, C. P. *Inorg. Chim. Acta* **1996**, *242*, 115-124.

[34] Shih, K. C.; Angelici, R. J. *Langmuir* **1995**, *11*, 2539-2546.

[35] Robertson, M. J.; Angelici, R. J. *Langmuir* **1994**, *10*, 1488-1492.

[36] Love, J.C.; Wolfe, D.B.; Haasch, R.; Chabinyc, M.L.; Paul, K.E.; Whitesides, G.M.; Nuzzo, R.G. *J. Am. Chem. Soc.* **2003**, *125*, 2597-2609.

[37] Chen, J.; Calvet, L. C.; Reed, M. A.; Carr, D. W.; Grubisha, D. S.; Bennett, D. W. *Chem. Phys. Lett.* **1999**, *313*, 741-748.

[38] Sellers, H.; Ulman, A.; Shnidman, Y.; Eilers, J. E. *J. Am. Chem. Soc.* **1993**, *115*, 9389-9401.

[39] Ugi, I. *Isonitrile Chemistry*; Academic Press: New York, 1974.

[40] Murpy, K.; Azad, S.; Bennett, D.W.; Tysoe, W.T. *Surf. Sci.* **2000**, *467*, 1-9.

[41] Stapleton, J.J.; Daniel, T.A.; Uppili S; Cabarcos O.M. Naciri J.; Shashidhar R.; Allara D.L. (Submitted for publication)

[42] Daniel T.A; Smilgies. D.; Allara, D.L.; unpublished results.

[43] The scan head has two separate z piezos, one for scan off sets and course approach Z steps and another for scanning the z direction only. The tip approached the surface in Tip-retract mode. The scan head would take one course z step with the z-scan piezo fully retracted. After the course z step was performed, the z-scan piezo is extended with a low gain insuring that the tip moves at a low speed. If the tip extended into the surface the approach would then stop. If no normal force change was detected, indicating the presence of the surface, the tip would be fully retracted again and another course Z step taken. This is repeated until the substrate surface is found, if

faster approach modes are used the metal tip will be blunted or other wise damaged leading to inconsistent contact areas and current measurements.

[44] The force distance curves is used as a relative measure of the tip radius of curvature. The higher the radius of curvature the higher the surface area between the tip and the substrate is. For damaged tips the adhesive force was determined to be 5 to 20 times higher than that of new clean tips (~10nN.) If a high adhesive force was found and was repeatable in different locations of the surface (done to insure that the tip is not just at a local defect causing higher forces) then the tip was removed from vacuum, discarded, and replaced.

[45] The average adhesive force was approximately 5 to 8 nN. To insure good and consistent contacts a total force of 10nN was applied to the surface.

[46] Sweeps started with a 1V bias and swept to -1 V bias in ~0.001 V steps before a return scan was done from -1-+1V. This alternating scan directions and small voltage steps were done to prevent transient currents. The bias was applied to the substrate while the AFM tip was grounded.

[47] No direct CP-AFM data on OPE SAMs appears to be available for comparison with our I-V curves but two studies have been done with SAMs of the three phenyl ring molecule [1,1':4',4"-terphenyl]-4-thiol on gold. Frisbie and co-workers applied ±0.3 V sweeps and report a 130 pA current at a 0.3 V tip bias [Wold, D.J.; Haag, R.; Rampi, M.A.; Frisbie, C.D., *J. Phys. Chem. B*. **2002**, *106*, 2813]. Ishida and co-workers in a similar study report ~1 nA currents at a 1 V tip bias [Takao Ishida, T.; Mizutani, W.; Liang, T-T.; Azehara, H.; Miyake, K.; Sasaki, S.; Tokumoto, H., Ann. N.Y. Acad. Sci., 2003, 1006: 164–186]. Considering the variations that one would

expect from typical variations in tip-molecule contact areas and from the intrinsic differences between the molecule−Au and −Pd junctions, these data compare reasonably with our observation of ~100-150 pA at a 1 V tip bias for the OPE-NC/Pd SAM.

[48] Stapleton, J.; Harder, P; Skulason, H.; Bader, M.; Allara, D., to be published elsewhere.

Appendix A

Supplemental Materials for Chapter 3

1. Preparation and Characterization of $CD_3(CD_2)_7(CH_2)_8SH$

Synthesis of CD_3-$[CD_2]_7$-$[CH_2]_8$-SH (4)

Hexadecyl-9,9,10,10,11,11,12,12,13,13,14,14,15,15,16,16 – d_{17} thiol (**4**) was synthesized as explained in Scheme 1. Hexadecanoic-9,9,10,10,11,11,12,12,13,13,14,14,15,15,16,16 – d_{17} acid (**1**) was obtained from CDN Isotopes, Pointe-Claire, Quebec, Canada. Borane-THF complex, phosphorus tribromide and potassium thioacetate were obtained from Aldrich Chemical Co. (Milwaukee, WI). NaOH was obtained from EMD Chemical (NJ) and concentrated HCl was obtained from J.T.Baker (NJ).

Scheme 1: Synthesis of CD_3-$[CD_2]_7$-$[CH_2]_8$-SH (**4**)

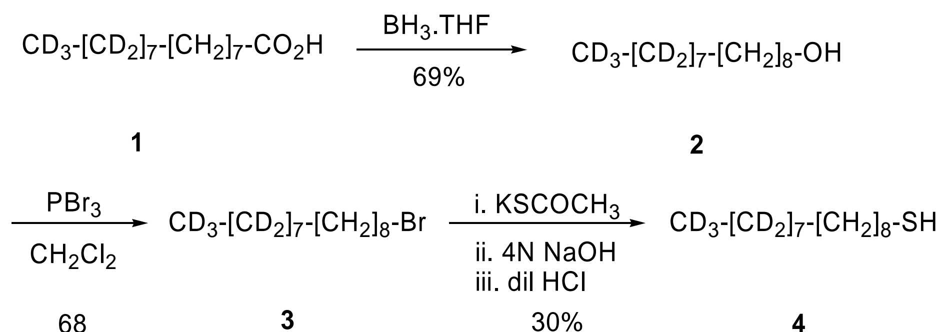

Hexadecyl-9,9,10,10,11,11,12,12,13,13,14,14,15,15,16,16 – d_{17} Alcohol (2).

To a solution of 0.5 g (1.832mmol) of partially deuterated acid **1** in 25 ml of dry THF, 4.0 ml of 1 M Borane-THF complex (4 mmol) in drops at 0°C. The resulting solution was warmed to room temperature over half an hour and then refluxed for 12 h under positive nitrogen atmosphere. The reaction was quenched with 10 ml of 50-50 water-THF mixture

followed by the addition of 10 ml of saturated potassium carbonate solution. The reaction mixture was extracted with ether (3 x 100 ml). The combined extracts were washed with brine and dried over $MgSO_4$. Evaporation of the solvent yielded 0.330g (69%) of alcohol **2**. ^{1}H NMR ($CDCl_3$) δ 3.62 (t, 2H), 1.27 (m, 14); ^{13}C NMR ($CDCl_3$) δ 14.2, 26.1, 26.8, 29.8, 30, 33.2, 63.5; GCMS – [m/e, intensity : M+ - 259, (1%) , 241 (7%), 213 (8%), 198(1%), 182 (3%), 169 (3%), 154 (4%), 139 (8%), 123 (12%), 107 (25%), 97 (36%), 83 (100), 68 (82%), 59 (36%), 50 (94%), 41(62%)].

Hexadecyl-9,9,10,10,11,11,12,12,13,13,14,14,15,15,16,16 – d_{17} Bromide (3).

0.7 ml of phosphorus tribromide (2g, 7.39 mmol) was dissolved in 10 ml of dichloromethane in an Erlenmeyer flask. 0.330 g of the alcohol **2** was dissolved in 35 ml of dichloromethane and cooled in an ice bath. The phosphorus tribromide solution was added to the alcohol-dichloromethane solution in drops over 5 mins. The solution was warmed to room temperature and stirred overnight. The reaction was quenched with 5 ml of ethanol and 15 ml of saturated $NaHCO_3$ solution. The reaction mixture was extracted with 3 x 100 ml of ether. The combined ether extracts were washed with brine and dried over $MgSO_4$. The solvent was removed *in vaccuo*. The product was purified by column chromatography using hexane as the eluent yielding 0.279g (68%) of hexadecyl – d_{17} bromide **3**. ^{1}H NMR ($CDCl_3$) δ 3.42 (t, 2H), 1.27 (m, 14);

Hexadecyl-9,9,10,10,11,11,12,12,13,13,14,14,15,15,16,16 – d_{17} thiol (4).

Hexadecyl – d_{17} bromide **3** (0.279g, 0.866 mmol) obtained from previous step was dissolved in 80 ml of degassed ethanol. 0.100 g of potassium thioacetate (1.842 mmol)

was added to the above solution and refluxed for 24 h under positive nitrogen atmosphere. The solvent was removed *in vaccuo* and added 15ml of brine to the residue. The resulting suspension was extracted with 3 x 75 ml of ether. The combined ether extracts were washed with brine and dried over Na_2SO_4. GCMS analysis of this extract showed that the reaction mixture contained a mixture of hexadecyl – d_{17} thioacetate and corresponding thiol. The solvent was removed *in vaccuo*. The crude reaction mixture was dissolved in 10 ml of degassed ethanol and added 2 ml of 4N NaOH solution and refluxed under nitrogen for 2 m. After removing the solvent under vacuum the residue was dissolved in a mixture 50 ml of degassed ether and 15 ml of degassed 18% HCl. This solution mixture was extracted with 3 x 75 ml of ether. The combined ether extracts were washed with brine and dried over Na_2SO_4. The product was purified by column chromatography using hexane as the eluent yielding 0.72g (30%) of hexadecyl – d_{17} thiol **4**. ^{1}H NMR ($CDCl_3$) δ 2.52 (q, 2H), 1.27 (m, 14); ^{13}C NMR ($CDCl_3$) δ 14, 23.2, 26.2, 29.0, 30, 32.5, GCMS – [m/e, intensity : M+ - 275, (38%) , 240 (26%), 211 (10%), 196(1%), 181 (3%), 166 (3%), 151 (4%), 134 (8%), 117 (22%), 101 (40%), 89 (72%), 69 (81%), 50 (100%), 41(82%)].

Appendix B

Supplemental Materials for Chapter 5

Preparation and Characterization of 4, 4'- Di(ethynylphenyl)-1-(isocyano) benzene

The OPE-isonitrile **3** was prepared by following Castro-Stephens/Sonogashiro's palladium-copper cross-coupling protocol[1] as described in Scheme 1.

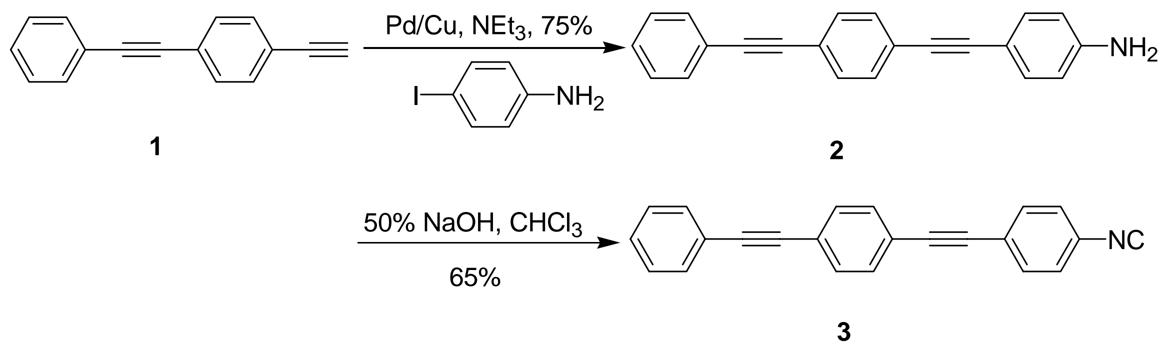

Scheme 1: Synthesis of 4, 4'- Di(ethynylphenyl)-1-(isocyano) benzene **3**

4, 4'- Di(ethynylphenyl)-1-(amino) benzene (2)

In a dry 100ml flask, 1.0 g of 1-Ethynyl-4-(ethynylphenyl)benzene **1**[2] (4.95 mmol), 1.084 g of 4-iodoaniline (4.95 mmol), 0.237g of bis(triphenylphosphine)palladium (II) dichloride (0.237 mmol), 0.160 g of copper(I) iodide and 9.1 mL of triethylamine (65.15 mmol) were dissolved in 15mL of benzene and heated at 70°C under nitrogen for 2 days. The reaction mixture was quenched with 25 mL of saturated ammonium chloride and extracted with 3 x 100 mL of ether. The combined organic layers were dried with anhyd. $MgSO_4$ and the solvent was removed *in vaccuo*. The product was purified by column chromatography using 1:5 ethylacetate-

hexanes as the eluent yielding 1.087 g (75%) of 4, 4'- Di(ethynylphenyl)-1-(amino) benzene **2**. ^{1}H NMR ($CDCl_3$) 7.54-7.45 (m, 6H), 77.34 – 7.42 (m, 5H), 6.65 (d, 8.5 Hz, 2H), 3.86 (s, br, 2H).

Di(ethynylphenyl)-1-(isocyano) benzene (3)

The isonitrile **3** was prepared using a modified literature procedure.[3] In a 50 mL flask was added 0.500 g of **2** (1.7 mmol) was dissolved in 20 mL of dichloromethane. To this solution, 0.2 g of benzyltriethylammonium chloride (0.09 mmol), 50 mL of 50:50 w/w NaOH and 1mL of chloroform (8.37 mmol) were added. The reaction mixture was gently refluxed overnight followed by the addition of 100 mL of water. The organic layer was diluted with 50 mL of dichloromethane and was washed with 3 x 100 mL of water and 100 mL brine. The organic layer was dried over $MgSO_4$ and the solvent was removed *in vaccuo* yielding 0.330g of **3** (65% crude yield). The product was purified by column chromatography using 1:10 ether-hexanes as the eluent. MS: m/z 303 (M^+); 304 (M + H). ^{1}H NMR ($CDCl_3$) . 7.3-7.45 (m, 8H), 7.15-7.3 (m, 5H). ^{13}C NMR ($CDCl_3$) 166.1, 133.0, 132.0, 129.0, 128.8, 126.9, 124.9, 124.2, 123.3, 122.6, 92.3, 92.1, 89.9, 89.3. IR spectrum (KBr): (C≡C) 2198cm^{-1}, (N≡C) 2122cm^{-1}

References

1. (a) Takahashi, S.; Kuroyama, Y.; Sonogashira, K.; Hagihara, N. *Synthesis*, **1980**, 627. (b) Stephens, R.D.; Castro, C.E.; *J.Org. Chem*. **1963**, *28*, 3313.

2. Tour, J.M.; Rawlett, A.M.; Kozaki, M.; Yao, Y.; Jagessar, R.C.; Dirk, S.M.; Price, D.W.; Reed, M.A.; Zhou, C.; Chen, J.; Wang, W.; Campbell, I. *Chem. Eur. J*. **2001**, *7*, No. 23, 5118.

3. Henderson, J.I.; Feng, S.; Ferrence, G.M.; Bein, T.; Kubiak, C.P. Inorg.Chim.Acta. **1996**, *242*, 115.

Vita

Thomas A. Daniel

Born

September 13, 1977 in Miami, Florida

Education

The Pennsylvania State University
Ph.D., Chemistry, August 2005
Thesis advisor: Dr. David L. Allara

Mercer University
B.S.E., Biomedical Engineering, May 1999

Relevant Employment

Graduate Research Assistant 1999-present

Graduate Teaching Assistant 1999-2000

Summer Research Assistant 1999 summer

Undergraduate Research Assistant 1998-1999
Mercer University Chemistry Department

Undergraduate Research Assistant 1998 summer
Oklahoma University Chemistry Department